

Measurement of the spin structure function g_1^d of the deuteron and its moments at low Q^2

Krishna P. Adhikari, Sebastian E. Kuhn,
Alexander Deur, Lamiaa El Fassi, Hyekoo Kang, Sarah K. Phillips,
Marco Ripani, Karl Slifer, Raffaella De Vita, Gail E. Dodge,
Xiaochao Zheng

March 18, 2017

Contents

1	Introduction	4
1.1	Inclusive Electron Scattering	6
1.1.1	Kinematic Variables	7
1.1.2	Differential Cross Section and Structure Functions . . .	9
1.2	Moments of g_1 and Sum Rules	10
1.2.1	First moment Γ_1 of g_1	10
1.2.2	Generalized GDH Integral	12
1.2.3	Generalized Forward Spin Polarizability γ_0	14
2	EG4 run	16
2.1	New CC in the 6 th Sector	18
3	Data Analysis Procedure	22
3.1	Raw Data Processing - Calibration and Reconstruction	23
3.2	Helicity States	25
3.3	Electron Identification	25
3.3.1	Electromagnetic Calorimeter Cuts	27
3.3.2	Cerenkov Counter Cuts	36
3.3.3	Minimum/Maximum Momentum cuts	42
3.3.4	Vertex-Z cuts	43
3.3.5	Fiducial Cuts	46
3.4	Data Quality and Stability Checks	53
3.5	Kinematic Corrections	56
3.5.1	Incoming Energy Loss Correction	56
3.5.2	Tracking Corrections	57
3.5.3	Momentum Correction	64
3.5.4	Outgoing Ionization Loss Correction	68
3.6	Cerenkov Counter (CC) Efficiency	69

3.6.1	Procedure	71
3.7	Pion Contamination Corrections	76
3.7.1	Method	76
3.8	e^+e^- -Pair Symmetric Contamination Corrections	78
3.9	Study of NH_3 Contamination of EG4 ND_3 Target	80
3.9.1	Procedure	80
3.9.2	Event Selection	81
3.9.3	Extracting the Contamination	83
3.9.4	Results and Conclusion	84
4	Monte Carlo Simulations and Extraction of g_1 and $A_1 F_1$	86
4.1	Simulation and Approach to Analysis	86
4.1.1	Outline of the method	89
4.2	Radiative Corrections	91
4.3	“Standard” simulation	91
4.3.1	RCSLACPOL	92
4.3.2	Event Generator	92
4.3.3	GSIM - CLAS Detector Simulation	94
4.3.4	GSIM POST PROCESSOR (GPP)	95
4.4	Comparison of Data and Simulation	98
4.5	Method to Extract g_1 and $A_1 F_1$	107
4.5.1	‘Variation’ of the standard simulation	107
5	Systematic Uncertainties	112
5.1	Evaluation of Experimental Systematics	113
5.2	Model uncertainties	115
5.3	Combining uncertainties	117
5.3.1	Combining data from the two beam energies	118
6	Results	129
6.1	Extracted g_1 and $A_1 F_1$	129
6.2	Moments of Deuteron Spin Structure functions	138
6.2.1	First moment of g_1 (Γ_1)	140
6.2.2	The extended GDH integral \bar{I}_{TT}	142
6.2.3	The Generalized Forward Spin Polarizability γ_0	144
7	Conclusions	147

¹ Chapter 1

² Introduction

³
⁴ A large amount of data on the spin dependent structure of the nucleon has
⁵ been accumulated since the late 1970s from both fixed target and colliding
⁶ beam experiments with polarized photons, (anti)electrons, and muons as well
⁷ as protons on a variety of polarized targets from hydrogen through 3He .

⁸ In a simple non-relativistic model one would expect the quarks to carry
⁹ the entire spin of the nucleon, but one of the first experiments carried out
¹⁰ at SLAC, in a limited kinematic region, seemed to confirm the predictions
¹¹ of the Naive Parton Model (NPM) - one of the early more realistic theo-
¹² ries - which predicted that 60% of the nucleon spin is carried by the quarks
¹³ [1]. However, a subsequent, more precise measurement over a larger kinematic
¹⁴ region performed by the EMC experiment at CERN reported, contrary to
¹⁵ the NPM predictions, that only $12 \pm 17\%$ of the spin is carried by the quarks
¹⁶ [2]. This discovery of the so-called “spin crisis” sparked a large interest in
¹⁷ measuring the spin content of the nucleon, giving birth to several experiments
¹⁸ (completed, underway and proposed) around the globe. The theoretical de-
¹⁹ velopments of Quantum Chromodynamics (QCD) - the quantum field theory
²⁰ that describes the nuclear interaction between the quarks and gluons - have
²¹ clarified our picture of the nucleon spin structure in great details. With the
²² discovery of a unique QCD property known as “asymptotic freedom”, quarks
²³ are known to be essentially free at high energies (typically several GeV) al-
²⁴ lowing perturbative QCD (PQCD) calculations of testable predictions for
²⁵ processes involving high energy or high momentum transfers [3]. Verifying
²⁶ Bjorken sum rule [4], which relates results from inclusive, polarized deep in-
²⁷ elastic scattering (DIS) to the axial coupling constant g_A of neutron beta

28 decay, is a precise test of QCD in its spin sector. The DIS results have ver-
29 ified the Bjorken sum rule at the level of 10% accuracy and has shown that
30 only about $30 \pm 10\%$ of the nucleon spin is carried by the quarks; the rest
31 of the spin must reside either in gluons or orbital angular momentum of its
32 constituents. Experiments to measure the gluon contribution are underway
33 at Brookhaven National Laboratory (BNL) and CERN.

34 Probing nucleon structure on the other end of the energy scale (i.e. prob-
35 ing with low momentum transfers) provides information about long distance
36 structure, which is also associated with static properties of the nucleon. In
37 this low energy regime, however, QCD calculations with the established per-
38 turbative methods become difficult or even impossible because the strong
39 coupling (α_s) becomes large. Thus perturbative expansions do not converge.
40 In this energy regime, the partons become very strongly coupled to the point
41 of being confined into hadrons which now emerge as the effective degrees of
42 freedom for the interaction. Therefore, other methods must be relied on to
43 make predictions in these non-perturbative energy scales. For example, effec-
44 tive theories such as chiral perturbation theory (χ PT) are used. There is also
45 an intermediate region where neither of these approaches (PQCD or χ PT)
46 is expected to work. In this region, it is expected that lattice QCD methods
47 will provide testable predictions in the near future. There are also some phe-
48 nomenological models aimed at describing the entire kinematic range. The
49 description of the low energy regime in terms of these theories and models
50 is challenging and theories used here still face difficulties (see below). There
51 are several predictions (for both nucleons as well as some light nuclei such as
52 the deuteron and Helium-3) from these low energy theories and models on
53 various observables which can be tested experimentally. Therefore, having
54 high precision data at the lowest possible momentum transfer is necessary to
55 test these predictions. In addition, new results will also help constrain future
56 calculations and provide input for detailed corrections to higher energy data.

57 With that perspective and motivation, the “EG4” experiment (E06-017)
58 for a precision double polarization measurement at low momentum transfer
59 using both proton and deuteron targets and the Hall B CLAS detector was
60 performed at Jefferson Lab. In addition to the usefulness of the measured
61 deuteron data for testing theoretical predictions calculated for the deuteron
62 itself, the data are also necessary for extracting neutron data in combination
63 with similar data from the proton target. An experiment with the similar
64 goal of probing the neutron at low momentum transfers but using ^3He was
65 performed in Hall A [5]. However, to be able to control nuclear medium

66 effects, neutron information must be extracted from both 3He and 2D . The
67 data on the deuteron (and eventually on the neutron) will not only be useful
68 to test the theoretical predictions at low but non-zero momentum transfers
69 but they can also be extrapolated to the real photon limit, thus testing some
70 long standing predictions such as the Gerasimov-Drell-Hearn (GDH) sum
71 rule [6, 7] derived from general principles. The analysis of the deuteron data
72 is the subject of this note.

73 In the future, we will extract information from the deuteron and proton
74 data from the EG4 experiment to provide a self-consistent determination of
75 the Bjorken sum, helping us to understand the transition from the partonic to
76 hadronic descriptions of the strong interaction. The data will also be useful in
77 studying the validity of quark-hadron duality in the spin sector, thus helping
78 further to understand the transition from the partonic to hadronic pictures.

79 **1.1 Inclusive Electron Scattering**

80 High energy particle scattering processes provide very powerful microscopes
81 to examine objects such as nuclei and nucleons. Scattering of leptons (most
82 commonly electrons) is one of the most extensively used processes. For ex-
83 ample, the scattering of high energy leptons off nucleons has played a key role
84 in determining the partonic structure of the nucleons. Following are some of
85 the advantages of lepton (and in particular electron) scattering:

- 86 • Leptons interact through the electroweak interaction which is very well
87 understood.
- 88 • The interaction is relatively weak, thus allowing the use of perturbative
89 QED.
- 90 • In electron scattering, one can, moreover, control and vary the po-
91 larization of the virtual photon (exchanged during the interaction) by
92 changing the electron kinematics. This allows the separation of the
93 charge and current interaction. Data from the scattering of polarized
94 electrons by polarized targets allows one to examine the target's strong-
95 interaction spin structure.
- 96 • A great advantage of electrons is that they can be copiously produced
97 in the laboratory relatively easily and at low costs, and since they are

98 charged, they can readily be accelerated and detected. (It is not as
99 easy and cheap to produce and handle the other lepton types.

100 In this section, we discuss the process of inclusive electron scattering (in
101 which only the scattered electron is detected ignoring the rest of the com-
102 ponents of the final state after the interaction). In doing so, the relevant
103 kinematic variables and related physical quantities to be measured or calcu-
104 lated from the process will be introduced and some of their relations with
105 one another will be deduced and discussed.

106 1.1.1 Kinematic Variables

107 A lepton scattering process, in which an incoming lepton represented by $l(p)$
108 of four momentum $p = p^\mu = (E, \vec{k})$ scatters off a target $N(P)$ which is usually
109 a nucleon or a nucleus at rest and with four momentum $P = P^\mu = (M, \vec{0})$,
110 can simply be represented by

$$l(p) + N(P) \rightarrow l(p') + X(P') \quad (1.1)$$

111 where $l(p')$ and $X(P')$ represent the scattered lepton and the rest of the
112 final state (which can have any number of particles) with four momenta
113 $p'^\mu = (E', \vec{k}')$ and $P'^\mu = (E_X, \vec{k}_X)$ respectively. The scattering angle which is
114 the angle between the incident and outgoing path/direction of the electron
115 is denoted by θ . The final (hadronic) state denoted by x is not measured,
116 with only the scattered electron detected and measured by the detector(s).
117 In the first order (Born) approximation of the process, a virtual photon is
118 exchanged (as depicted in Fig (1.1)) whose four momentum is equal to the
119 difference between that of the incident and the scattered electron and is given
120 by $(p - p')^\mu = (\nu, \vec{q})$, where $\nu = (P \cdot q)/M$ and \vec{q} represent the energy and
121 3-momentum transferred by the incident electron to the target $N(P)$.

122 The kinematics of the scattering process, for a given beam energy E , can
123 be completely described in terms of two of the following Lorentz invariant

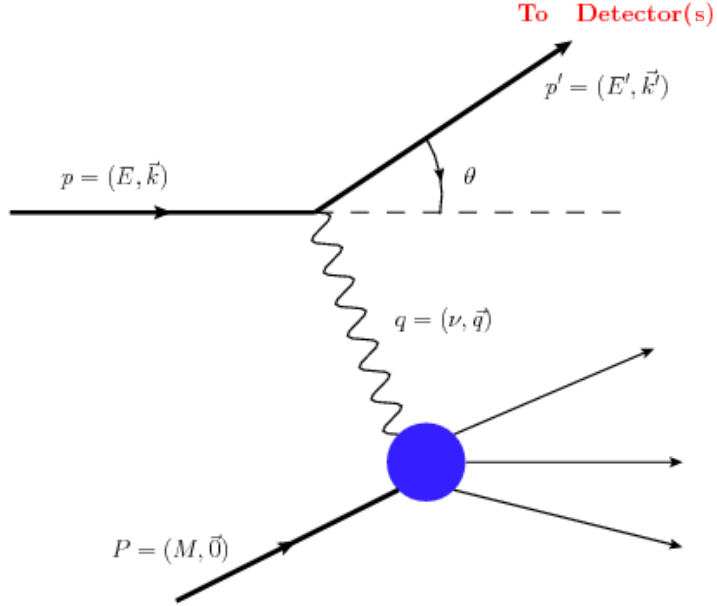


Figure 1.1: Lowest order (Born approximation) Feynmann diagram representing the process of inclusive lepton scattering

¹²⁴ variables.

$$\nu = E - E' \quad (1.2)$$

$$Q^2 = -q^2 \simeq 4EE' \sin^2 \frac{\theta}{2} \quad (1.3)$$

$$W = \sqrt{(P+q)^2} = \sqrt{M^2 + 2M\nu - Q^2} \quad (1.4)$$

$$x = \frac{Q^2}{2P \cdot q} = \frac{Q^2}{2M\nu} \quad (1.5)$$

$$y = \frac{q \cdot P}{p \cdot P} = \frac{\nu}{E} \quad (1.6)$$

¹²⁵ where $Q^2 = -q^2$ is the negative of the squared four-momentum transferred
¹²⁶ (with electron mass neglected in the expression for Q^2), which defines the
¹²⁷ resolution of the electron probe; W is the invariant mass of the unmeasured
¹²⁸ final state (x); x is known as the Bjorken scaling variable, which is also
¹²⁹ interpreted as the momentum fraction carried by the struck quark (parton)
¹³⁰ in the infinite momentum frame; M is the nucleon mass ≈ 0.939 GeV, and
¹³¹ lastly, y is the fraction of the energy that is lost by the lepton during the

¹³² process.

¹³³ ¹³⁴ 1.1.2 Differential Cross Section and Structure Functions

¹³⁵ The differential cross section for the process of inclusive (polarized) elec-
¹³⁶ tron scattering on (polarized) targets can be expressed, in the Born ap-
¹³⁷ proximation, in terms of four dimensionless structure functions $F_1(x, Q^2)$,
¹³⁸ $F_2(x, Q^2)$, $g_1(x, Q^2)$, and $g_2(x, Q^2)$, effectively parameterizing the internal
¹³⁹ hadronic structure information into four response functions. For example,
¹⁴⁰ in the case of the anti-parallel or parallel beam and target polarizations,
¹⁴¹ the spin-dependent (polarized) inclusive cross sections can be expressed as
¹⁴² follows:

$$\frac{d^2\sigma}{d\Omega dE'} = \left(\frac{d\sigma}{d\Omega} \right)_{Point} \left[\frac{2}{M} F_1(x, Q^2) \tan^2 \frac{\theta}{2} + \frac{1}{\nu} F_2(x, Q^2) \right. \\ \left. \pm 2 \tan^2 \frac{\theta}{2} \left[(E + E' \cos \theta) \frac{M^2}{\nu} g_1(Q^2, \nu) - \gamma^2 M^2 g_2(Q^2, \nu) \right] \right]^{(1.7)}$$

¹⁴³ where “+” refers to anti-parallel beam helicity and target polarization,
¹⁴⁴ while “-” refers to the parallel case. And the Point cross section (for the
¹⁴⁵ lepton scattering from a Dirac particle - a spin-1/2 point particle of charge
¹⁴⁶ $+e$) given by

$$\left(\frac{d\sigma}{d\Omega} \right)_{Point} = \frac{\alpha^2 \cos^2 \frac{\theta}{2}}{4E^2 \sin^4 \frac{\theta}{2}} \frac{E'}{E} \quad (1.8)$$

¹⁴⁷ with $\frac{E'}{E}$ being the recoil factor.

¹⁴⁸ These kind of relationships allow the measurement of structure functions
¹⁴⁹ by measuring cross-sections corresponding to different combinations of beam
¹⁵⁰ and target polarizations. For example, one can extract the first two structure
¹⁵¹ functions F_1 and F_2 from the unpolarized scattering experiments, whereas,
¹⁵² the spin structure functions g_1 and g_2 can be measured in experiments with
¹⁵³ polarized electron beam and polarized targets and by measuring the cross
¹⁵⁴ section difference between the anti-parallel and parallel beam-target polar-
¹⁵⁵ izations.

¹⁵⁶ **1.2 Moments of g_1 and Sum Rules**

¹⁵⁷ Moments of structure functions are their integrals (over the complete x range)
¹⁵⁸ weighted by various powers of the variable x. The n^{th} moment of g_1 , for
¹⁵⁹ example, is given by

$$\Gamma_n(Q^2) = \int_0^1 g_1(x, Q^2) x^{(n-1)} dx \quad (1.9)$$

¹⁶⁰ The moments allow the studies of the (Q^2 dependence of) fundamental
¹⁶¹ properties of nucleon structure. For example, the first moment of xF_1 of a
¹⁶² nucleon gives the total momentum or mass fraction carried by quarks and the
¹⁶³ first moment of g_1 gives the fraction of the nucleon spin contributed by the
¹⁶⁴ quark helicities. These integrals get their particular significance from the fact
¹⁶⁵ that they can be predicted from rigorous theoretical methods, such as in the
¹⁶⁶ sum rules derived from general assumptions or from the method of Operator
¹⁶⁷ Product Expansion, lattice QCD calculations and χ PT calculations¹. Their
¹⁶⁸ importance can be highlighted from the fact that it was the experimental
¹⁶⁹ tests of the sum rules involving the first moments of nucleon that led to the
¹⁷⁰ discovery of the original “spin crisis” and provided a significant test of QCD
¹⁷¹ in the spin sector [8].

¹⁷² In this section, three integrals are considered which have been calculated
¹⁷³ from the EG4 data on the deuteron - the first moment of g_1 (Γ_1), the gen-
¹⁷⁴ eralized GDH integral (\bar{I}_{TT}), and the generalized forward spin polarizability
¹⁷⁵ (γ_0).

¹⁷⁶ **1.2.1 First moment Γ_1 of g_1**

¹⁷⁷ The first moment of g_1 is the integral of g_1 over the complete range of the
¹⁷⁸ Bjorken scaling variable x.

$$\Gamma_1(Q^2) = \int_0^1 g_1(x, Q^2) dx \quad (1.10)$$

¹In contrast, the same is not true about the structure functions because presently their complete description based on QCD first principles has not been possible yet (especially in the low to intermediate momentum transfer regions due to the strong coupling property of QCD).

179 This moment gives, in the quark-parton model, the fraction of the nu-
180 cleon spin contributed by the quark helicities and enters directly into two
181 historically important sum rules - Ellis-Jaffe sum rule and Bjorken sum rule.
182 Measurements of the moment on the proton by the European Muon Collabo-
183 ration (EMC) in 1988 showed that the Ellis-Jaffe sum rule is violated, which
184 meant that the long held belief that all the proton spin is carried by quarks
185 is not true, thus, sparking the well known “spin crisis”. On the other hand,
186 measurements from SLAC, CERN, Fermilab, DESY, and more recently, from
187 JLab, have confirmed the Bjorken sum rule (which relates the difference of
188 the first moments of the proton and the neutron to the fundamental axial
189 coupling constant (g_A) of neutron beta decay) at the level of 10% accuracy,
190 thus helping establish the QCD as the correct theory of the strong interac-
191 tions. The moment also enters into the virtual photon extension of another
192 famous sum rule - the GDH sum rule (see below).

193 In addition, the moment is studied on its own right because it provides
194 a powerful tool to test the validity of various theories and models in which
195 it is calculable. In the past, it has been measured on proton, deuteron and
196 neutron (${}^3\text{He}$) at SLAC, CERN and DESY in the DIS region in order to
197 understand the quark spin contribution as well as to test the validity of
198 the Bjorken sum rule and hence QCD as a result [8]. Recently, it has also
199 been measured at JLab from DIS down to a fairly low Q^2 region. In the
200 intermediate and low momentum transfers, some phenomenological model
201 predictions are available, whereas in the very low Q^2 region, several chiral
202 perturbation theory (χPT) calculations are available.

203 **1.2.2 Generalized GDH Integral**

204 **GDH Sum Rule**

205 The Gerasimov-Drell-Hearn (GDH) sum rule [6, 7] relates the energy weighted
206 sum of a particle's photo-absorption cross sections to its anomalous magnetic
207 moment κ . For a target of arbitrary spin S , the sum rule is:

$$\int_{\nu_{th}}^{\infty} \frac{\sigma_P(\nu) - \sigma_A(\nu)}{\nu} = -4\pi^2 \alpha S \left(\frac{\kappa}{M}\right)^2 \quad (1.11)$$

208 where σ_P and σ_A are the photoabsorption cross sections with photon helicity
209 parallel and anti-parallel to the target spin respectively. M and κ represent
210 the target mass and anomalous magnetic moment respectively and S rep-
211 resents the target spin. The integration extends from the onset ν_{th} of the
212 inelastic region ² through the entire kinematic range and is weighted by the
213 inverse of the photon energy ν .

214 The sum rule for the proton has been measured (at various places such as
215 Mainz, Bonn, BNL and others) and verified to within 10% [9–12] and some
216 deuteron results exist from Mainz and Bonn, but there is very little or no
217 data available on neutron and other targets;

218 **Implications of the sum rule** The sum rule relates the static property
219 κ of a particle's ground state with the sum of the dynamic properties of
220 all the excited states. One deeper significance of this sum rule is that if a
221 particle has a non-zero anomalous magnetic moment, then it must have some
222 internal structure, and, therefore, a finite size and the excited states (a point-
223 like particle cannot have excited states). Because of the same reason, the
224 discovery of nucleon anomalous magnetic moments provided one of the first
225 strong indications that the nucleons had some intrinsic internal structure.

226 In addition to the benefit of that implication, the sum rule and its exten-
227 sion to $Q^2 > 0$ provides an important testing ground for various theoretical
228 predictions based on QCD and its effective theories/models.

²The pion photo-production threshold given by $\nu_{th} = m_\pi(1 + m_\pi/2M) \approx 150\text{MeV}$ marks the onset of the inelastic region for the nucleons, but for nuclei, the summation starts from the first nuclear excitation level

229 **Generalization of the GDH Sum (Rule)**

230 In order to investigate the “spin crisis” of the 1980’s, Anselmino *et al.* [13]
 231 proposed that the real photon ($Q^2=0$) GDH integral could be extended to
 232 electroproduction cross sections (finite Q^2) and that the experimental deter-
 233 mination of the extended integral would shed light on the transition from
 234 the perturbative to non-perturbative QCD. The idea was to use the virtual
 235 photoabsorption cross sections in place of the real photoabsorption cross sec-
 236 tions and proceed in exactly the same way as when deriving the real photon
 237 GDH sum rule. This extension depends somewhat on the choice of the vir-
 238 tual photon flux and on how the spin structure function g_2 is considered [14].
 239 In one extension the virtual photon flux given by $K = \nu$ is chosen and the
 240 real photoabsorption cross section difference in Eq. 1.11 are replaced by
 241 the corresponding virtual photoabsorption cross section difference $2\sigma_{TT}$. As
 242 a result, we get the following extended GDH integral (considering only the
 243 inelastic contribution starting from the pion production threshold) [8]

$$\bar{I}_{TT} = \frac{2M^2}{Q^2} \int_0^{x_0(Q^2)} dx [g_1(x, Q^2) - \frac{4M^2 x^2}{Q^2} g_2(x, Q^2)] \quad (1.12)$$

244 where $x_0(Q^2) = Q^2/(Q^2 + m_\pi(2M + m_\pi))$ is the pion production threshold
 245 that defines the onset of the inelastic region.

246 The integral can also be expressed in terms of the first moment of the
 247 product $A_1 F_1$ as follows:

$$\bar{I}_{TT} = \frac{2M^2}{Q^2} \int_0^{x_0(Q^2)} dx A_1(x, Q^2) F_1(x, Q^2) \quad (1.13)$$

248 where A_1 is the virtual photon asymmetry as given by:

$$A_1(x, Q^2) = \frac{\sigma_{\frac{1}{2}}^T - \sigma_{\frac{3}{2}}^T}{\sigma_{\frac{1}{2}}^T + \sigma_{\frac{3}{2}}^T} = \frac{g_1(x, Q^2) - \gamma^2 g_2(x, Q^2)}{F_1(x, Q^2)} \quad (1.14)$$

$$(1.15)$$

249 **1.2.3 Generalized Forward Spin Polarizability γ_0**

250 Polarizabilities are fundamental observables (quantities) that characterize the
251 structure of composite objects such as nucleons or deuteron. They reflect the
252 response to external perturbations such as external electromagnetic fields.
253 Like the GDH sum, they are also integrals over the excitation spectrum of
254 the target and their derivations rely on the same basic assumptions. At
255 the real photon point, for example, the electric and magnetic polarizabilities
256 α and β represent the target's response to external electric and magnetic
257 fields respectively. The generalized polarizabilities represent the extensions
258 of these quantities to the case of virtual photon Compton scattering. Because
259 the integrals defining the polarizabilities involve weighting by some powers
260 of $1/\nu$ or x , they converge faster than the first moments and thus are more
261 easily determined from low energy measurements. In other words, they have
262 reduced dependence on the extrapolations to the unmeasured regions at large
263 ν , and higher sensitivity to the low energy behavior of the cross sections
264 (particularly the threshold behavior), thus providing better testing grounds
265 for theoretical predictions such as from χ PT and phenomenological models
266 [14].

267 The GDH sum rule comes from the first term of the low energy expansion
268 of the forward Compton amplitude [15]. Likewise, we get another sum rule
269 from the second, i.e., the next-to-leading term (which is in the third power
270 of ν). The second coefficient of the expansion is known as the forward spin
271 polarizability γ_0 and by comparing the coefficients of the ν^2 terms on both
272 sides (coming from the dispersion relations on the left side and from the low
273 energy expansion on the right side) gives us the following expression for the
274 polarizability [16]:

$$\gamma_0 = -\frac{1}{4\pi^2} \int_{thr}^{\infty} \frac{\sigma_{\frac{1}{2}} - \sigma_{\frac{3}{2}}}{\nu^3} d\nu \quad (1.16)$$

275 Now, by considering the case of forward scattering of a virtual photon and
276 using the same general approach as for getting the generalized GDH sum rule,
277 the $\mathcal{O}(\nu^3)$ (NLO) term in the low energy expansion of VVCS (doubly virtual
278 Compton scattering) amplitude $g_{TT}(x, Q^2)$ gives the following generalization
279 of the forward spin polarizability [17] [8]:

$$\begin{aligned}\gamma_0(Q^2) \equiv \gamma_{TT}(Q^2) &= \frac{16\alpha M^2}{Q^6} \int_0^{x_0} \left[g_1(x, Q^2) - \frac{4M^2 x^2}{Q^2} g_2(x, Q^2) \right] x^2 dx \\ &= \frac{16\alpha M^2}{Q^6} \int_0^{x_0} A_1(x, Q^2) F_1(x, Q^2) x^2 dx\end{aligned}\quad (1.18)$$

280 where $\alpha = \frac{e^2}{4\pi}$ is the fine structure constant. At large Q^2 , the g_2 dependent
 281 term in the integrand becomes negligible and γ_0 reduces to the third moment
 282 of g_1 [17].

283 In exactly the same manner, from the $\mathcal{O}(\nu^2)$ term of the low energy
 284 expansion of the VVCS amplitude $g_{LT}(x, Q^2)$ one gets another polarizability
 285 - the generalized longitudinal-transverse polarizability as follows:

$$\delta_0(Q^2) \equiv \delta_{LT}(Q^2) = \frac{16\alpha M^2}{Q^6} \int_0^{x_0} [g_1(x, Q^2) + g_2(x, Q^2)] x^2 dx \quad (1.19)$$

286 This latter polarizability is not considered here because we did not measure
 287 the transverse target configuration.

288 Because the generalized polarizabilities can be expressed with the mo-
 289 ments of the structure functions, it is possible to measure them using mea-
 290 surements of the structure functions. As stated earlier, because of the weight-
 291 ing by some powers of ν or x , these integrals converges more rapidly in energy
 292 than the GDH integral and therefore can more easily be determined by low
 293 beam energy measurements. These integrals are valuable because they shed
 294 light on the long distance (soft), non-perturbative aspects of the target struc-
 295 ture. The integrals are possible to be calculated using effective or approxi-
 296 mate theories such as χ PT and lattice methods. Thus the measurements of
 297 these quantities provide benchmark tests of such theories.

298 The first measurement of γ_0 for a proton target at the real photon point
 299 was done by the GDH experiment at Mainz [16]. Recently the JLab EG1b
 300 experiment has provided some finite Q^2 results for both deuteron as well as
 301 nucleon targets [18].

³⁰² **Chapter 2**

³⁰³ **EG4 run**

³⁰⁴ The deuteron target part of the EG4 experiment ran for about a month
³⁰⁵ in 2006, mostly with longitudinally polarized frozen $^{15}\text{ND}_3$ as the target. In
³⁰⁶ between these deuteron runs, some small amount of data was also collected on
³⁰⁷ carbon-12 and empty cell targets, which are important in various auxiliary
³⁰⁸ studies during the data analysis (such as their use in estimating nuclear
³⁰⁹ background while developing momentum corrections, estimating the length
³¹⁰ of the target material or estimating unpolarized background). A total of 113
³¹¹ data runs (from run ID 51896 to 52040) were collected for the lower beam
³¹² energy (1.3 GeV) and 221 runs (from 51593 to 51867) for the 2.0 GeV case
³¹³ (with each run consisting of about 3.0×10^7 event triggers) [19]. Each run
³¹⁴ took about 2 hours and collected about 2 GB of data in raw format and
³¹⁵ saved as about 20-30 BOS files (see next section). With the combination of
³¹⁶ low beam energies and low scattering angles, low momentum transfers can
³¹⁷ be measured down to about 0.02 GeV² within the kinematic coverage of the
³¹⁸ resonance region ($1.08 < W < 2.0$ GeV.)

³¹⁹ In addition to the use of low beam energies and low θ measurements, in
³²⁰ order to maximize the statistics in the low momentum transfers, following
³²¹ measures were taken that were unique to the experiment:

- ³²² • Use of the electron outbending torus field configuration to enhance the
³²³ low angle acceptance (so that more of very forward going electrons
³²⁴ would be bent towards and detected by the CLAS detector).
- ³²⁵ • Use of a a newly built Cerenkov Counter (CC) in the 6th sector¹ (see
³²⁶ Figs. 2.4 and 2.5) that was designed to optimize electron detection

¹For reasons of limited resources, only one new CC was built and the 6th sector alone

327 in the outbending torus configuration. This led to a better and more
328 uniform detection efficiency would be better and more uniform than
329 with the existing counters² which were optimized for electron inbending
330 configuration.

- 331 • To further enhance the low angle coverage, the polarized target was
332 placed in a more retracted position along the beam line i.e. at about
333 -101.0 cm upstream of the CLAS center.

334 Other than that the CLAS detector in the EG4 setup (see Fig. 2.1)
335 was used in the standard configuration like in any other polarized target
336 experiments using CLAS. The following list summarizes various specifications
337 of the experimental setup (for more details see [20]):

- 338 • **Beam energies:** 1.3 and 2.0 GeVs for ND₃ target runs and 1.0, 1.3,
339 2.0, 2.3 and 3.0 GeVs for NH₃ target runs.
340 – **Beam polarization:** Longitudinally polarized ($\approx 85\%$) electron
341 beam from CEBAF accelerator. Moeller scattering used for the
342 polarization measurement.
343 • **Polarized targets:** Solid ND₃, and NH₃ targets polarized using the
344 technique of Dynamic Nuclear Polarization (DNP).
345 – **Average polarizations:** Between (75 - 90)% and (30 - 45)%
346 respectively.
347 – **Lengths:** 1cm for ND₃ and 1 cm and 0.5 cm for NH₃.
348 – **Densities:** 1.056 and 0.917 respectively.
349 – **Packing fractions:** (0.624, 0.764) for (1.3, 2.0) GeV ND₃ runs
350 respectively and (0.625, 0.624/0.717³, 0.716, 0.682, 0782) for (1.0,
351 1.3/1.3, 2.0, 2.3, 3.0) GeV NH₃ runs.

was used to detect the scattered electrons

²The standard CLAS Cherenkov detectors were designed such that their optics, geometry, module position and mirror orientation were optimized for low rate high Q^2 experiments that mostly use(d) electron in-bending torus fields. The design was a compromise between the desired kinematic coverage and the complexities of the CLAS detector system including the effect of the torus field.

³The two numbers 0.624/0.717 for the 1.3 GeV NH₃ runs are due to the fact that two different NH₃ targets were used in case of 1.3 GeV runs. One target was in the top cell and the other was in the bottom cell of the target stick.

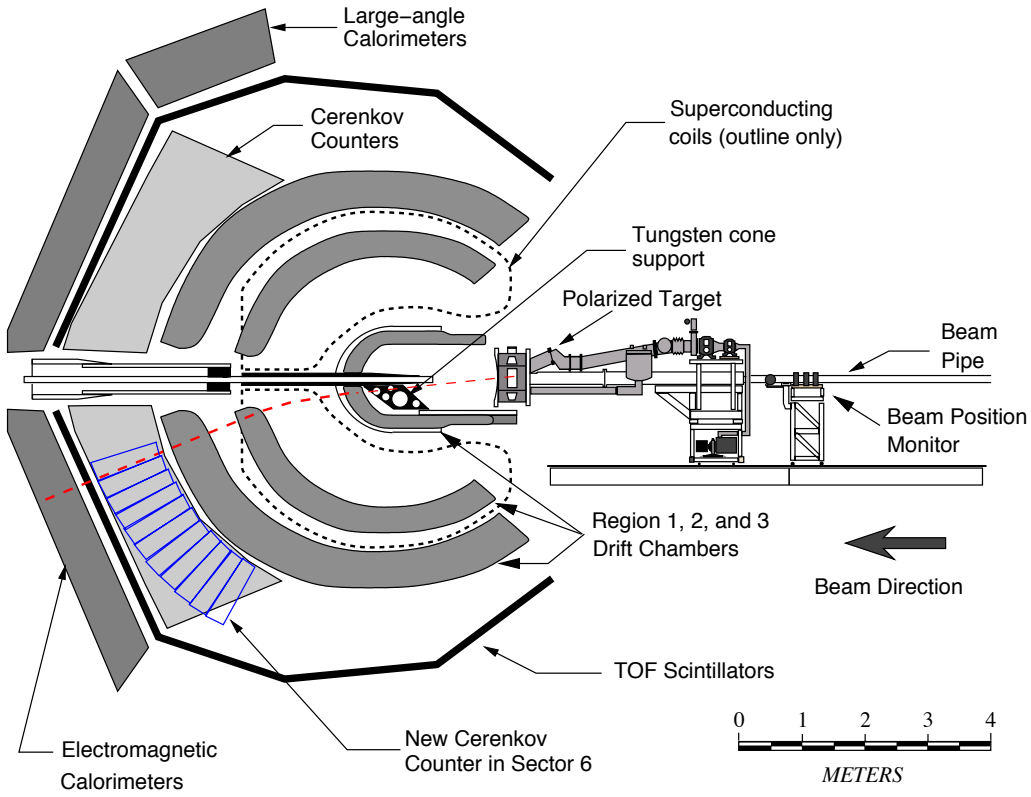


Figure 2.1: The schematic diagram of the EG4 experimental setup showing the CLAS detector, polarized target system and some beam line elements.

- 352 • **Other targets:** Carbon-12 (1 cm and 0.5 cm long), Empty target
 353 cup, Target cup filled only with liquid helium (LHe), LHe bath and
 354 various foils due to different target chamber windows.
- 355 • **Torus currents:** 1500 Amps for 1.0 and 1.3 GeV runs and 2250 A
 356 for 2.0, 2.3, and 3.0 GeV runs.

357 2.1 New CC in the 6th Sector

358 The Cherenkov Counters (CC) serve the dual function of triggering on elec-
 359 trons and separating electrons from pions (or identifying charged particles).
 360 These detectors use the light emitted by Cherenkov radiation (emission of

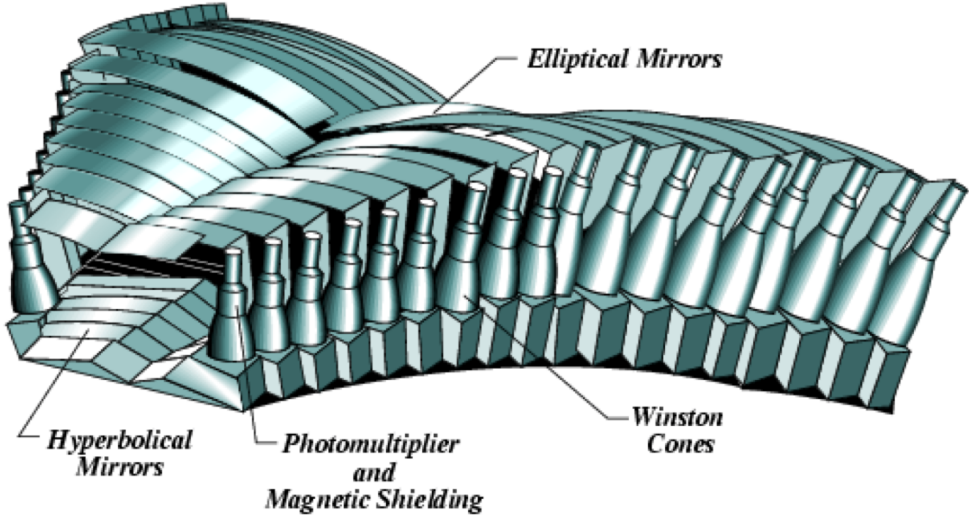


Figure 2.2: The computer rendered image of the Standard CLAS Cherenkov Counter

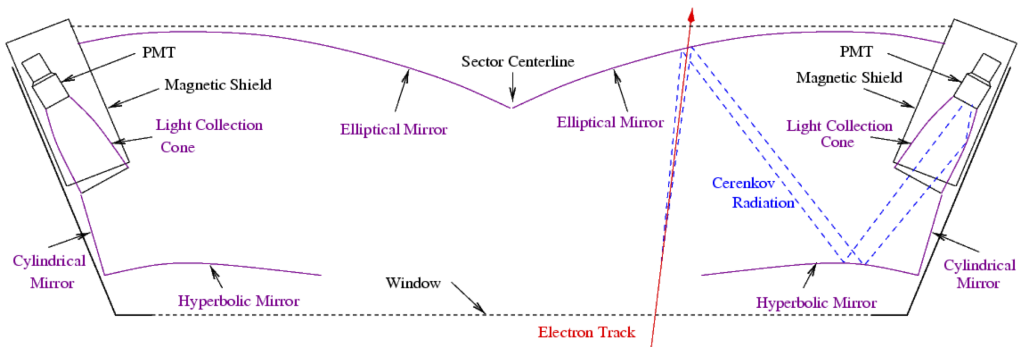


Figure 2.3: The schematic diagram of a CLAS Cherenkov Counter (CC) module showing mirrors, PMTs and the light reflections.

361 light when the charged particle travels faster than light in that medium) to
 362 measure the particle velocity (or rather $\beta = v/c$). The knowledge of β com-
 363 bined with the particle momentum (from the tracking detectors) determines
 364 the particle's mass, thus giving us information on the particle identification.
 365 The index of refraction (n) is carefully optimized for the particle masses and
 366 momentum range of the experiments in question. Threshold counters record

367 all light produced, thus providing a signal whenever β is above the threshold
368 $\beta_t = 1/n$. In the standard configuration, CLAS uses one Cherenkov threshold
369 detector in each of the six sectors in the forward region from 8° to 45° .

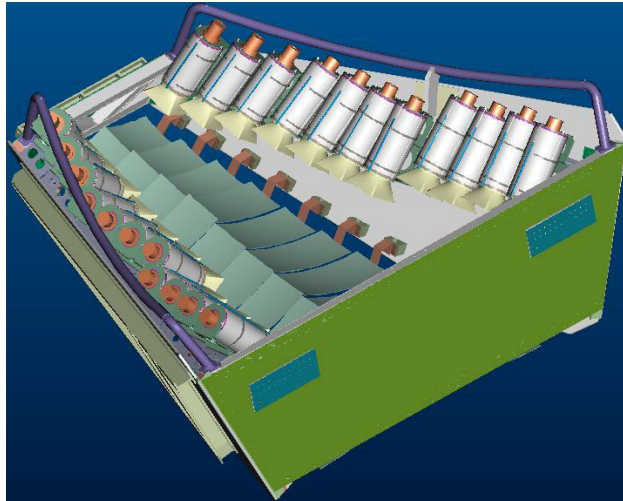
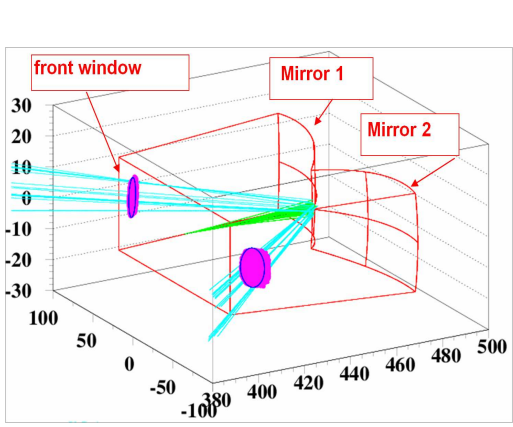
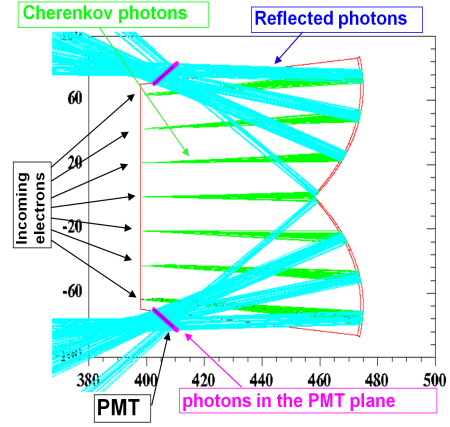


Figure 2.4: The new Cherenkov counter (courtesy of INFN, Genova)

370 A new gas threshold cherenkov counter (designed and built by INFN -
371 Genova, Italy) was installed in the sixth sector. This new CC detector (see
372 Fig. 2.4 for its CAD rendition) is specifically optimized for the out-bending
373 field configuration, which is necessary to reach the desired low momentum
374 transfer (measurements down to 6 degrees). The detector uses the same ra-
375 diator gas (C_4F_{10} - perfluorobutane) and the same gas flow control system as
376 the standard one, but it uses a different design. In the new CC, the number
377 of CC-modules is now 11 instead of the 18 in the standard ones. In order
378 to maximize the light collection, a single reflection design (see Fig. 2.5(b))
379 using spherical mirrors is used (the standard CC used double relections from
380 elliptical and hyperbolic mirrors). The geometry, the size, the mirror size,
381 position, and orientation, the dimensions as well as the assembly of the mod-
382 ules were optimized for the experiment and the performance study was done
383 using a complete GEANT simulation [16]. Additionally, for the purpose of
384 efficiency and performance studies (see Sec. 3.6), a few special trigger data
385 runs were taken during the experiment. These special runs had the trigger
386 that mainly involved EC-signals (and no CC-signal at all) to decide whether
387 the detected particle was a good scattered electron candidate.



(a) Schematic of a new CC segment.



(b) Schematic of light reflections.

Figure 2.5: Schematic of a new CC segment showing the arrangements of the mirrors, PMTs and the light reflections (courtesy of INFN, Genova).

³⁸⁸ **Chapter 3**

³⁸⁹ **Data Analysis Procedure**

³⁹⁰ The goal of this data analysis is to extract the spin structure function g_1 for
³⁹¹ the deuteron and evaluate its moments. Since the product $A_1 F_1$, which is
³⁹² proportional to σ_{TT} , directly enters sum rules for the real photon point, which
³⁹³ leads to the generalized GDH integral (\bar{I}_{TT}) and the generalized forward spin
³⁹⁴ polarizability (γ_0) being expressed in terms of the first and third moments of
³⁹⁵ the product $A_1 F_1$, we decided also to extract the product $A_1 F_1$ using exactly
³⁹⁶ the same procedure as for g_1 .

³⁹⁷ The extraction of both g_1 and $A_1 F_1$ depend directly on the measurement
³⁹⁸ of the following polarized cross-section difference:

$$\Delta\sigma_{\parallel} = \frac{d^2\sigma^{\downarrow\uparrow}}{d\Omega dE'} - \frac{d^2\sigma^{\uparrow\uparrow}}{d\Omega dE'} = \frac{1}{N_t} \cdot \left[\frac{N^+}{N_{e^-}^+} - \frac{N^-}{N_{e^-}^-} \right] \cdot \frac{1}{P_b P_t} \cdot \frac{1}{\Delta\Omega} \cdot \frac{1}{\eta_{detector}} \quad (3.1)$$

³⁹⁹ where,

- ⁴⁰⁰ • N_t = Number density of deuteron nuclei in the target
- ⁴⁰¹ • $N^{+/-}$: Number of scattered electrons (off deuteron only) for each helicity state (+/-).
- ⁴⁰² • $N_{e^-}^{+/-}$: Number of incident electrons for +/- helicity states
- ⁴⁰³ • $P_b P_t$ = Product of the beam and target polarizations
- ⁴⁰⁴ • $\Delta\Omega = \sin\theta \cdot \Delta\theta \cdot \Delta\phi$: The solid angle for the given kinematic bin. This term includes the “detector acceptance”.

407 • $\eta_{detector}$ accounts for the detector efficiencies

408 The data analysis to extract the physics quantities involves accurately
409 measuring each of these quantities, either separately or in some combined
410 form. To do so, the data must be properly reconstructed, calibrated and
411 corrected to build all the scattering events during the experiment. Since
412 the reconstructed events include a wide range of physical processes in ad-
413 dition to the electron-deuteron scattering process that we are interested in,
414 proper event selection cuts must be applied. In this chapter, all these steps
415 from the data reconstruction and calibration through the extraction of g_1 are
416 described.

417

418 **3.1 Raw Data Processing - Calibration and** 419 **Reconstruction**

420 The raw data recorded by the CLAS DAQ system, which consists of ADC
421 and TDC values registered by various detector components as well as the
422 beam related information such as beam helicity and Faraday Cup readings,
423 are organized into banks (with each bank carrying data belonging to a par-
424 ticular detector component or some part of it) and saved in special format
425 (BOS) files. These raw data are next processed with a standard CLAS soft-
426 ware package called RECSIS, which analyzes and combines the matching bits
427 and pieces of the raw information to reconstruct particles and events that
428 produced them. Such reconstruction produces output data that consist of
429 event and particle IDs, particle positions and energies and momenta (in the
430 lab frame CLAS coordinate system), and also some static particle properties
431 such as charge and mass. The reconstruction program uses geometric pa-
432 rameters and calibration constants (from the CLAS Calibration Database)
433 for the detector in order to properly process and transform the raw data into
434 the reconstructed tracks.

435 The first part of the data processing is the detector calibration. In this
436 phase, a small sample (about 10%) of raw data (uniformly selected over the
437 entire run period to ensure time stability verification) is chosen and the en-
438 ergy and time calibration constants are adjusted to give the correct behavior
439 while constantly monitoring related variables. This is done separately for
440 each run period to consider the different running conditions, the possibility

441 of unwanted changes in hardware that may have occurred, as well as drift
442 of detector response over time. This process of adjusting the calibration
443 constants and reconstructing the data is repeated until a desired level of ac-
444 curacy is reached. Once that level is reached, the calibration constants are
445 “frozen” and the final reconstruction is done. The resulting output is saved
446 in especial formats¹. These saved data provided the starting point for our
447 higher level data analysis as described in this document.

448 The iterative work of data reconstruction and detector calibration, which
449 was a very computing intensive and time consuming, was done by R. De Vita
450 (in 2006-2007) soon after the data collection was completed, which has been
451 summarized in the analysis note [20] by X. Zheng which has been approved
452 by the hadron spectroscopy working group. This analysis, meanwhile, has
453 been published [21]. The data from this “Pass1” reconstruction was first
454 analyzed as part of the Ph. D. dissertations by three graduate students, but
455 during these analyses, a few anomalies² in reconstruction were observed which
456 were later tracked down to a mixing up of codes from two EG4 sub-packages
457 for the reconstruction software. After the mix-up was sorted out, a new
458 pass (Pass2) of reconstruction was performed by L. El Fassi in 2014/15 (still
459 using the same calibration constants as used by the Pass1 reconstruction).
460 The data from this latest pass of reconstruction was used for the analysis
461 reported in this note

¹Two especial data formats - BOS and ntuple (h10) - were used

²The anomalies observed in the pass1 analysis were the discretized reconstruction of vertex and wrong reconstruction of track positions in DC1.

462 **3.2 Helicity States**

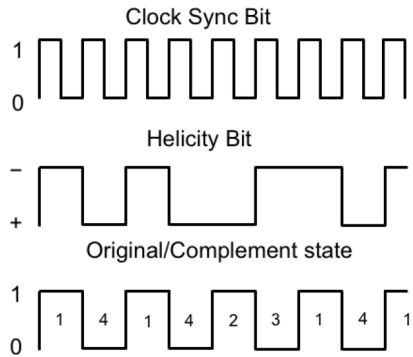


Figure 3.1: Different data signals sent from the injector that monitor the helicity states of beam electrons. (Fig. courtesy of N. Guler [22]).

463 As we saw from Eq. 3.1, the physics extraction depends on measurements of
464 the number of events in the two (+/-) electron helicity states. The CEBAF
465 accelerator provides the polarized electrons in closely and equally spaced
466 bunches. These bunches are further grouped into “buckets” according to
467 their helicity states, which are alternated pseudo-randomly at the injector
468 with a frequency of 30 Hz. The information on the helicity state of each of
469 the buckets and the total integrated charge contained in it is injected into the
470 DAQ data stream immediately after the helicity flip. Using a combination of
471 different types of sequence control signals sent from the injector (see Fig. 3.1),
472 it is possible to determine which helicity state a particular event belonged
473 to, which then can be used to label the helicity state of the event in the data
474 stream, together with the total beam charge of the state.

475 **3.3 Electron Identification**

476 In CLAS electron-scattering experiments, the scattered electron defines the
477 timing of each event. In addition, in inclusive measurements, the scattered

478 electron is the only particle to be detected and measured. So, it is particu-
479 larly important to make sure that electrons are well measured and properly
480 identified and are not contaminated with misidentified particles such as neg-
481 ative pions (π^-) or lost by being misidentified.

482 The process of identifying the primary scattered electrons starts by first
483 rejecting all those particle candidates which are not the first entries (i.e., the
484 trigger particles) in the event bank. The remaining sample of the candidates
485 is refined further by rejecting those with positive charges. Then, the sample
486 is further refined by applying a set of cuts that are listed and described below.
487 An electron candidate is considered good if it passes all of these cuts.

488 **1. Good Electron Cuts**

- 489 (a) **Cut on particle charge:** $q=-1$
- 490 (b) **Detector status cuts:**
 - 491 i. **DC status:** $dc>0; dc_part>0$
 - 492 ii. **SC status:** $sc>0; sc_part>0$
 - 493 iii. **EC status:** $ec>0; ec_part>0$
 - 494 iv. **CC status:** $cc>0; cc_part>0$
495 (For simulated data, all of the above except those on CC
496 variables are used.)
- 497 (c) **Electromagnetic Calorimeter Cuts** (see Sec. 3.3.1)
- 498 (d) **Osipenko cuts** Cuts on CC angle θ , ϕ and time matching be-
499 tween CC and other detectors. (see Sec. 3.3.2)
- 500 (e) **Cut on minimum number of photoelectrons** (see Sec. 3.3.2)

501 **2. Good Event Cuts**

- 502 (a) **Cut on minimum number of particles detected and recon-
503 structed in the event:** $gpart>0$
- 504 (b) **Minimum/maximum momentum cuts** (see Sec. 3.3.3)
- 505 (c) **Sector cut** $dc_sect = 6; cc_sect = 6$ (to select electrons from the
506 sector where the low momentum Cherenkov detector was installed)
- 507 (d) **Scattering vertex-z cuts** (see Sec. 3.3.4)
- 508 (e) **Fiducial cuts** (see Sec. 3.3.5)

509 This data analysis relied on comparing the experimental data with a
510 Monte-Carlo simulated data set that was as realistic as practically possible.
511 Thus, we also have to analyze the simulated data in the same way as the
512 experimental data. In the ideal situation, all cuts would be the same for
513 both experimental and simulated data. However, we could not make our
514 simulation match perfectly with our experimental data. Therefore, some of
515 the data selection cuts are defined separately for the two cases and sometimes
516 separately even for different Q^2 bins (to make sure we have the same fractions
517 of events in corresponding kinematic bins for both type of data).

518 **3.3.1 Electromagnetic Calorimeter Cuts**

519 The EC cuts consist of two different cuts applied together. One of these
520 is on the sampling fraction i.e. the fraction of the energy deposited in the
521 calorimeter, and the other is on the energy fraction deposited in the inner
522 part of the calorimeter.

523 **Cuts on EC sampling fraction**

524 While moving through the EC, charged pions are minimum ionizing particles
525 in the momentum range detectable by CLAS. On the other hand, each elec-
526 tron deposits its total energy E_{tot} in the EC³ by producing electromagnetic
527 showers. Therefore, the sampling fraction E_{tot}/p should be independent of
528 the momentum for electrons (in reality there is a slight dependence).

³Because some of the deposited energy is in the lead part of the EC rather than the scintillator, only a fraction of the electron energy is detected in the EC.

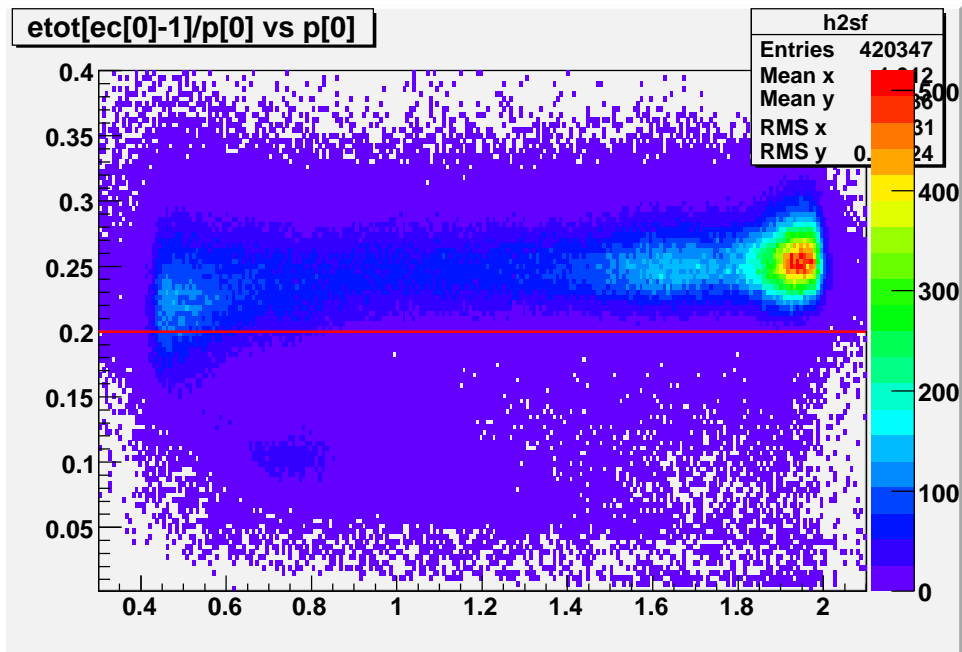


Figure 3.2: An example of the cut on the EC sampling fraction (2.0 GeV data). The plots shows the distribution of the sampling fraction (in Y-axis) plotted against the particle momentum (in X-axis). The brighter stripe above about 0.2 in the energy fraction are due to the electrons whereas those below are the pions.

529 For the EC in CLAS, the electron sampling fraction ($etot/p$) is about 0.25
530 and pions give signals that are mostly below 0.2 (see Fig. 3.2 or others that
531 follow). Therefore, a lower cut of $etot/p > 0.2$ is usually chosen to reject
532 most of the pions without significantly losing good electrons. However, in
533 our low beam energy experiment, few pions are produced and the electron
534 peaks are cleaner in lower kinematic bins as can be seen in the low Q^2 bins
535 of Fig. 3.3. Therefore, a Q^2 bin dependent cut of $etot/p > (\mu - 3\sigma)$ was
536 chosen, where μ and σ are the Gaussian fit parameters representing the mean
537 and standard deviation of the distribution in the corresponding Q^2 bin. The
538 choice of 3σ was decided by looking at the sampling fraction distributions in
539 each of the Q^2 bins and making sure that no pion signal was observed in any
540 of the bins.

541 On simulated data also, a corresponding 3σ cut was applied by first re-
542 peating the exact same procedure to get the corresponding values of μ and
543 σ from the simulated data. Using same- σ cuts in corresponding Q^2 bins of
544 both experimental and simulated data ensures that we had the same fraction
545 of data in corresponding bins from both experimental and simulated sides.

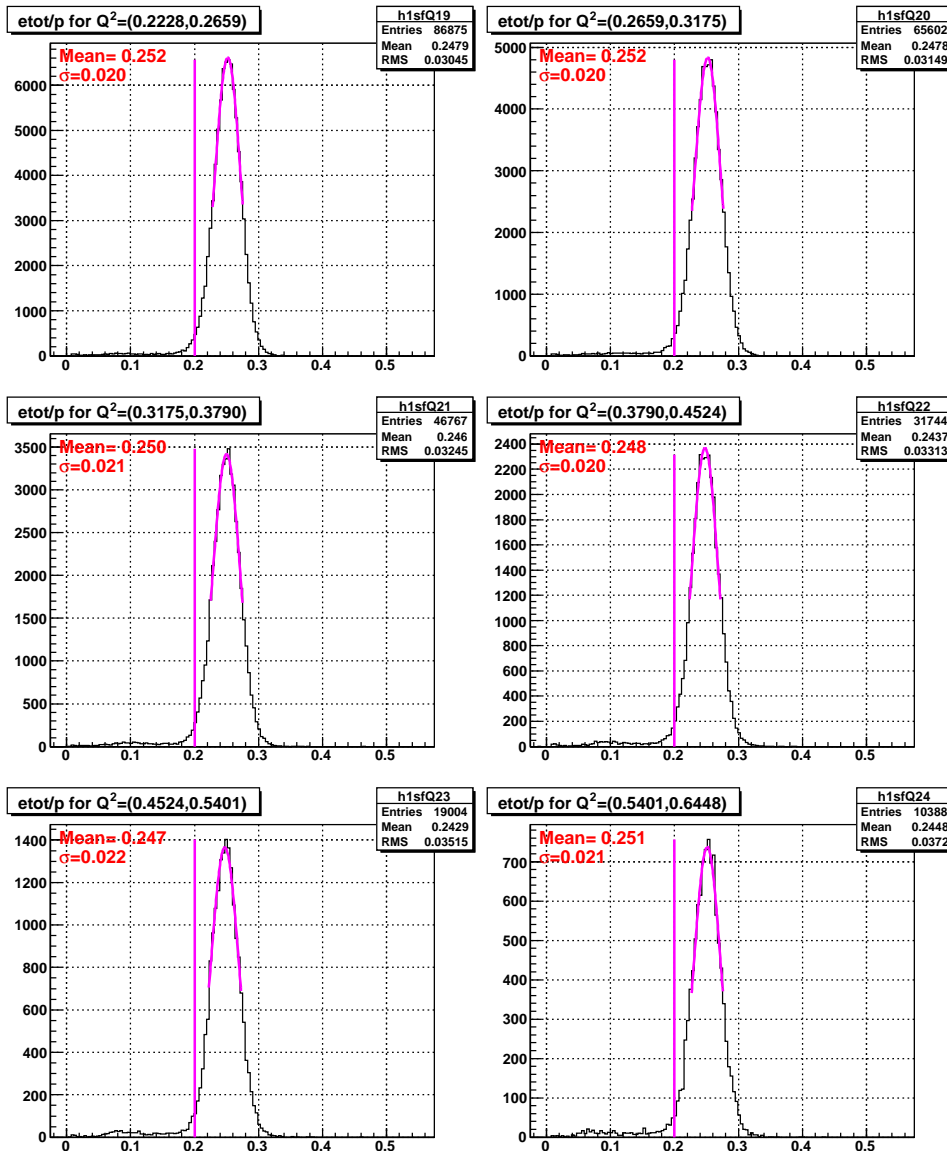


Figure 3.3: The Q^2 dependent cuts on the EC sampling fraction for 2.0 GeV experimental data. Events below the red lines are rejected.

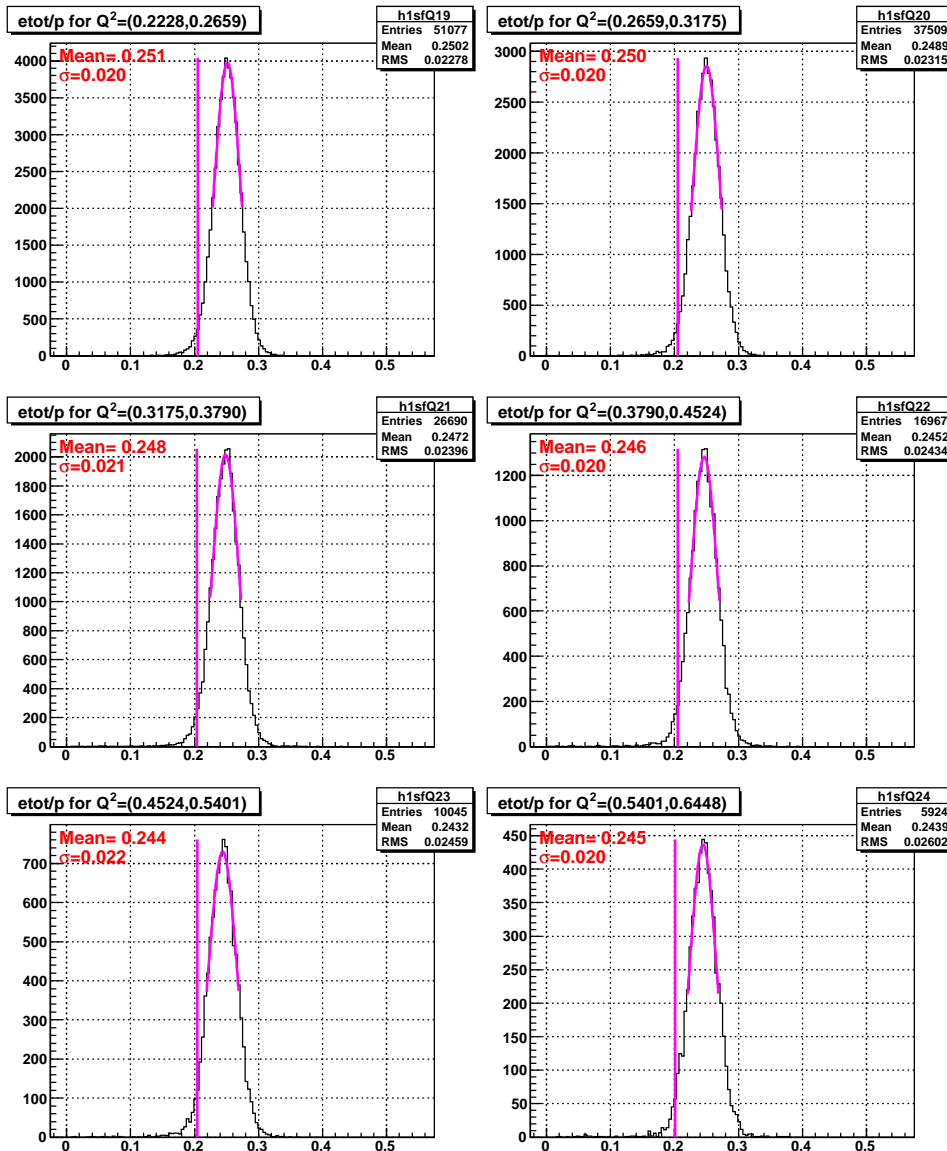


Figure 3.4: The Q^2 dependent cuts on the EC sampling fraction for 2.0 GeV simulation data. Events below the red lines are rejected.

546 **Cuts on E_{in}**

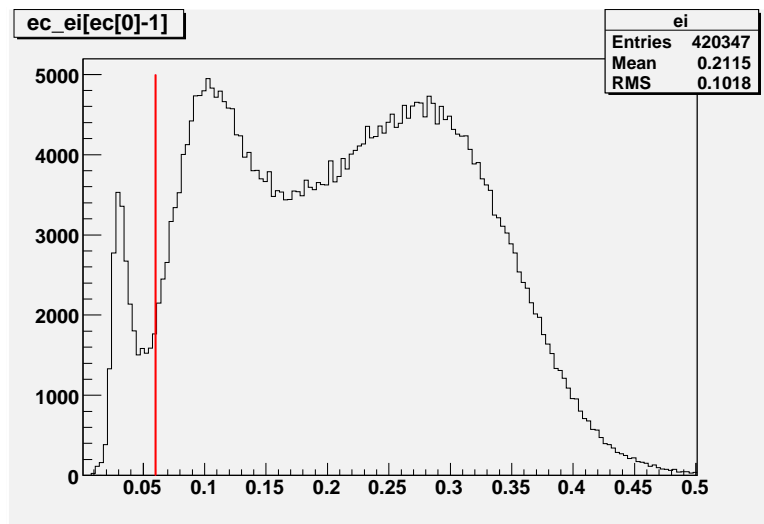


Figure 3.5: Energy deposited (GeV) in the inner EC and the cut (red line) used to reject pions (seen as a peak at about 0.03 GeV) from a sample of electron candidates of 2.0 GeV data.

547 Pions, which do not shower and are minimum ionizing particles in the
548 momentum range detected in CLAS, deposit only a small amount of energy
549 in the inner part of the EC, independent of their momentum. When E_{in} is

550 histogrammed, the small pion signal peak at about 0.03 clearly stands out
551 from the large electron sample, with little overlap in between. So, a universal
552 cut of $E_{in}=0.05$ on both data and simulation (as shown by figures 3.5, 3.6
553 and 3.7) safely rejects most of the pions from the electron candidate sample.

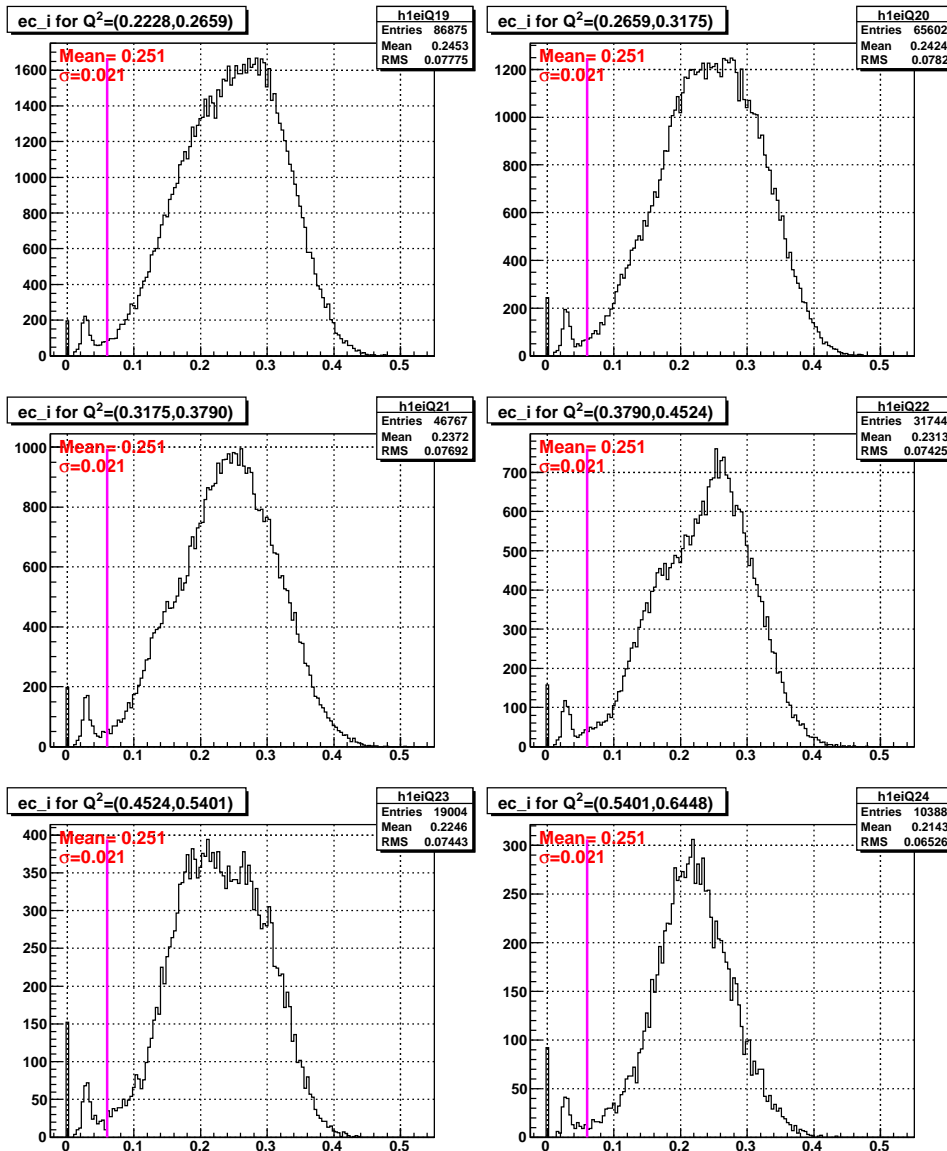


Figure 3.6: The EC-inner cut on a sample of 2.0 GeV experimental data in various Q^2 bins.

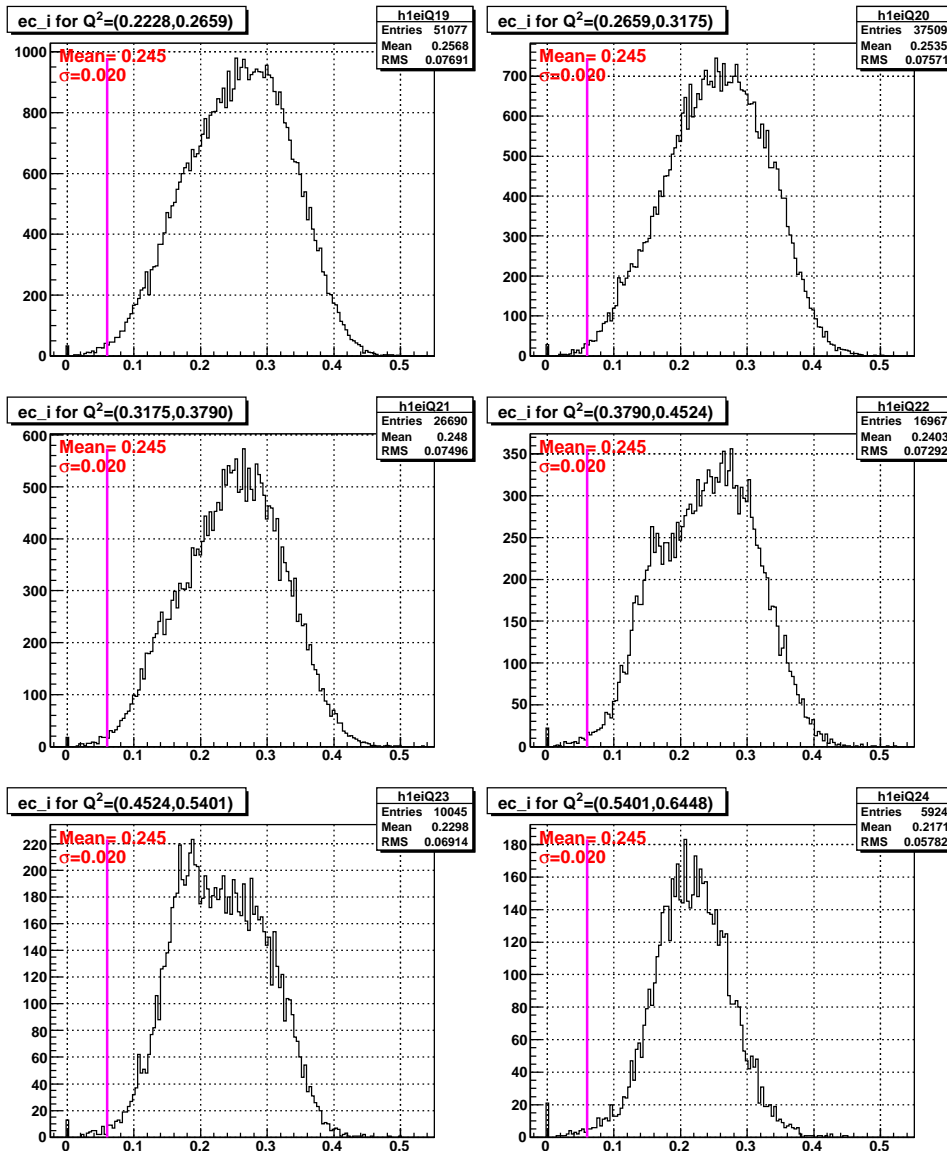


Figure 3.7: The EC-inner cut on a sample of 2.0 GeV simulation data in various Q^2 bins.

554 **3.3.2 Cerenkov Counter Cuts**

555 **Osipenko (CC Geometry and Time Matching) Cuts**

556 As discussed in Sec. 2 the new EG4-dedicated CC consists of 11 modules
557 each consisting of a pair of mirrors and PMTs. The segments are placed
558 along the CLAS polar angle covering 15 to 45 degrees, i.e., the segments are
559 at different polar angular positions. During normal operation, the PMTs of
560 these segments may produce thermal noise that is equivalent to that produced
561 by one photo-electron passing through it. As a result, when a noise pulse in
562 the CC and a pion track measured by DC coincides within the trigger window
563 of the CLAS detector, the track gets registered as an electron candidate by
564 the event reconstruction program, thus contributing to the contamination of
565 electron candidates with the misidentified pion tracks. In fact, this turns out
566 to be the biggest source of pion contamination. In order to minimize such
567 contamination and help better identify electrons from pions, CC geometric
568 and time-matching cuts are applied.

569 This category of cuts for this experiment is mostly based on a similar
570 analysis done for another CLAS experiment by M. Osipenko [20, 23].

571 The first requirement in the CC-matching is for the electron candidate
572 track (as reconstructed by DC) to have a corresponding signal in CC. In ad-
573 dition, the track needs to meet several matching conditions to be acceptable
574 as described in the next sections.

575 **CC θ Matching** As said above, the CC segments are at different average
576 polar angle positions (between 15 and 45 degrees), so in principle, one can
577 expect a one-to-one correspondence between the polar angle of the track (as
578 measured at the vertex) and the CC-segment. However, the torus magnetic
579 field bends the particles towards or away from the beamline, so it's more
580 convenient to use the CC projected polar angle θ_{proj} rather than the vertex
581 angle θ , where θ_{proj} is defined as the polar angle of the position vector defined
582 by the point of intersection of the track with the plane at which the CC
583 PMTs reside as reflected by the CC mirrors (another projected angle ϕ_{proj}
584 is the azimuthal angle of the same vector). These projected angles can be
585 uniquely calculated for each track based on the DC signals of the track as
586 well as the CC geometry information. To simplify the later analysis process,
587 these projected angles for each track were calculated during the final data
588 reconstruction process and then saved in the output files just like all the other

589 information for the events and particles. Finally, for the actual electrons
 590 a one-to-one correspondence between θ_{proj} and the segment number can be
 591 established, which discriminates against background noise and the accidental
 592 pions (or any other negative charge candidates). For each segment, the θ_{proj}
 593 distribution (see Fig. 3.8) is fitted with a gaussian to determine its mean (μ)
 594 and width (σ) and then saved for future use in cuts. These fit parameters
 595 are then used during the data analysis to define these CC- θ -matching cuts.
 596 The events that have $\mu - 3\sigma < \theta_{proj} < \mu + 3\sigma$ pass this cut, and the others
 597 are rejected as not genuinely being electrons.

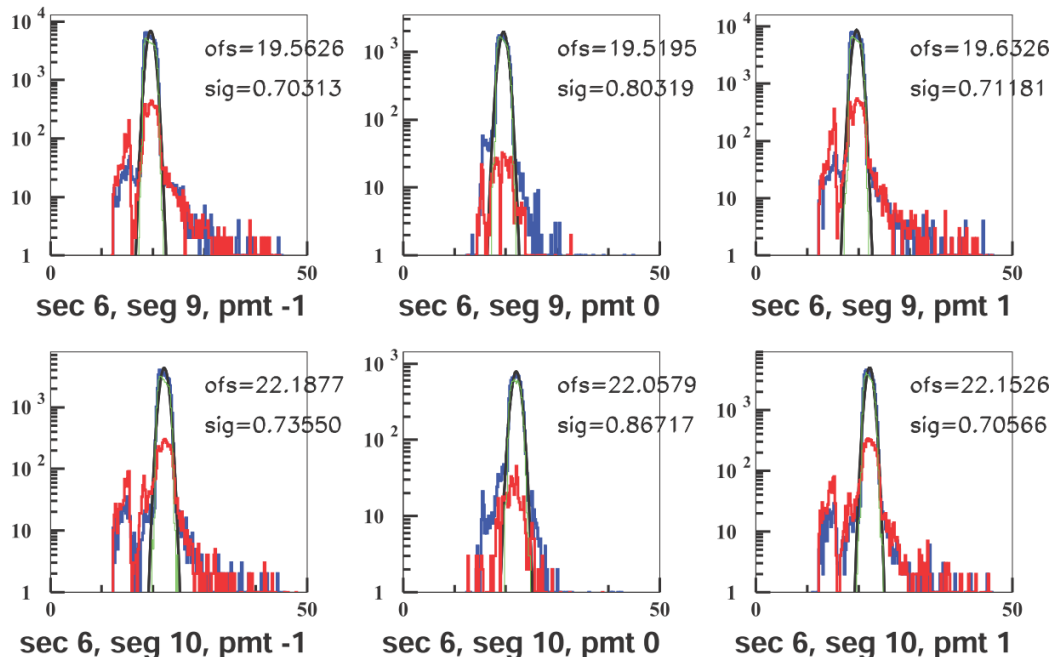


Figure 3.8: The θ_{proj} distributions in two (9th and 10th) of the CC-segments (figures used from [20]). Here, the first, second and third columns correspond to events that fired the left, both and the right PMTs respectively. The blue lines are for good electron candidates that pass the EC cuts as well as $Nphe > 2.5$. The red ones are for those that pass the EC cuts but with $Nphe < 2.5$ (thus likely pions), and the green lines (not visible due to being nearly identical to the blue ones) are for those which pass both EC cuts and all Osipenko cuts. The Gaussian fits which are used to define the θ matching cuts are shown in black ("ofs" and "sig" in the panel refer to μ and σ , respectively). If the candidate falls outside $\pm 3\sigma$ limits given by the fit, θ_{proj} is taken as not matching with the corresponding segment and, therefore, the event is rejected.

598 **CC ϕ Matching** One can also have a one to one correspondence between
599 the other CC-projected angle ϕ_{proj} and the left or right PMT in the corre-
600 sponding CC-segment, because when the track is on the right side of the CC,
601 the right PMT should fire and vice versa. However, there are some excep-
602 tional cases of events which fire both PMTs. That happens when ϕ_{proj} of the
603 track is less than 4 degrees (when measured relative to the sector mid-plane),
604 in which case the Cerenkov light hits both PMTs but with less efficiency (be-
605 cause the Cherenkov photons are shared between the two). Fig. 3.9 shows
606 for two of the segments the ϕ_{proj} distributions and the Gaussian fits that are
607 used to define these cuts.

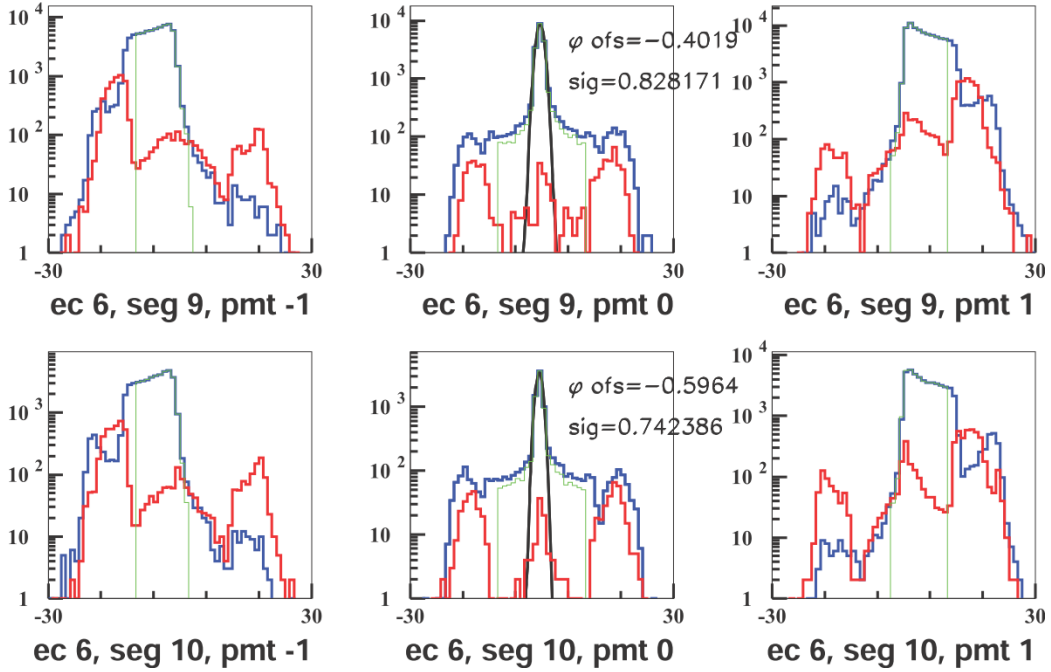


Figure 3.9: The ϕ_{proj} distributions in two (9^{th} and 10^{th}) of the CC-segments (figure used from [20]). Here, the first, second and third columns correspond to events that fired the left, both and the right PMTs respectively. The blue lines are for good electron candidates that pass the EC cuts as well as $Nphe > 2.5$. The red ones are for those that pass the EC cuts but with $Nphe < 2.5$ (thus likely pions), and the green are for those which pass both EC cuts and all Osipenko cuts. The Gaussian fits to the distributions that fired both left and right PMTs are shown in black ("ofs" and "sig" in the panel refer to μ and σ , respectively). If the candidate falls outside 3σ on the positive (negative) side but the left (right) PMT is fired, we take it as having left-right inconsistency and, therefore, the event is rejected. In other words, if $\theta < \mu - 3\sigma$ but $PMT = 1$, or if $\theta > \mu + 3\sigma$ but $PMT = -1$, the event is rejected.

608 **CC Time Matching** The difference ΔT between the track time recorded
 609 on a CC segment and the corresponding time recorded on the TOF (or SC),
 610 corrected for the path length from the CC to the TOF, is used to define one of
 611 the time-matching cuts $\Delta t_{SC-CC} > -6.0\text{ns}$ which was chosen to reduce pion
 612 contamination without losing too many electron candidates (see Fig 3.10).
 613 Likewise, the time between CC and EC is also used to define another cut
 614 $\Delta t_{EC-CC} > -6.0\text{ns}$ (see Fig 3.11) to further reduce the pion contamination.

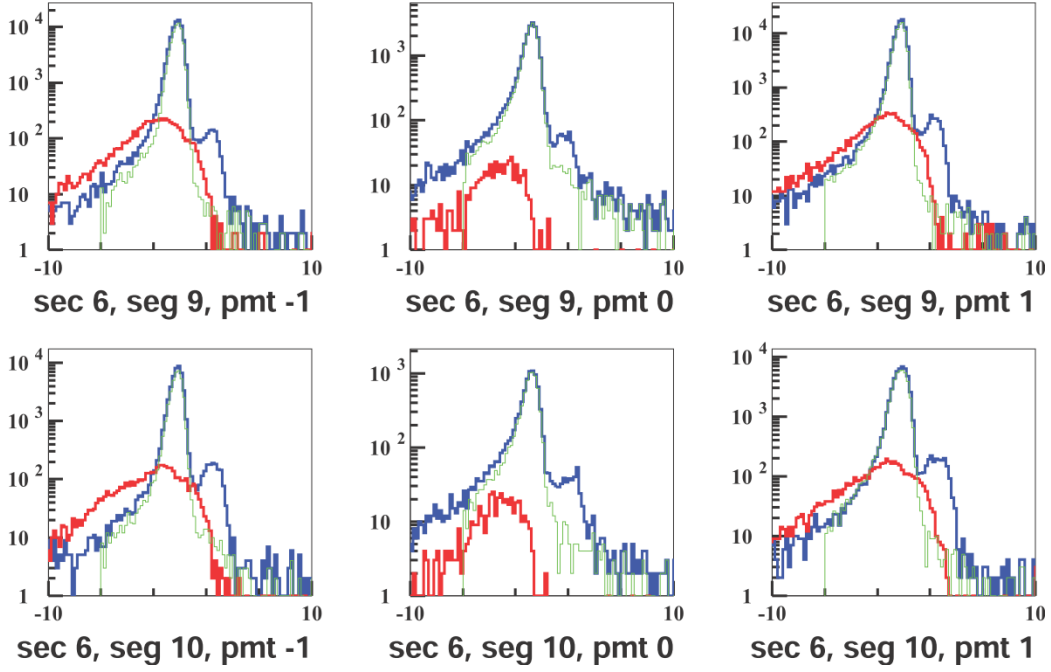


Figure 3.10: The Δt_{SC-CC} distributions for two of the CC-segments (figure used from [20]). Here, the first, second and third columns correspond to events that fired the left, both and the right PMTs respectively. The blue lines are for good electron candidates that pass the EC cuts as well as $Nphe > 2.5$. The red ones are for those that pass the EC cuts but with $Nphe < 2.5$ (thus likely pions), and the green are for those which pass both EC cuts and all Osipenko cuts. The $\Delta t_{SC-CC} > -6.0\text{ns}$ cut was chosen to reduce pion contamination without losing too many electron candidates. (The small peaks at about +3 ns are due to particles hitting PMTs directly.)

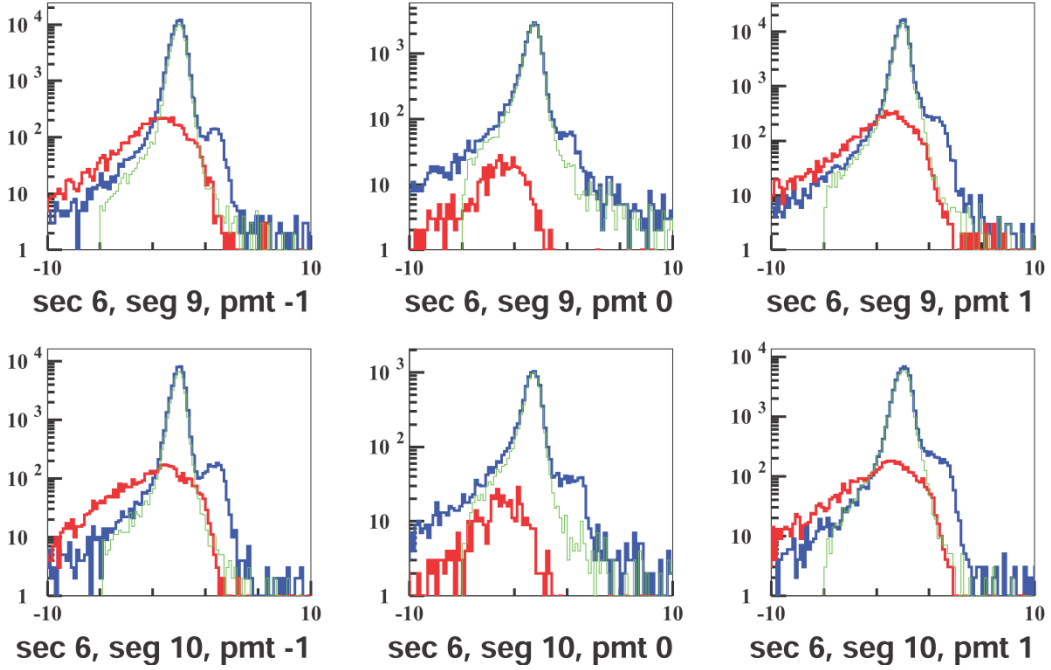


Figure 3.11: The Δt_{EC-CC} distributions for two of the CC-segments (figure used from [20]). Here, the first, second and third columns correspond to events that fired the left, both and the right PMTs respectively. The blue lines are for good electron candidates that pass the EC cuts as well as $Nphe > 2.5$. The red ones are for those that pass the EC cuts but with $Nphe < 2.5$ (thus likely pions), and the green are for those which pass both EC cuts and all Osipenko cuts. The $\Delta t_{EC-CC} > -6.0\text{ns}$ cut was chosen to reduce pion contamination without losing too many electron candidates. (The small peaks at about +3 ns are due to particles hitting PMTs directly.)

615 Cut on Minimum Number of Photoelectrons

616 The “nphe” variable in the data ntuple which represents the ADC signal from
 617 the CC converted to “number of photoelectrons” and multiplied by 10 is also
 618 used to discriminate electrons from pions and the background. The number
 619 of photoelectrons produced in CC by an electron is typically between 5 and 25
 620 or between 50 and 250 in the units of nphe, where the electronic background
 621 and negative pions produce signals equivalent to one photo-electron (or 10 in
 622 nphe units) and so a cut is determined somewhere between these two regions
 623 based on the shapes and sizes of the electron and pion peaks. In our case,

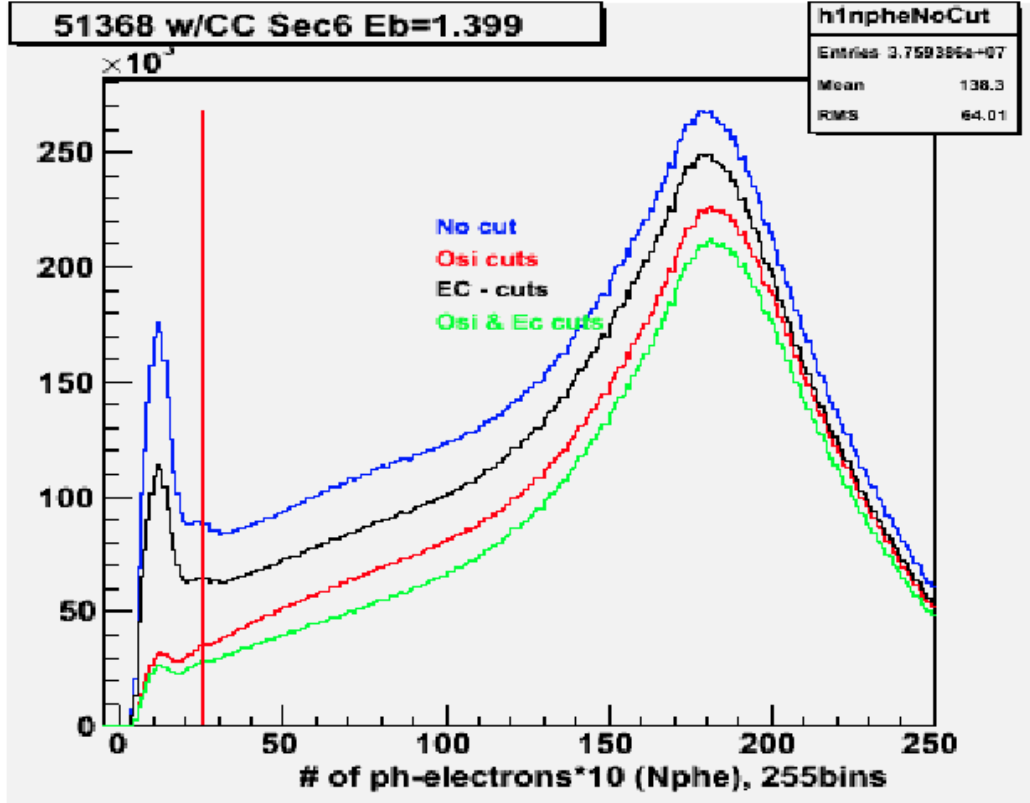


Figure 3.12: The cut (the red straight line at 25) on the number of photo-electrons produced in CC times 10 (from 1.3 GeV data). The signals below the red line are mostly pions and noise and above the line are mostly electrons. We also see the effects of overall EC cuts, overall Osipenko cuts and the effect of both when applied together.

⁶²⁴ we chose to have the cut $Nphe > 25$ as depicted by the straight line in Fig.
⁶²⁵ 3.12.

⁶²⁶ 3.3.3 Minimum/Maximum Momentum cuts

⁶²⁷ A study [24] of the inclusive cross section at various beam energies in CLAS
⁶²⁸ developed a parametrization of the low momentum cut p_{min} as a function of
⁶²⁹ the calorimeter low trigger threshold (in milli-Volts)

$$p_{min} \text{ (MeV)} = 214 + 2.47 \times EC_{threshold} \text{ (mV)} \quad (3.2)$$

630 The low threshold for EC-total energy for EG4 was 65 mV [25], so, the
 631 minimum momentum cut was determined to be at: $p_{min} = 0.37 \approx 0.4$ GeV.
 632 In addition, another minimum cut of $p_{min} = 0.2 * E_{beam}$ was added, so the
 633 actual minimum cut amounted to the larger of those two. Likewise, the
 634 momentum cannot be more than that of the beam energy (in natural units),
 635 therefore, the upper cut on the momentum is: $p_{max} = E_{beam}$.

636 Fig. 3.13 shows the momentum distribution of the electron candidates
 637 for the 2 GeV data and the minimum and maximum cuts.

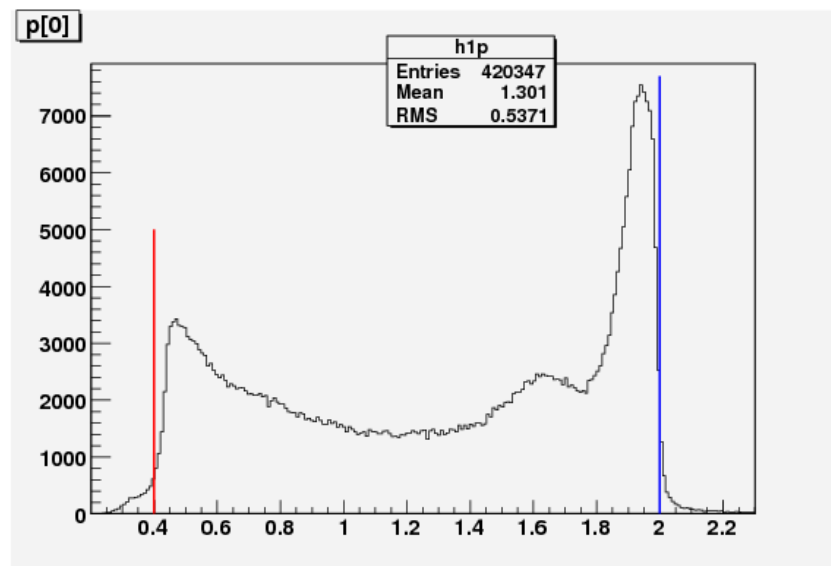


Figure 3.13: The maximum and minimum momentum cuts (on 2.0 GeV ND₃ data).

638 3.3.4 Vertex-Z cuts

639 In the EG4 experiment, the ND₃ polarized target was of 1 cm long and was
 640 placed at ($x = 0$, $y = 0$, $z = -100.93$ cm) in the CLAS coordinate system.
 641 Since the beam electrons have to go through a few foils before reaching the
 642 target as well as the detector, we want to reject electron tracks with vertices
 643 outside the target volume. For this purpose, use a cut on the reconstructed
 644 vertex co-ordinate “ v_z ”. However the vertex resolution demands reasonably
 645 wide “ v_z ” cuts so as not to lose too many good events. That is why the
 646 distribution of “ v_z ” was studied and based on the position and width of
 647 the distribution as well as our knowledge of the location of various foils and

648 target materials, the cuts on “ v_z ” were decided. It was seen (see Figs. 3.14
 649 and 3.15) that the resolutions get worse and the distributions get wider as
 650 we go to lower Q^2 values, so again Q^2 dependent cuts were chosen for both
 651 data and simulation with the cuts tightening as Q^2 increases.

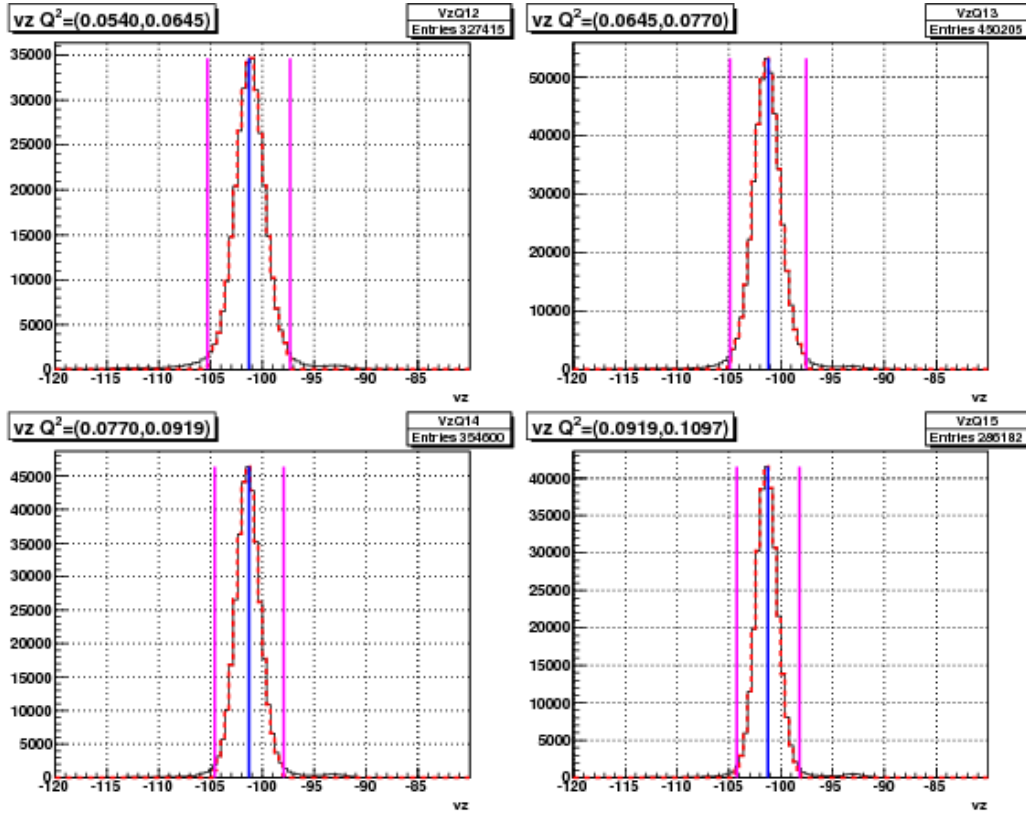


Figure 3.14: 2.0 GeV data showing the Q^2 dependent v_z -cuts (the magenta lines on the left and right of the peaks) in some of the Q^2 bins. The continuous black line represents events before applying all the other event selection cuts (except on v_z) and the thicker dotted red line are the events after the cuts. The blue lines are the centers of the distributions, from which the cuts are 3 times σ away on each side, where σ is the standard deviation for the distribution in the given Q^2 bin (both the central value and the σ are determined during the cut development studies).

652 As in the case of EC variables, the reconstructed “ v_z ” distribution in
 653 the simulation does not come out quite the same as in the experimental
 654 data . To have the same fraction of events in the corresponding Q^2 bins as

655 in the experimental data, a separate set of cuts (determined based on the
 656 distributions of both types of data) had to be used for simulation. For this
 657 purpose, the Gaussian fit parameters μ and σ (representing the mean and
 658 standard deviation) for all the Q^2 bins were tabulated separately for both
 659 data and simulation and separate sets of $\pm 3\sigma$ cuts were determined for all
 660 bins. For example, if μ_q and σ_q were the two Gaussian fit parameters for the
 661 q^{th} Q^2 bin of either data or simulation, then the lower and upper cuts for
 662 “ v_z ” for that data set in the given Q^2 bin would be $\mu_q - 3\sigma_q$ and $\mu_q + 3\sigma_q$
 663 respectively (as shown by the magenta vertical lines in Figs. 3.14 and 3.15).

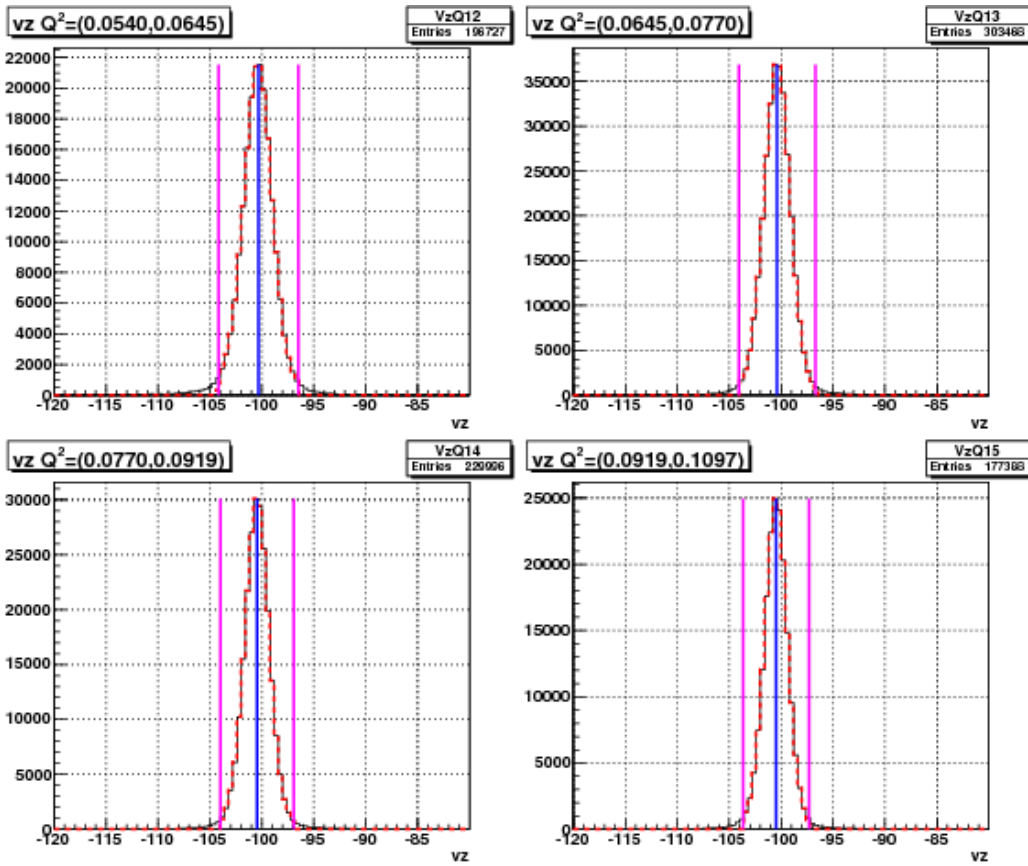


Figure 3.15: Q^2 dependent v_z -cuts on simulation data (similar to Fig. 3.14).

664 **3.3.5 Fiducial Cuts**

665 Similar to the cuts discussed so far, we also had to match the region of good
666 efficiency of the physical detector with the corresponding region from the
667 simulation. For the experimental and simulation data to be comparable,
668 they must have the same detector acceptance. Two event variables polar
669 angle (θ_{vtx}) measured at the vertex and the azimuthal angle ϕ_{DC1} measured
670 at the drift chamber layer 1 are chosen to define the good efficiency regions of
671 the detector. The reason for the choice of the variable θ_{vtx} should be obvious
672 because it is directly related with the kinematic variables Q^2 and W used in
673 the analysis. However, due to the momentum dependent rotational effect of
674 the magnetic field on the reconstructed azimuthal angle (ϕ_{vtx}) at the vertex,
675 the angle ϕ_{DC1} is preferred over ϕ_{vtx} to define the fiducial region because
676 that allows the easy selection (rejection) of the events which passed through
677 and got detected by the more (less) reliable central (marginal) regions of
678 the Cerenkov Counters. After a careful and extensive study of the event
679 distributions on both data and simulation, we arrived at four sets of fiducial
680 cuts in terms of the variables θ_{vtx} , ϕ_{DC1} and the torus current normalized
681 inverse momentum i.e., $I_{torus}/(2250p)$.

682 The first set (see Fig. 3.16) of fiducial cuts were determined by comparing
683 regular and EC-only data (which were taken using triggers that didn't
684 involve CC) and selecting cuts such that regions with relatively darker spots
685 (reflecting very low CC-efficiency) were rejected.

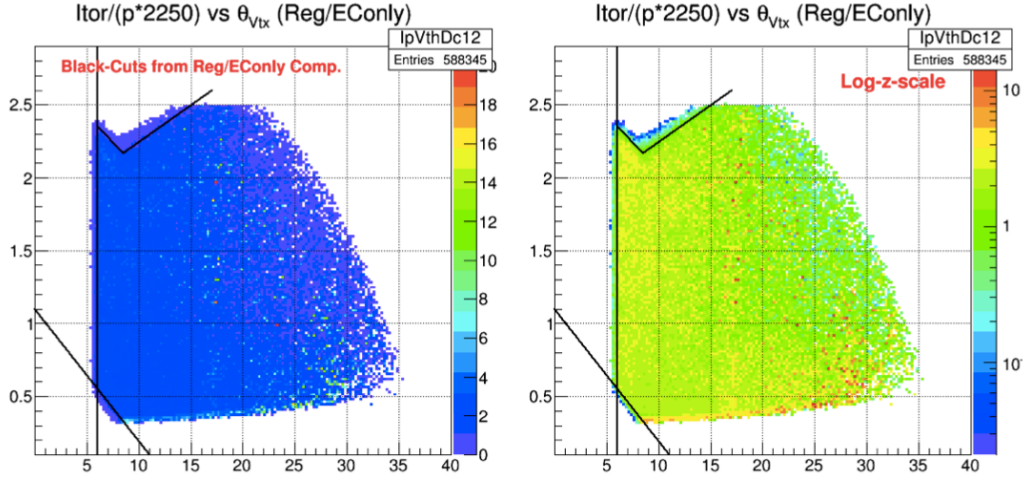


Figure 3.16: Fiducial cuts determined by comparing the distributions of regular and EC-only **experimental data** as a function of $I_{torus}/(2250p)$ and θ_{vtx} . Here in the top panels, we see distributions of ratios of the regular and EC-only data respectively in linear and log scales in the color axis respectively. Inefficient regions of the CC are excluded using the indicated cuts.

686 The second set of cuts came from a similar comparison between the regu-
 687 lar and EC-only data in the $I_{torus}/(2250p)$ vs θ_{vtx} (instead of θ_{DC1}) space (see
 688 Fig. 3.17) .

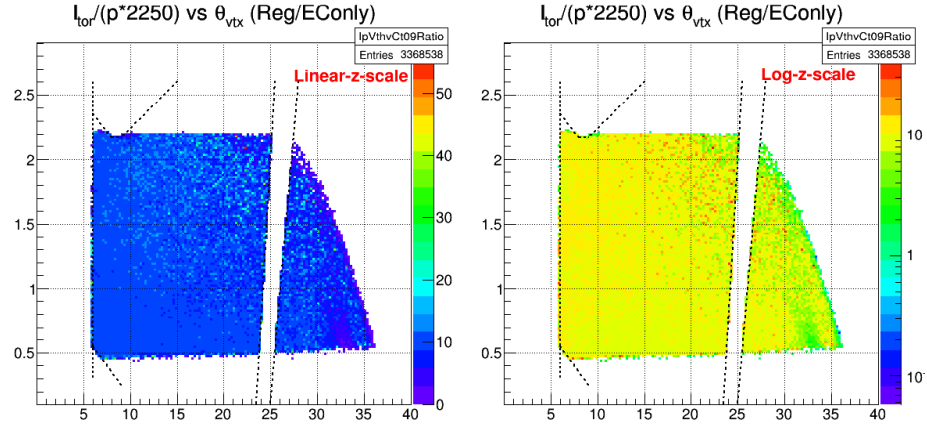


Figure 3.17: Fiducial cuts determined by comparing the distributions of regular and EC-only **experimental data** as a function of $I_{torus}/(2250p)$ and vertex angle θ_{vtx} . Here, the vertical cut near $\theta_{vtx}=25$ degrees is to avoid the region of low efficiency possibly due to dead wires in DC.

689 The third set of cuts came from a comparison between the experimental
 690 and the corresponding simulated data as shown in the Fig. 3.18. as indicated
 691 by various straight lines in the two plots.

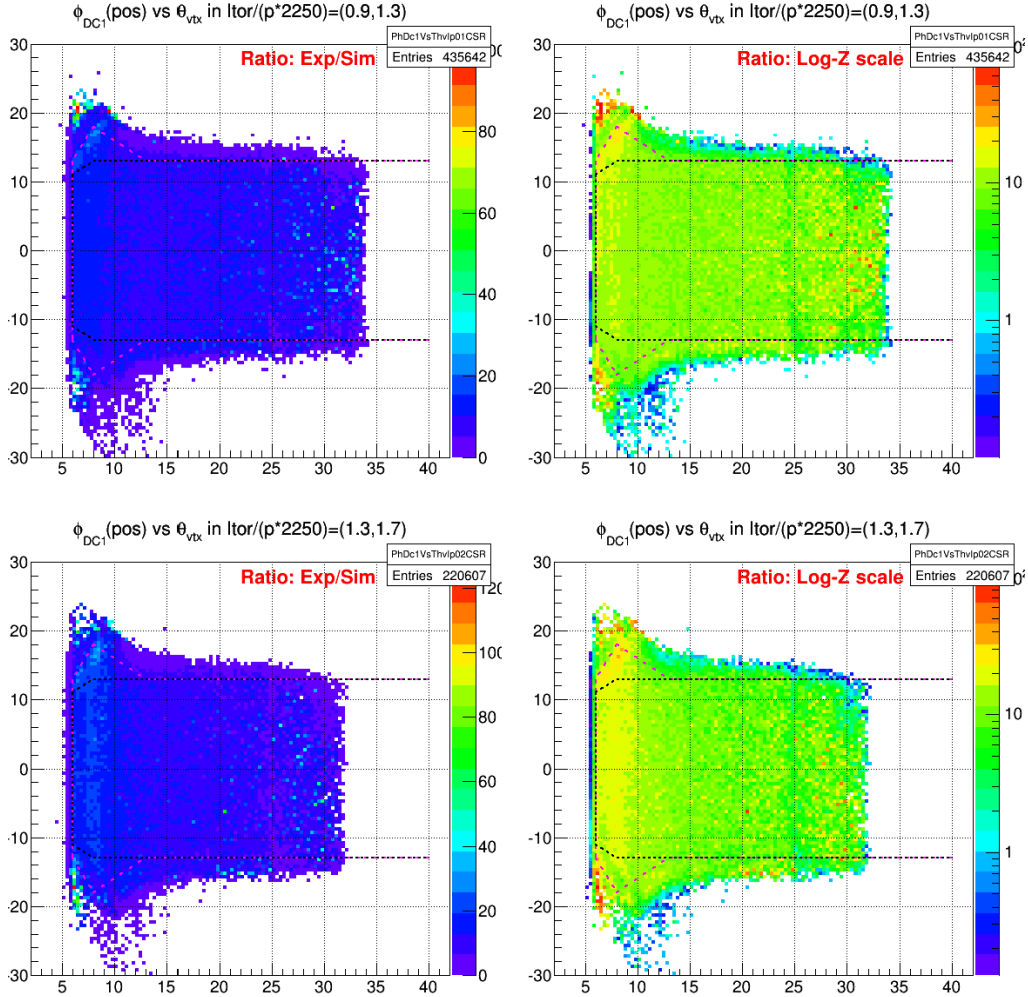


Figure 3.18: Distribution (in two of six bins of $I_{torus}/(2250p)$) of ratios of **experimental** and **simulated** data (for 2.0 GeV) (both in linear and log-z scales) as a function of vertex angle θ_{vtx} and azimuthal angle ϕ_{DC1} as measured by the track position at the first drift chamber layer (angles in degrees). The dotted lines indicate the fiducial cuts for accepting good electrons.

692 Lastly, further sets of cuts were developed based on the distribution of
 693 the average number of photo electrons (nphe) as recorded by the Cerenkov
 694 Counter (CC) (see Fig. 3.21).

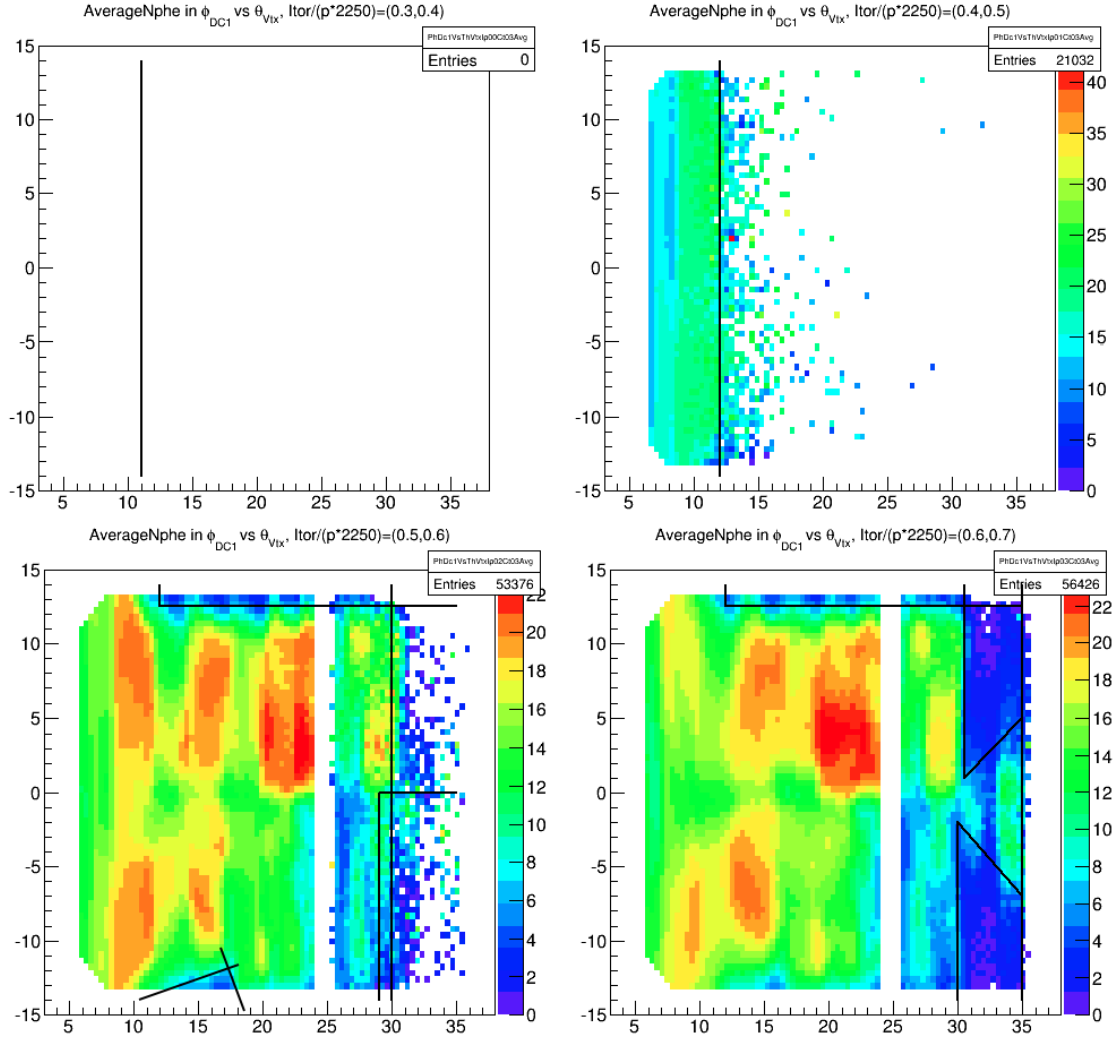


Figure 3.19: Average Nphe distributions as a function of ϕ_{DC1} (along Y-axis) and θ_{vtx} (along X-axis) in first four bins of $\frac{I_{tor}}{p \cdot 2250}$. The black lines show the cuts that reject the very low CC-inefficiency regions.

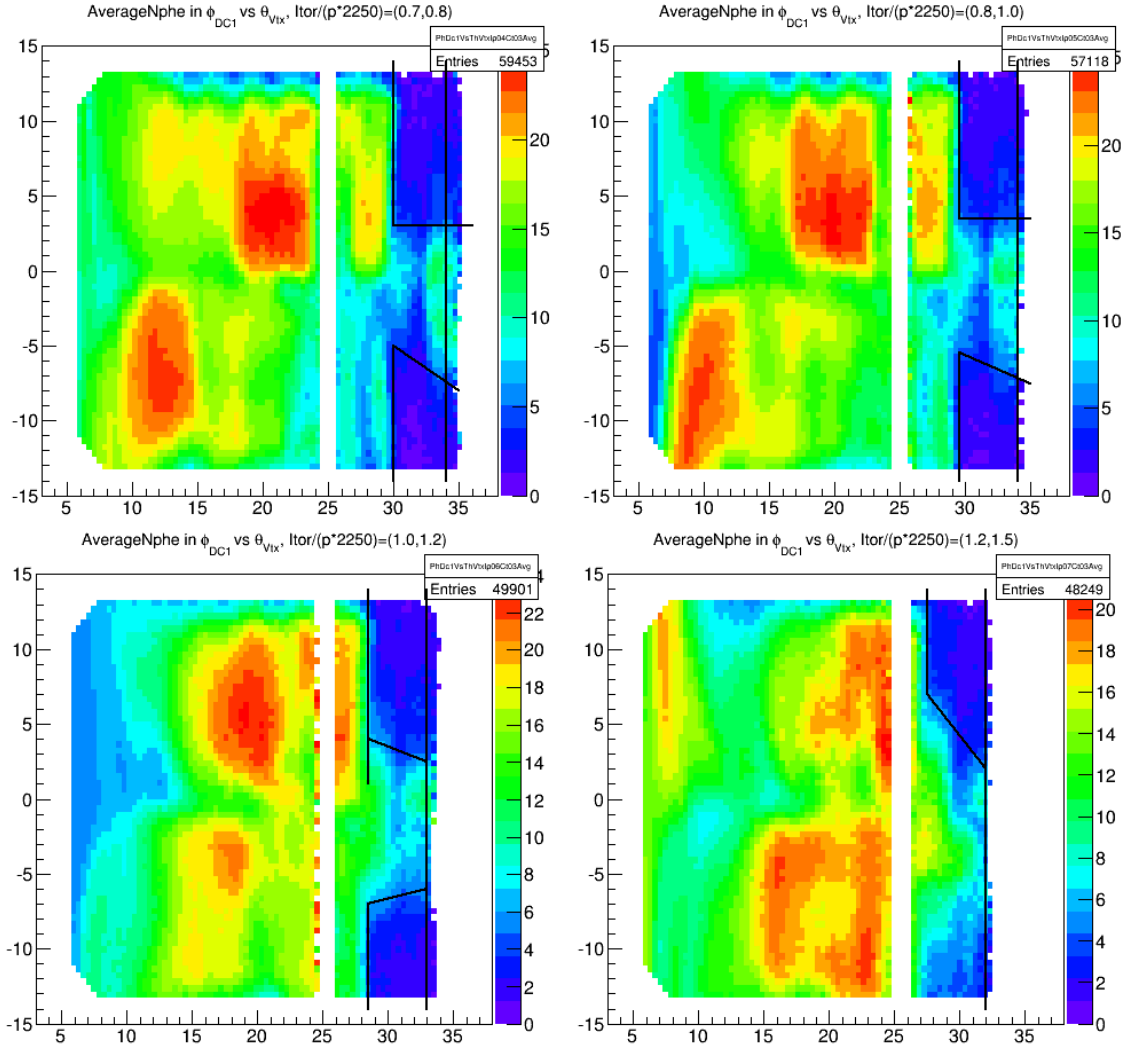


Figure 3.20: Average Nphe distributions as a function of ϕ_{DC1} (along Y-axis) and θ_{vtx} (along X-axis) in next four bins of $\frac{I_{tor}}{p \cdot 2250}$. The black lines show the cuts that reject the very low CC-inefficiency regions.

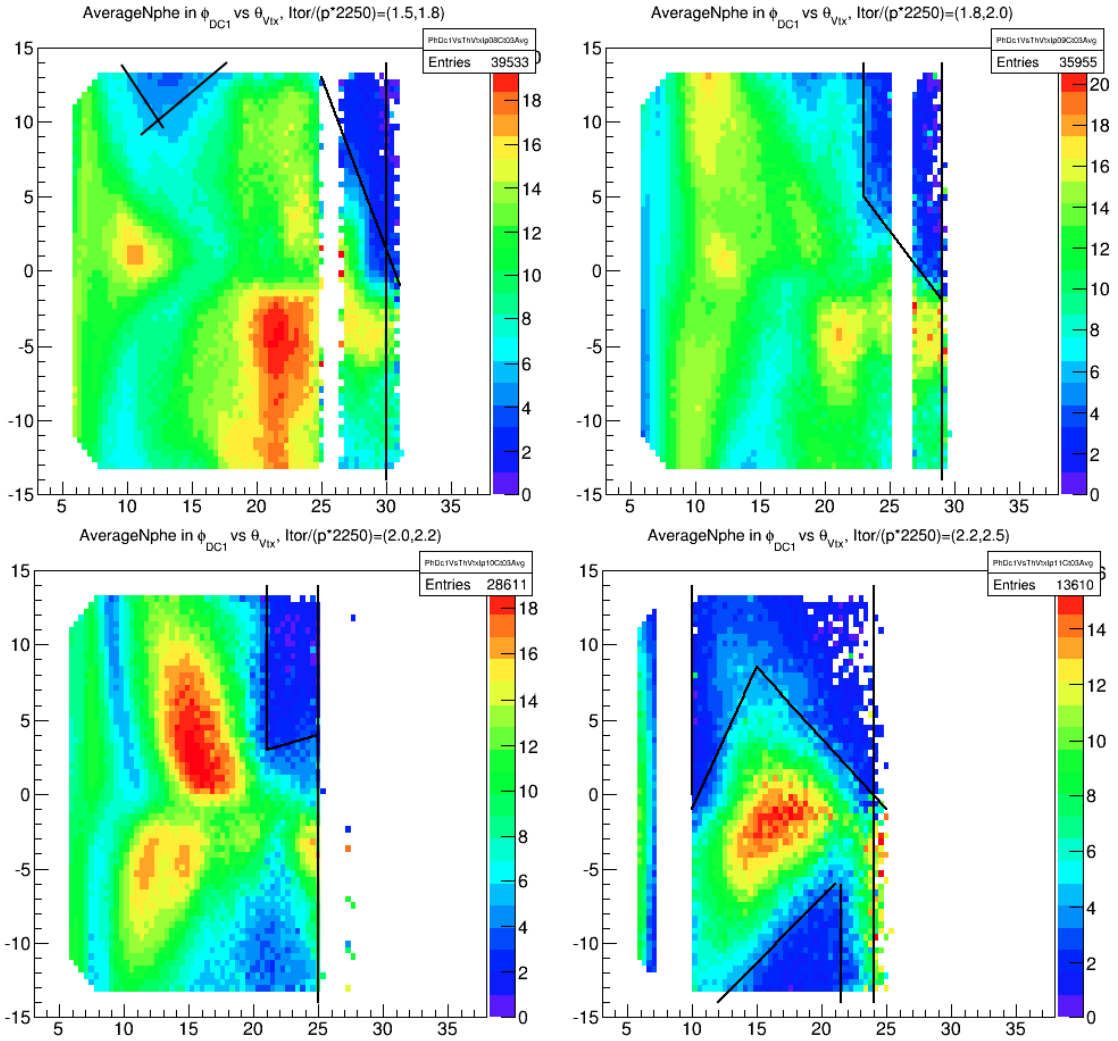


Figure 3.21: Average Nphe distributions as a function of ϕ_{DC1} (along Y-axis) and θ_{vtx} (along X-axis) in last four bins of $\frac{I_{tor}}{p^*2250}$. The black lines show the cuts that reject the very low CC-inefficiency regions.

695 3.4 Data Quality and Stability Checks

696 With an available set of good event/electron selection cuts, beam charge
697 (measured by Faraday cup) normalized total event counts (sometimes also
698 known as event “yield”), as well as polarization dependent differences, were
699 calculated for each of the data files for all the runs and then plotted against
700 the run number to study the data quality and stability as shown by Figs.
701 3.22, 3.23 and 3.24.

702 If nothing unusual happened or if the experimental conditions are not
703 changed, then it is expected that the event yield as well as the count differ-
704 ences remain constant over time. Therefore, the graphs of these event counts
705 plotted versus time or run number (which also roughly reflect the flow of
706 time) should indicate the stability and quality of the data collected. For
707 example, Fig. 3.22 shows such a total yield plot for all the data files from
708 the 2.0 GeV beam energy data set on deuteron target. We can see that these
709 data runs display some features of instability over the full period of time, but
710 stability over short time periods. For example, all the data with run numbers
711 below about 51610 show significantly higher event yield than the runs after
712 that run (possibly due to beam-target misalignment as indicated by raster
713 magnet ADC values in Fig 3.24).

714 Likewise, the stability of the polarized count differences in the elastic
715 region ($0.9 \text{ GeV} < W < 1.0 \text{ GeV}$) as well as separately in the delta (Δ)
716 resonance region were studied by plotting them versus the same run numbers
717 (here the elastic and Δ -resonance regions are considered separately, because
718 the spin asymmetries in these two regions have opposite signs, which would
719 have decreased the observed difference if combined. To further enhance the
720 sensitivity of the observation, the difference of the count differences measured
721 in the elastic and Δ -resonance regions as given by

$$\Delta N_{elastic} - \Delta N_{\Delta-res} = \frac{1}{P_b P_t} \left[\left(\frac{N^+}{FC^+} - \frac{N^-}{FC^-} \right)_{elastic} - \left(\frac{N^+}{FC^+} - \frac{N^-}{FC^-} \right)_{\Delta} \right] \quad (3.3)$$

722 were plotted (see Fig. 3.23). It was observed that this elastic normalized
723 count difference (which is what really matters to our analysis, in the end)
724 was much more stable than the total yield.

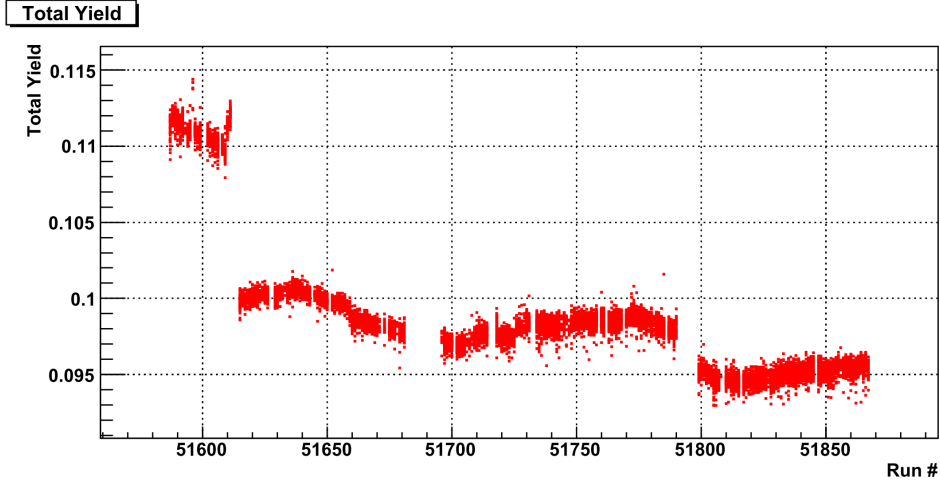


Figure 3.22: Total normalized yield ($= \frac{N^+ + N^-}{FC^+ + FC^-}$) for 2.0 GeV ND₃ runs.

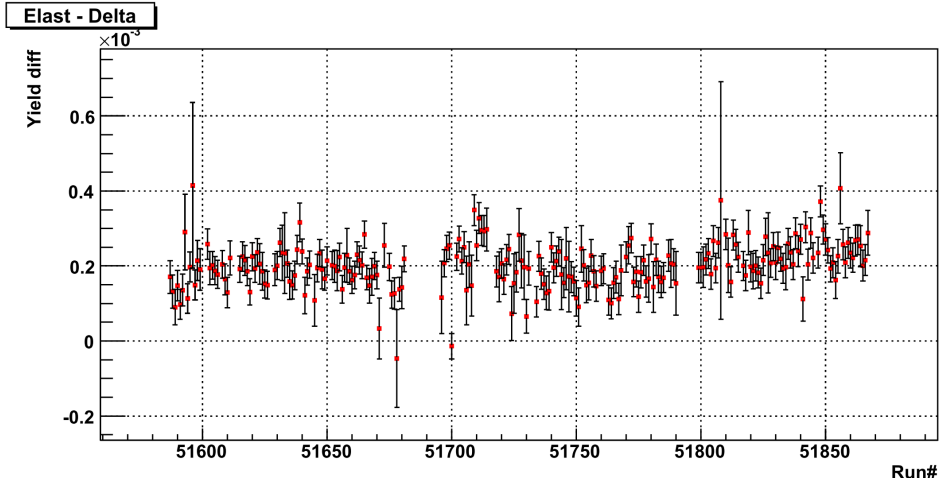


Figure 3.23: Polarized yield differences (Eq. 3.3) normalized with $P_b P_t$ and BPM/F-cup for elastic peak minus that for the Δ peak for the 2.0 GeV ND₃ runs.

725 The same was also repeated for the other variables such as the root-
 726 mean-square of the ADC values (see Fig. 3.24) which carry information on
 727 the X and Y coordinates of the beam at the interaction vertex, thus their
 728 plots giving us somewhat more direct information on whether there was any
 729 misalignment between the beam and the target.

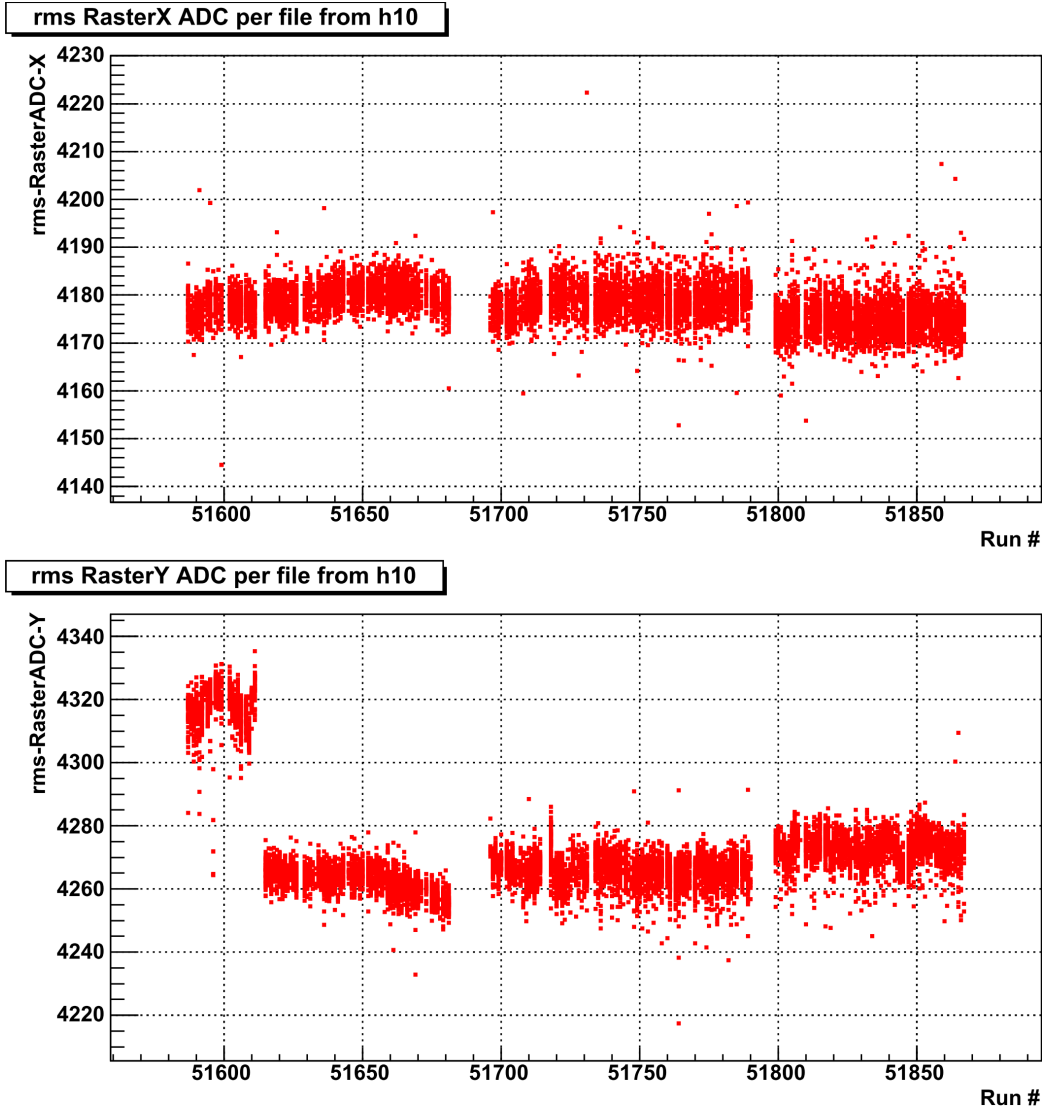


Figure 3.24: Root-mean-square of the ADC values for the raster magnet currents in the directions X and Y. The distributions show a larger raster size in the y-direction for the first group of runs, indicating that the beam may have been hitting the edges and the walls of the target or other more dense structure support materials, thus explaining the higher total yield for the corresponding runs as shown by the Fig. 3.22. This does not affect our final analysis because these off-target materials are not polarized and, hence, do not contribute to the polarization dependent count difference (ΔN) used in the final analysis.

730 Based on the studies of these quality and stability plots, the data runs
731 were divided into subgroups with each beam energy data set. In each sub-
732 group, the data showed more stability than over the whole run period for
733 the given beam energy. For example, in case of the 2.0 GeV deuteron data,
734 the runs were divided into four distinct sub groups corresponding to the four
735 separate bands as seen in the Fig. 3.22. These subgroups were later treated
736 and analyzed separately to get the corresponding normalized polarized count
737 differences (with all data runs from each subgroup combined together). After
738 the initial combination within the subgroups, they were again combined into
739 the grand total by properly considering the half-wave-plate status, and the
740 target polarization directions.

741 **3.5 Kinematic Corrections**

742 The reconstructed event vertices and associated particle 4-momenta are slightly
743 off from their true values for several reasons. First, RECSIS does not take
744 into account the fact that the beam is rastered in polarized target experi-
745 ments. Next, any imperfections and mis-alignments of detectors and other
746 components of the experimental set-up are not accounted for. Furthermore,
747 the torus field map is not known precisely. In addition, the effects of multiple-
748 scattering and particle energy losses are not considered in RECSIS. There-
749 fore, to get more accurate results from the data analysis, the data quality
750 must be improved by applying various kinematic corrections. Following is
751 the list of the corrections that were applied for the analysis:

- 752 1. Incoming (beam) energy loss correction (due to ionization)
- 753 2. Tracking corrections
- 754 3. Drift chamber dependent momentum correction
- 755 4. Outgoing energy loss correction (due to ionization after scattering)

756 **3.5.1 Incoming Energy Loss Correction**

757 The first correction listed above considers the loss of beam energy due to
758 atomic collisions before the actual nuclear scattering takes place. A good
759 estimate for this loss is 2 MeV on average [26, 27], which is subtracted from

760 the nominal beam energy. This correction is applied during the analysis
761 whenever the beam energy is involved⁴, and therefore it is not included in
762 the correction package described below.

763 3.5.2 Tracking Corrections

764 This work is mostly based on the work documented in the EG1-DVCS-TN-
765 004[29] , in which a routine or method is developed to swim the particles
766 through the field map of the target magnet to the drift chambers in order
767 to determine the particle angles and position at the target, provided the di-
768 rection cosines of the tracks at DC and the beam position from the raster
769 magnets are known. It is expected that the method improves both the angu-
770 lar resolution and the reconstructed longitudinal vertex position. The slightly
771 modified version of the corresponding C/C++ routine is used with some of
772 the constants in the routine replaced by new parameters to be determined
773 by the method of **χ^2 -square minimization** using ep-elastic events. (Since
774 this data set didn't have enough e^+e^- pairs, we didn't use them in the min-
775 imization like in the EG1DVCS.)

776 Method

777 First of all, in order to convert raster magnet ADCs into corresponding
778 beam positions x_0 and y_0 , we need conversion parameters. These param-
779 eters are determined by using a method outlined in EG1-DVCS-TN-002[30].
780 The method determines the values of the slopes and offsets that convert the
781 X- and Y-raster ADC readings to corresponding beam positions x_0 and y_0
782 in cm by minimizing the sensitivity of target vertex position (v_z) for charged
783 tracks to beam motion.

784 Next, ep-elastic events are skimmed (from all of the NH_3 target data-
785 set) using electron ID cuts for the electrons (see section 3.3) in the sixth
786 sector and proton ID consisting mainly of the time-of-flight cuts are used to
787 select protons in the third sector (opposite to the sixth one). Then missing
788 momentum cuts (less than 0.1 GeV for each of the four components P_x ,
789 P_y , P_z and E) based on 4-momentum conservation requirements (within
790 measurement uncertainties) are used to help further clean up the accidental

⁴The beam energies that we used were derived from the Hall A and Hall C Tiefenback energies or the MDSY1c or MDSY3c energies[28]

791 coincidences. These skimmed events are saved in root files and later reused
792 for the minimization process described here.

793 The cuts used in the initial data skimming required that each of the four
794 missing components $(Px, Py, Pz, E)_{miss}$ be less than 0.1 GeV.

795 After that a correction routine involving a set of correction equations
796 with several unknown parameters are established. Then with the help of
797 TMinuit (ROOT version of Minuit), several sets of trial values are given to
798 these unknown parameters and the corresponding correction is applied to
799 the particles in the skimmed events. For each set of these trial values, a
800 specifically defined χ^2 (see below) is evaluated looping over all the skimmed
801 events and the Minuit tries to find the optimum set of these parameter values
802 for which the χ^2 is minimum. Such an optimal set of values are chosen as
803 the correct values of these parameters and is used in the eventual correction
804 routine.

805 **The correction routine**

806 The routine uses 17 constants (free parameters determined by the above
807 mentioned process of χ^2 -minimization) and the following input and output
808 variables:

- 809 • **Input variables:** $x_r, y_r, \text{cxd}, \text{cyd}, \text{xdc}, \text{ydc}, \text{zdc}, p, q$.

810 – x_r, y_r are x & y beam positions as returned by the raster correction
811 routine (see appendix)
812 – **cxd, cyd** are direction cosines of the track as measured at DC1
813 – **xdc, ydc, zdc** are the coordinates of the track measured at DC1
814 – p, q are the momentum and charge of the track

- 815 • **Output variables:** cxc, cyc, czc, vzc (all three corrected direction
816 cosines and the corrected Z-coordinate at the vertex) .

817 The sequence of calculation steps taken (inside the routine) to arrive at the
818 output results are as follows (where, I am also using the notations of P.
819 Bosted i.e., subscripts '0' used to indicate variables at vertex, subscript 'f'
820 for those at the drift chambers (these are the tl1_ variables in the ntuples),
821 and the values of (x, y, z) are in cm):

- 822 • First of all, get ready the following constants and variables:

- 823 – $f_c = \frac{B}{50} = 0.995$ is the overall field correction
 824 * (i.e., the $B.dl$ correction factor. Our $B = 4.97T$, with B in
 825 kG f_c is 0.995)
 826 – $targsign = 1$
 827 – $\theta_f = \arccos(cz_{dc})$
 828 – $\phi_f = \text{atan2}(cy_{dc}, cx_{dc})$
- 829 • Then, θ_f is corrected (for the misalignment of the DC) as follows:
- 830 – If it's the electron in the event,
 831 * $\theta_f = \theta_f + (\text{par}[0] + \text{par}[1] \times \phi_f) \frac{\cos\theta_f}{\cos\phi_f} + (\text{par}[2] + \text{par}[3] \times$
 832 $\phi_f) \sin\theta_f$
 833 – else if its the proton,
 834 * $\theta_f = \theta_f + (\text{par}[4] + \text{par}[5] \times \phi_f)$
- 836 • Next, get ϕ_0 without raster corrections yet
- 837 – $\phi_0 = \phi_f + targsign \times f_c (0.186 + \text{par}[10] + (0.045 + \text{par}[11]) \theta^2 +$
 838 $(0.008 + \text{par}[12]) \theta_f^3 + (0.0032 + \text{par}[13]) \theta_f^3/p^2) \frac{q}{p}$
- 839 • Correction to polar angle from focusing effect. First, get focusing term
 840 for beam (x,y)=0.
- 841 – $\delta\theta = f_c (0.90 \theta_f + 1.2 \theta_f^3)/(100 p^2)$
- 842 • Displacement of beam along trajectory (x_p) and perpendicular to it
 843 (y_p)
- 844 – $x_p = x_r \cos\phi_0 + y_r \sin\phi_0$
 845 – $y_p = -(x_r + \text{par}[6]) \sin\phi_0 + (y_r + \text{par}[7]) \cos\phi_0$
- 846 • Correction to $\delta\theta$ from radial target field, which only depends on raster
 847 x and y but not vertex z. Also, no effect on peak at zero!
- 848 – $\delta\theta = \delta\theta (1. + targsign q p (0.5/\theta_f) (y_p/0.75))$

849 • Now can get cz

850 – $\theta_0 = \theta_f + \delta\theta$

851 – $cz_c = \cos\theta_0$

852 • Now ϕ_0 again, this time including raster correction

853 – $\phi_0 = \phi_f + \text{targsign } f_c (0.186 + \text{par}[10] + (0.045 + \text{par}[11]) \theta^2 +$
854 $(0.008 + \text{par}[12]) \theta_f^3 + (0.0032 + \text{par}[13]) \theta_f^3/p^2) \frac{q}{p} (1 - (0.09 +$
855 $\text{par}[14]) \frac{0.35 - \text{par}[15]}{\theta_f} x_p)$

856 • Get cx and cy using this cz

857 – $cx_c = \sin\theta_0 \cos\phi_0$

858 – $cy_c = \sin\theta_0 \sin\phi_0$

859 • Renormalize czc

860 – $cz_c = \sqrt{1.0 - cx_c^2 - cy_c^2}$

861 • Apply target field rotation correction

862 – $cx_c = cx_c - \text{targsign } q \text{par}[8] cz_c/p$

863 – $cy_c = cy_c + \text{targsign } q \text{par}[9] cz_c/p$

864 • Renormalize again:

865 – $czc = \sqrt{1.0 - cx_c^2 - cy_c^2}$

866 – $\theta_0 = \arccos(cz_c)$

867 • Get vertex z in cm

868 – $r_{dc} = \sqrt{(x_{dc} - x_r)^2 + (y_{dc} - y_r)^2}$

869 – $Z_c = Z_{dc} - \frac{r_{dc} - (22 + \text{par}[16]) \cos\theta_0 (\tan\theta_0 - \tan\theta_f)}{\tan\theta_f}$

870 • Finally, the routine outputs (returns) the four corrected quantities

871 – cx_c, cy_c, cz_c, Z_c .

872 **Calculation of χ^2 (to be minimized)**

873 The chi-square has different components as follows:

874 $\chi^2 = \chi_{\text{Zvar}}^2(\mathbf{e}) + \chi_{\text{Zvar}}^2(\mathbf{p}) + \chi_{\text{Evar}}^2 + \chi_{\text{miss}}^2 + \chi_{\text{Ppen}}^2 + \chi_{\text{Epen}}^2 + \chi_{\text{Zpen}}^2 + \chi_{\Delta E}^2$
 875 where,

- 876 • $\chi_{\text{Zvar}}^2(\mathbf{e})$ and $\chi_{\text{Zvar}}^2(\mathbf{p})$ are Z-variance contributions from electron and
 877 proton candidates in the ep-elastic events and are calculated as $\chi_{\text{Zvar}}^2 =$
 878 $\frac{1}{N_{ep}-1} \left(\sum Z_c^2 - \frac{(\sum Z_c)^2}{N_{ep}} \right) / (0.05)^2$ separately for the electrons and protons.
 879 (Here, Z_c is the corrected Z of vertex and N_{ep} is the number ep-elastic
 880 events used in the minimization)
- 881 • $\chi_{\text{Evar}}^2 = \frac{1}{N_{ep}-1} \left(\sum E_b^2 - \frac{(\sum E_b)^2}{N_{ep}} \right) / (0.005)^2$ is E_b -variance contribution.
 882 (Here, $E_b = M_p \left(\frac{1}{\tan(\theta_p)\tan(\theta_e/2)} - 1 \right)$ is the beam energy calculated after
 883 the angles are corrected by the correction routine.)
- 884 • $\chi_{\text{miss}}^2 = 100 \times \left(\frac{\sum p_x^2(\text{miss}) + \sum p_y^2(\text{miss})}{0.02^2} + \frac{\sum p_z^2(\text{miss}) + \sum E^2(\text{miss})}{0.05^2} \right)$ is missing
 885 four-momentum contribution. (Here, 100 is an arbitrary number to
 886 make the weight of this contribution comparable to others.)
- 887 • $\chi_{\text{Ppen}}^2 = \sum_{i=0}^{16} \frac{(par[i] - iPar[i])^2}{0.01^2}$ is the contribution due to runaway penalty
 888 on free parameters of the minimization. (Here, par[i] & iPar[i] are the
 889 current and initial values of the 'i'th parameter. In the first iteration,
 890 initial values were set to either zeros or the corresponding values as
 891 determined for EG1-DVCS by P. Bosted. In later iterations, they were
 892 set to the values determined from the previous iteration of the mini-
 893 mization.)
- 894 • $\chi_{\text{Zpen}}^2 = \sum_{e,p} \left(\sum_{N_{ep}} \frac{(Z_c - (-100.93))^2}{0.05^2} \right)$ is a penalty term when Z_c runs away
 895 from the known/nominal target center (-100.93 cm)
- 896 • $\chi_{\text{Epen}}^2 = \sum_{i=2}^4 \left(\frac{\sum_{N_{ep}} E_b}{N_{ep}} - E_0 \right)^2 / (0.005)^2$ is a penalty term to constrain E_b
 897 running away from the nominal values E_0 of beam energy.

- 898 • $\chi^2_{\Delta E} = \left(\sum_{i=2}^4 \frac{\sum N_{ep}}{N_{ep}} (E_b - E_0)^2 \right) / (0.005)^2$ is another penalty term to constrain
 899 E_b running away from the nominal values E_0 of beam energy.

900 **Minimization**

901 TMinuit is used to minimize the value of χ^2 as calculated above and, thereby,
 902 determine the values of the free parameters used in the correction routine.
 903 The minimization was done in such a way that the parameters were deter-
 904 mined step by step - first deciding the first six parameters (keeping others
 905 fixed to initial values), then next two, then next two, then next four, then
 906 next 2 and finally the last one respectively.

907 **Tracking Correction Results**

908 With the method of χ^2 -minimization described above, the following set of
 909 values were determined for the 17 parameters from par[0] through par[16]
 910 respectively:
 911 -0.00165789, -0.00131314, -0.00643021, -0.00721441, -0.00775272, 0.00483673,
 912 0.063387, -0.0615822, 0.00133127, 0.000839944, 0.0210091, -0.0363265, 0.00335536,
 913 0.00104193, 2.51519, -0.0313527, -1.29325

914 As a result of the corrections with these newly determined parameter
 915 values, various quantities before and after the corrections looked as shown in
 916 the following figure:

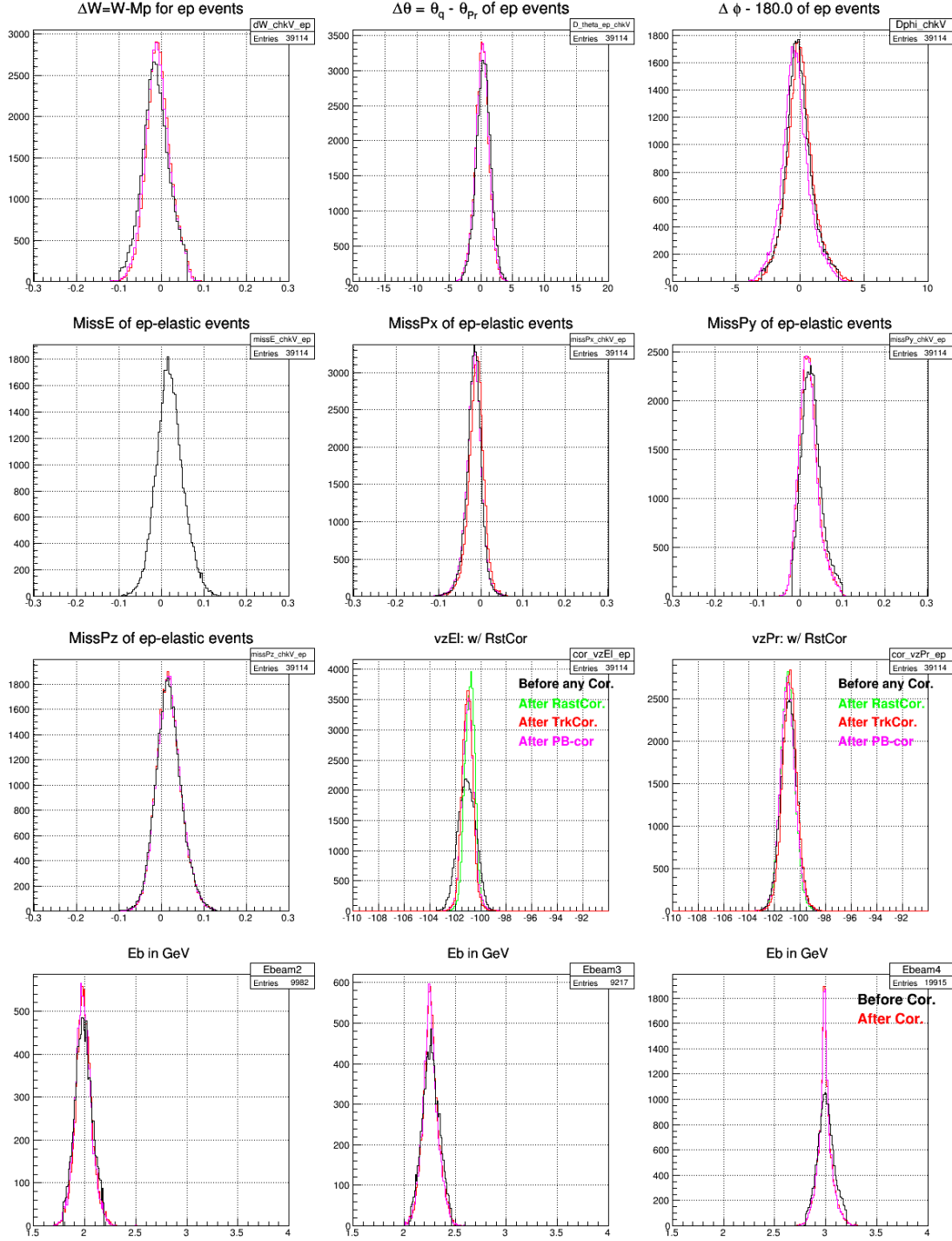


Figure 3.25: Comparing various quantities before and after the tracking corrections which affects only the angles (and ~~not~~ the magnitude 'p') of the momentum.

917 **3.5.3 Momentum Correction**

918 Different DC related factors contribute to the biggest part of the system-
 919 atic deviations of particle momenta as reconstructed by RECSIS. The drift
 920 chambers could be misaligned relative to their nominal positions or the sur-
 921vey results that is used by RECSIS could be inaccurate or out-of-date. The
 922 effects of physical deformations (due to thermal and stress distortions) of
 923 the chamber including wire-sag, incorrect wire positions may not have been
 924 incorporated properly. The torus field map used by the reconstruction soft-
 925 ware may not have been accurate and complete enough [31]. Effects on angles
 926 θ and ϕ due to these contributions are already factored in the tracking cor-
 927 rection described earlier. However, a separate method is developed to correct
 928 for the effect on the magnitude p of the momentum. This p -correction meth-
 929 ods picks up and builds on some of the ideas outlined in the CLAS-NOTE
 930 2003-005 [31].

931 **Procedure to determine the first 11 parameters**

932 The procedure involved dividing the covered kinematic space into a number
 933 of bins, finding in them the magnitude of shifts of the inclusive elastic peaks
 934 w.r.t. the expected position and use that to fit to a function to get an
 935 analytical expression for the correction. The following angular bins were
 936 used:

- 937 • Six θ_{dc1} bins: (0,8),(8,10),(10,12),(12,15),(15,20),(20,30) degrees
- 938 • Five ϕ_{dc1} bins: (-10,-6),(-6,-2), (-2,2), (2,6), (6,10) degrees

939 where the angles used are the ones measured at the first drift chamber and
 940 ϕ_{dc1} is measured w.r.t the sector mid-plane (thus the maximum range allowed
 941 is (-30.0,30.0)).

$$E'_{elastic} = \frac{E_{beam}}{1 + \frac{2E_{beam}}{M_p} \sin^2(\theta_e/2)} \quad (3.4)$$

942 In each of these kinematic bins, the quantity $\Delta E = E'_{elastic} - p$ (see Eq.
 943 3.4) is histogrammed for both NH₃ and ¹²C data separately. Next, the carbon
 944 histogram is cross-normalized with the ammonia histogram (by comparing
 945 the two in the region left to the quasi-elastic peak) and subtracted from the

946 latter one to remove the nuclear background. The difference gives histograms
 947 for the elastic events (as shown by the dashed green histogram in Fig. 3.26).
 948 A Gaussian fit to the extracted elastic histogram gives the position and width
 949 of the distribution. The offset or shift of average position of the peak with
 950 respect to the expected $\Delta E = 0$ gives us the needed correction on energy
 951 $E \approx p$ for the electron. This process is repeated for all of the bins listed
 952 above and the corresponding ΔE offsets or the corrections are determined
 953 for each of them. Additionally, ΔE distributions using ^{15}N nuclear mass
 954 in calculating $E'_{elastic}$ are also made and off-sets in the corresponding elastic
 955 peaks are also recorded whenever possible (particularly from the lower θ bins
 956 from low beam energy data where the nuclear-elastic and quasi-elastic peaks
 957 are well separated). Finally, these values of corrections for different average
 958 values of θ_{dc1} and ϕ_{dc1} are fit to Eq. 3.5 (which is based on similar work done
 959 for EG1b analysis[22]) and using the method of χ^2 -minimization in order to
 960 determine the values of the 11 fit parameters.

$$\frac{\Delta p}{p} = Pcorr1 + Pcorr2 + PatchCorr \quad (3.5)$$

961 where, $\frac{\Delta p}{p}$ is the ratio of the correction (Δp) to the magnitude (p) of the
 962 momentum and

$$Pcorr1 = \left((E + F\phi) \frac{\cos \theta}{\sin \phi} + (G + H\phi) \sin \theta \right) \frac{p}{qB_{torus}} \quad (3.6)$$

$$Pcorr2 = (J \cos \theta + K \sin \theta) + (M \cos \theta + N \sin \theta)\phi \quad (3.7)$$

$$PatchCorr = 0.02 \left(P + (Q + R \frac{\phi_{deg}}{30^\circ}) (\frac{10^\circ}{\theta_{deg}})^3 \right) \quad (3.8)$$

963 The quantity B_{tor} stands for $\int B_\perp dl$ along the track length multiplied by
 964 the speed of light in the units of m/ns ($c = 0.29979$ m/ns) and is given by

$$B_{tor} = 0.76 \frac{I_{tor} \sin^2(4\theta)}{3375\theta/rad} \quad \text{for } \theta < \frac{\pi}{8} \quad (3.9)$$

$$B_{tor} = 0.76 \frac{I_{tor}}{3375\theta/rad} \quad \text{for } \theta > \frac{\pi}{8} \quad (3.10)$$

965 In all these equations, sector number, θ , ϕ , θ_{deg} , and ϕ_{deg} come from the
 966 angle information measured at DC1. The direction cosine variables tl1_cx,
 967 tl1_cy, tl1_cz (from pass1 ntuple) are used to derive these quantities. C++
 968 standard functions `acos()` and `atan2()` are used to evaluate θ , ϕ (w.r.t the
 969 sector mid plane).

970 These total of eleven unknown parameters were determined by fitting
 971 above mentioned momentum offsets (in combination with ionization energy
 972 loss correction for electrons (see Sec.3.5.4 below)) to the correction function
 973 given by the Eq. 3.5.

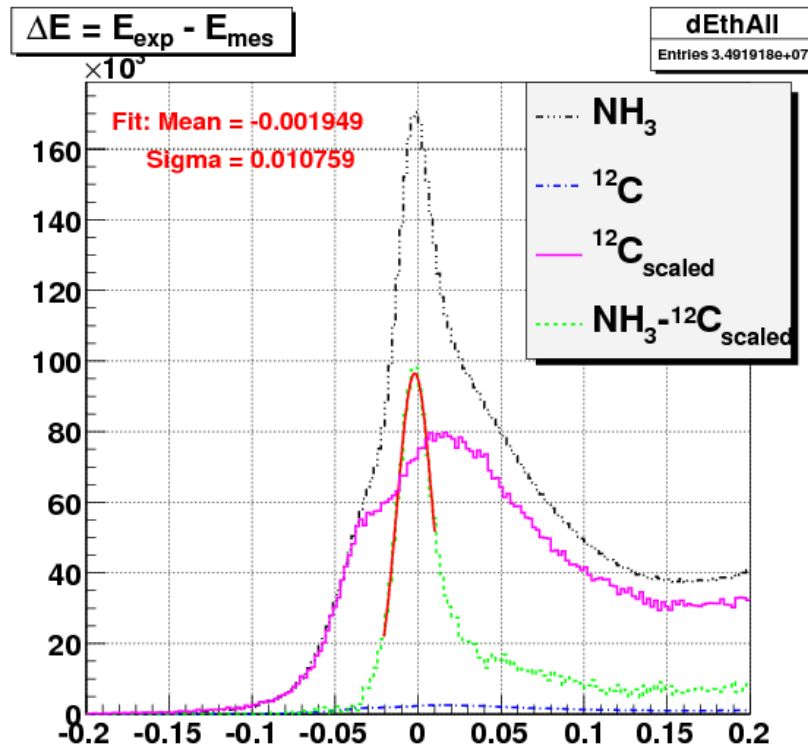


Figure 3.26: Plots showing background removal from the ΔE counts from NH_3 (shown by “ NH_3 ” line) data (by subtracting cross-normalized counts from ^{12}C data (shown by “ $^{12}\text{C}_{\text{scaled}}$ ” line)) to separate the elastic peak (shown by “ $\text{NH}_3 - ^{12}\text{C}_{\text{scaled}}$ ” line) in one of the kinematic bins, thereby getting the momentum offset for that bin. The ^{12}C data is used to account for the nuclear elastic background from ^{15}N nucleii in the ammonia target. It would have been best to have data from ^{15}N target itself but due to technical difficulties that was not possible and, therefore, ^{12}C target was chosen as the closest possible approximation of ^{15}N target.

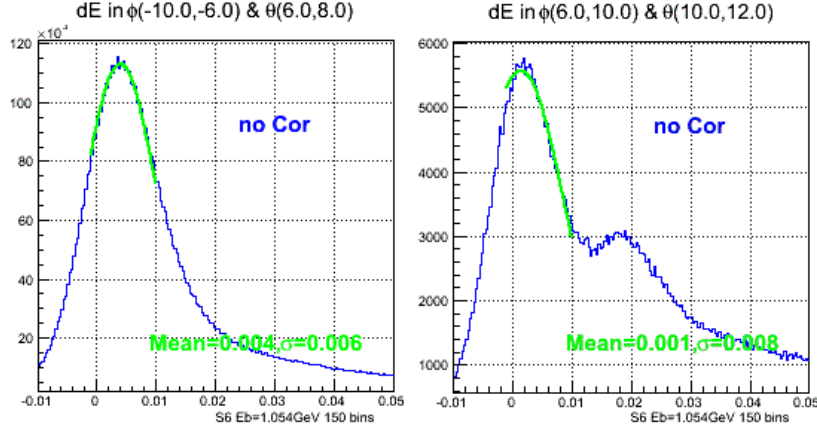


Figure 3.27: Nuclear elastic peaks from ^{15}N target and the Gaussian fits in two of many kinematic bins as seen in $\Delta E = E'_{\text{elastic}} - p$ distributions from NH₃ data before the momentum corrections. In this case E'_{elastic} is evaluated using known mass of ^{15}N in Eq. 3.4. In the second plot, the proton elastic peak is also visible. Ideally, after all the corrections, the nuclear elastic peak is expected to be centered at zero. But, as is obvious from these figures, these peaks show offsets. These offsets (given by the mean values of the Gaussian fits) are collected from those bins in which the nuclear elastic peaks are very well separated (particularly the first few angular bins) and used in the χ^2 -minimization along with all the offsets of elastic peaks (see Fig. 3.26)

974 3.5.4 Outgoing Ionization Loss Correction

975 In addition to the corrections described above, the energy (E) of each of the
 976 particles is corrected for the outgoing ionization loss by adding an estimation
 977 of ionization loss as follows: $E_{\text{cor}} = E + \Delta E$ with $\Delta E = \frac{dE}{dX}\tau$ where the factor
 978 τ is the total effective mass thickness traversed by the particle and

$$dE/dX \approx 2.8 \text{ MeV}/(\text{g cm}^{-2}) \quad \text{for electrons} \quad (3.11a)$$

979 and, for hadrons [32]

$$dE/dX \approx 0.307 \times \frac{0.5}{\beta^2} \left(\ln \left(2.0 \times 511.0 \frac{\beta^2 \gamma^2}{0.090} \right) - \beta^2 \right) \text{ MeV} \quad (3.11b)$$

980 which is an approximation of the Bethe-Block formula [32]:

$$-\frac{1}{\rho} \frac{dE}{dx} = 4\pi N_a r_e^2 m_e c^2 \frac{Z}{A} \frac{1}{\beta^2} \left(\ln \left(\frac{2m_e c^2 \gamma^2 \beta^2}{I} \right) - \beta^2 \right) \quad (3.12)$$

981 The total effective mass thickness τ (in cm) is calculated as follows:

982 • $\tau = \tau_{||}/\cos \theta$ if $\theta <= \pi/4$

983 • $\tau = \tau_{||}/\cos(\pi/4)$ if $\theta > \pi/4$

984 where $\tau_{||}$ is calculated as:

985 • $\tau_{||} = \Delta z \times 0.6 + 0.4$ if $\Delta z > 0.0$ and $\Delta z < 1.0$

986 • $\tau_{||} = 0.6 + 0.4$ if $\Delta z \geq 1.0$

987 • $\tau_{||} = 0.4$ if $\Delta z \leq 0.0$

988 with $\Delta z = z_{target_center} - z_{ave} + L_{target}/2 = (-101.0 \text{ cm} - z_{ave} + 0.5) \text{ cm}$ being
989 the physical distance (along the target length) traveled by the particle
990 through the polarized target material (e.g. the EG4 ND₃ target has length
991 1.0 cm and is positioned at $z = -101.0$ cm). The factor 0.6 is the effective
992 mass thickness of ND₃ (density of ND₃ ($\sim 1 \text{ g/cm}^3$) multiplied by the pack-
993 ing fraction which is roughly 0.6 [33], whereas 0.4 is the sum of the mass
994 thicknesses of He (~ 0.3) and that of window foils (~ 0.1) [22].

995 Using the ionization loss corrected energy and the rest mass of the parti-
996 cle, momentum is recalculated as $p_{cor} = \sqrt{E_{cor}^2 - m^2}$ (where m is the mass
997 of the particle). Finally, this new p is used along with the previously cor-
998 rected angles to evaluate the three cartesian components p_x , p_y and p_z of the
999 momentum as follows:

$$\begin{aligned} p_x &= p \sin \theta \cos \phi \\ p_y &= p \sin \theta \sin \phi \\ p_z &= p \cos \theta \end{aligned} \tag{3.13}$$

1000

1001 3.6 Cerenkov Counter (CC) Efficiency

1002 In the EG4 experiment, the Cherenkov Counter (CC) signal plays a major
1003 part in forming the event trigger for the data-acquisition system (DAQ). As
1004 stated earlier (see 2.1), for the purpose of achieving low Q^2 measurements
1005 with high detector efficiency⁵, a new dedicated CC was designed and placed

⁵High detection efficiency is crucial for achieving smaller systematic uncertainties in the extracted physics quantities.

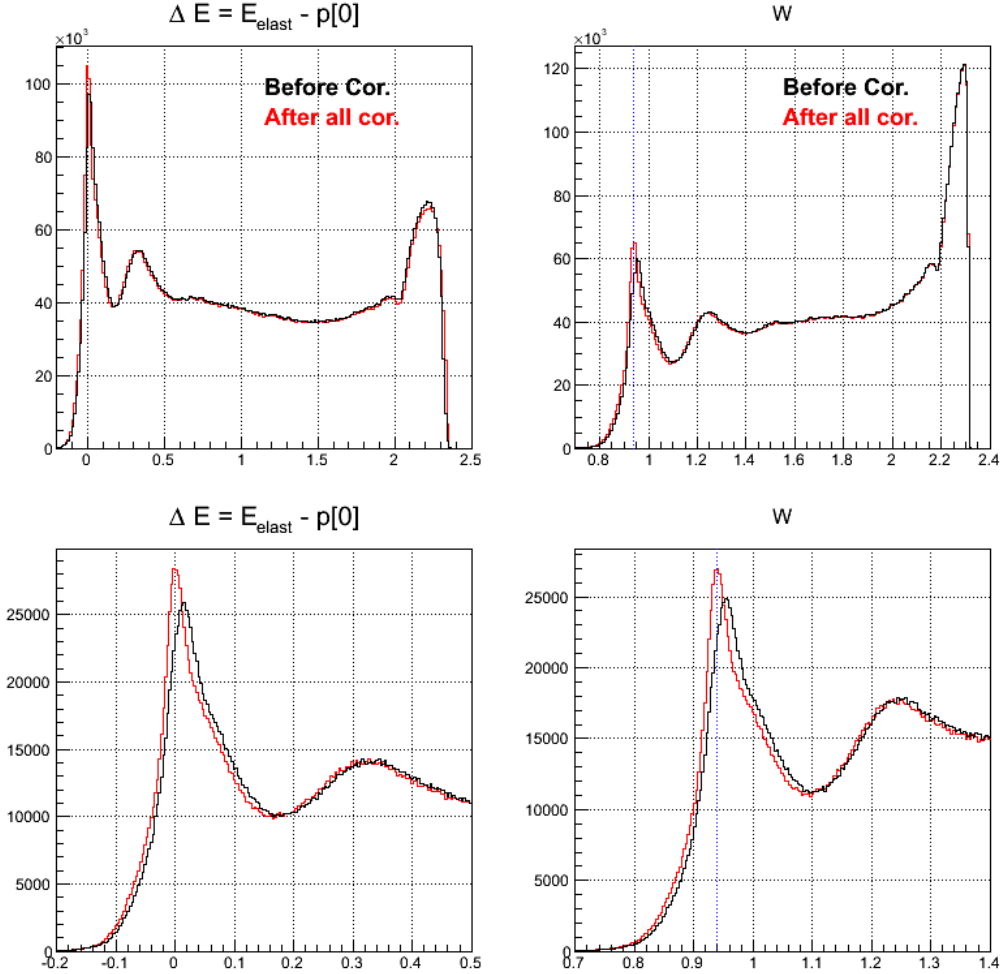


Figure 3.28: Effects of kinematic corrections on inclusive events from 3 GeV NH₃ data. Here, distributions of ΔE and W are shown in two different ranges. The upper ones show the full range distributions, whereas the lower two show the distributions near the quasi-elastic peak. The distributions before the corrections are shown by **black continuous** lines and the ones after the corrections are shown by the **red** lines. Here, E_{elast} is the calculated or expected energy of the scattered electron assuming it was scattered off elastically, whereas, $p[0]$ is the momentum as measured by CLAS. From these plots it is evident that the momentum correction works as expected because the peak of ΔE is narrower and better centered at zero after the correction.

1006 in the sixth sector. Even though the new CC was designed to have a very
1007 high and uniform detection efficiency, some variation occurs over the covered
1008 kinematic range and therefore the knowledge of the detector efficiency as a
1009 function of the kinematics is required by our method of absolute cross-section
1010 difference. Therefore, a study was done to determine the CC efficiency as
1011 follows.

1012 **3.6.1 Procedure**

1013 The efficiency for some specific kinematic bin depends on the average num-
1014 ber of photoelectrons produced by electrons in that bin which, in turn, is
1015 determined by the hit location on the Cerenkov PMT-projected plane as
1016 well as the angle with which the electron hits (or intersects) the plane. In
1017 the following, we describe how we determined the efficiency as a function of
1018 kinematic variables.

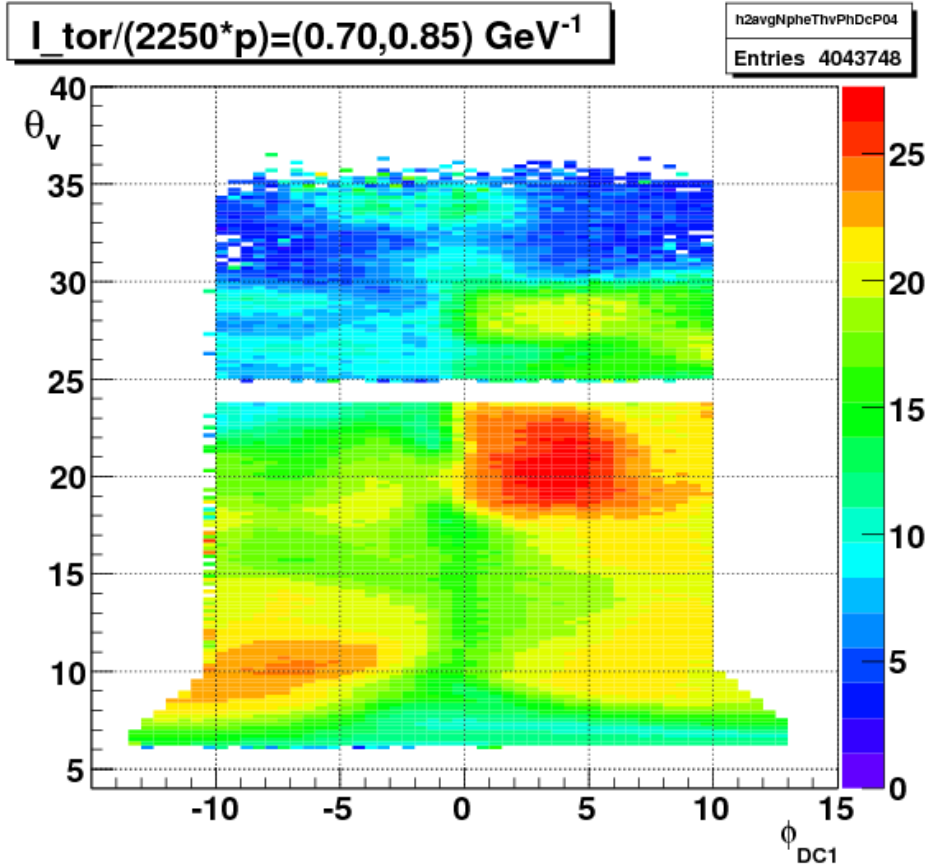


Figure 3.29: Average photoelectron number (color-coded) produced in the 6th sector CC as a function of θ_{vtx} and ϕ_{DC1} in the second bin of the variable $ip = (I_{tor}/2250)/p$ (from the 2.3 GeV NH₃ data).

- 1019 1. First, we define a torus-current normalized inverse-momentum variable
- 1020 $ip = (I_{tor}/2250)/p$ (see above), and divide the whole kinematic space
- 1021 into 12 bins in “ip” as follows: (0.3, 0.4, 0.5, 0.6, 0.7, 0.85, 1.0, 1.25,
- 1022 1.5, 1.75, 2.0, 2.25, 2.53). (For example, a 0.5 GeV electron during a
- 1023 2 GeV run, which used 2250 A for torus current, would have $ip = 2.0$
- 1024 GeV^{-1})
- 1025 2. Next, for each bin in “ip”, a 2D map of the average number of photoelec-
- 1026 trons is produced in a kinematic space defined by θ_{vtx} (scattering angle
- 1027 measured at the event vertex) and ϕ_{DC1} (azimuthal angle as measured

at DC1). For this step, some data from NH₃ production runs⁶ are used with the standard electron selection cuts. One of these average-nphe maps is shown in the Fig. 3.29.

- 1028
- 1029
- 1030
- 1031 3. Next, using the “EC-only-trigger” data runs, good electron candidates
1032 are selected using the same cuts as before but without any CC-related
1033 cuts. For each of the selected electrons, the expected number of photo-
1034 electrons in the CC is determined in a look-up from the above average
1035 N_{ph} -maps based on its momentum and angles. This expected N_{ph} is
1036 then histogrammed in two ways - one histogram for those electrons
1037 which either didn’t trigger CC or didn’t pass all of the CC related
1038 cuts and another histogram for all electrons. The ratio of these two
1039 histograms (shown in the top-right and top-left panels of Fig. 3.30 re-
1040 spectively) gives us the inefficiency of the CC-detector as a function of
1041 N_{ph} (as shown by the bottom two panels of the same figure). (Errors
1042 in the inefficiencies have not been drawn (for the purpose of cleaning)
1043 in the figures but they were calculated using the fact that the error in
1044 a ratio N2/N1 is $\sqrt{N2(1 - N2/N1)/N1}$).
- 1045 4. The ideally expected CC intrinsic inefficiency is given by the Poisson
1046 distribution, since we require more than 2 photoelectrons, the theoreti-
1047 cal prediction for the inefficiency is actually $(1 + N_{ph} + 1/2 N_{ph}^2) * \exp(-N_{ph})$. However,
1048 we found empirically that if we calculate N_{ph} only with
1049 electrons that exceed the threshold of 2.5, then we find that the
1050 functional form is pretty close to the form $y = p_0 + p_1 \cdot \exp(-p_2 x)$, where
1051 x represents $\langle N_{ph} \rangle$, and y represents the inefficiency. This form was
1052 used to fit with the above measured inefficiency and the result of the
1053 fit is shown in Fig. 3.30. We find that the inefficiency agrees very well
1054 with the expectation at low nphe, but remains at a very small constant
1055 value of around 0.01 (we call it the “constant background”) at higher
1056 nphe.

⁶This method relies on the use of two different sets of data. One is the regular NH₃ target data and another is the “EC-only” data runs which were collected without using CC in the trigger. Since the latter type of data were collected with NH₃ as target, to be consistent, NH₃ production data was chosen rather than the ND₃ ones to make the N_{ph} -maps.

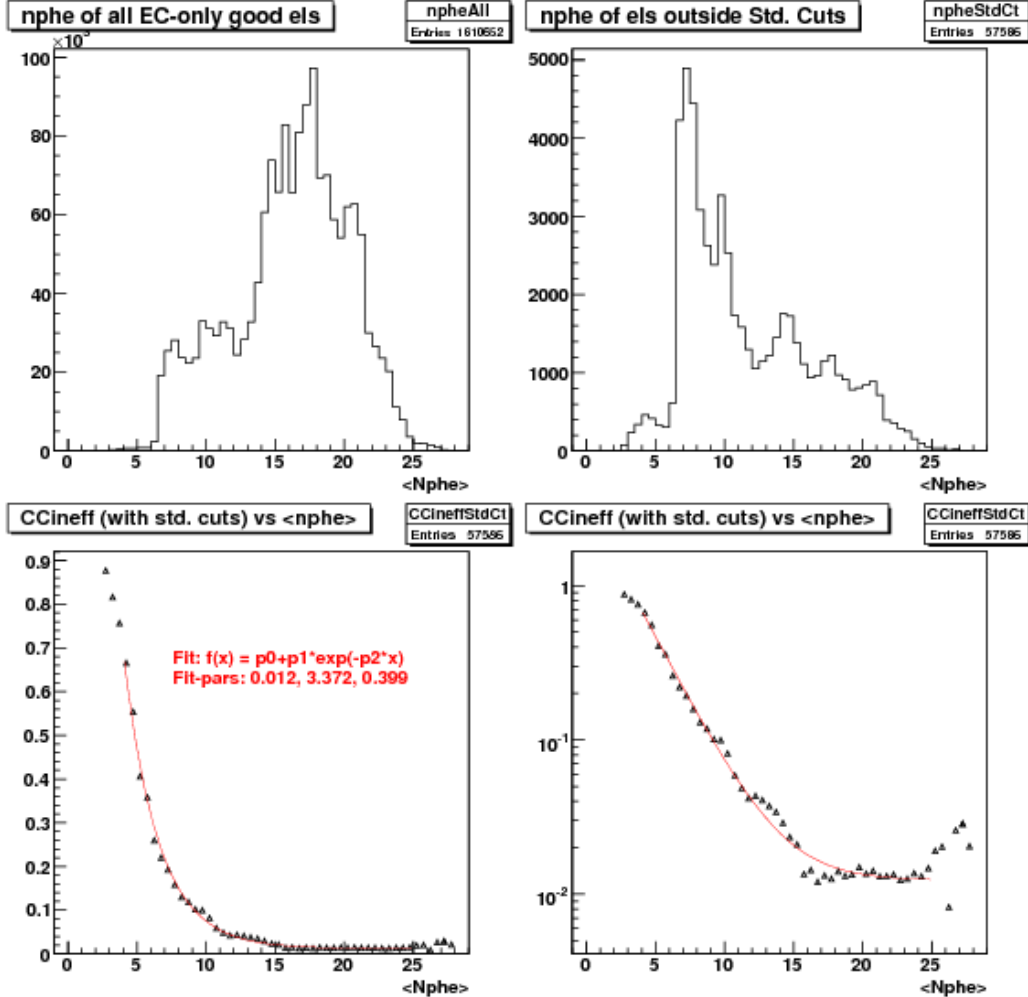


Figure 3.30: EC detected good electrons (for all momenta) as a function of $\langle N_{ph} \rangle$ (top left). Similar distribution (top right) for those good electrons that were detected by the EC but were rejected by the standard set of event selection cuts which includes CC-dependent cuts. By dividing the latter with the former, one gets the calculated CC inefficiency. The bottom two plots show the inefficiency distribution and a fit (red continuous line) in both linear (in third panel) and logarithmic (fourth panel) scales. Looking at the first plot, it can be seen that most electrons are above $N_{ph} = 15$ where the inefficiency is at most 1-2 %.

- 1057 5. Finally we use the inefficiency fit just developed to evaluate the corre-
 1058 sponding efficiencies and transform the 2D map of N_{ph} into the corre-

1059 sponding efficiency maps (see Fig. 3.31 for such a map in one momen-
 1060 tum bin.). These maps are later used to apply the efficiency correction
 1061 on an event by event basis in the simulation.

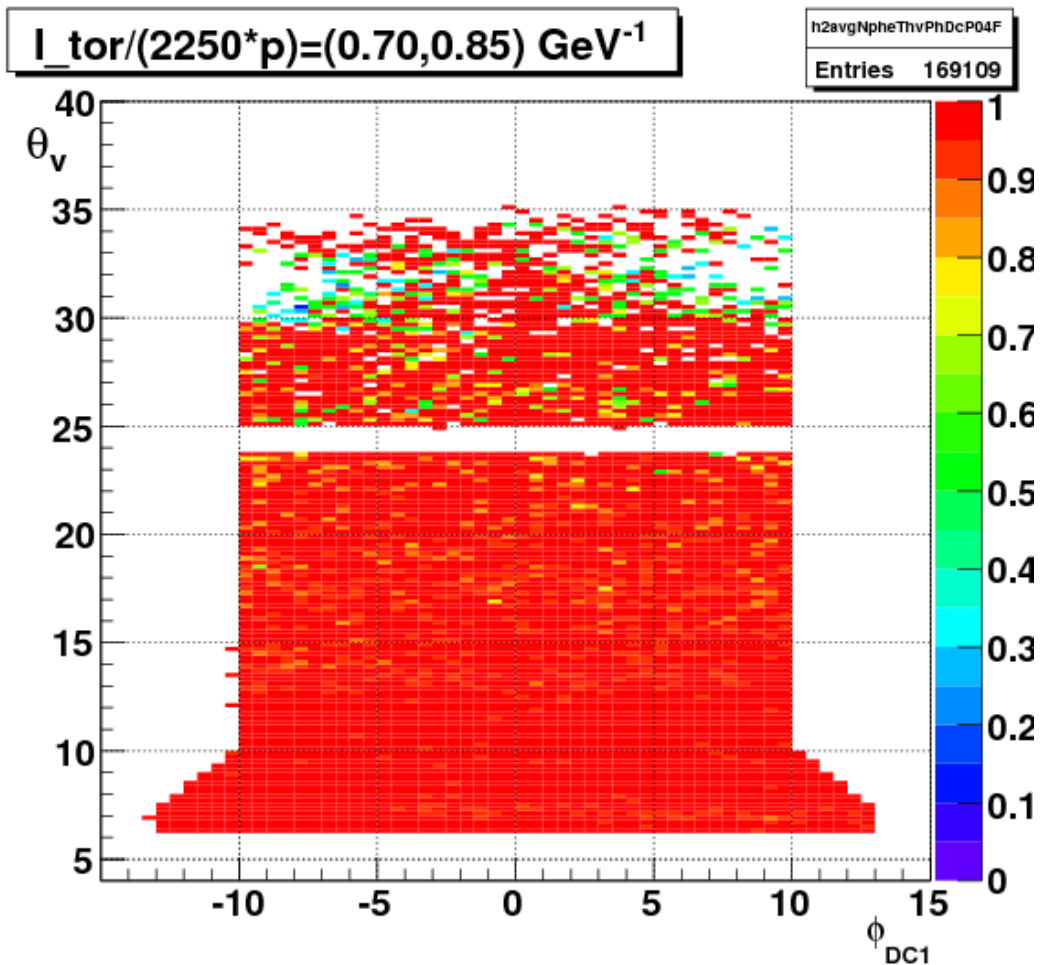


Figure 3.31: CC-efficiency in a momentum bin .

1062 From this study, we see that the CC is very efficient in most of the
 1063 kinematic region (see Fig. 3.31). Once, the CC-(in)efficiency was estimated,
 1064 we use the calculated CC efficiency to multiply our simulation (i.e., for each
 1065 simulated event, we look up the CC efficiency and weigh the event with it).

3.7 Pion Contamination Corrections

One of the two major sources of backgrounds in the measured EG4 electron rates comes from misidentified negatively charged pions (π^-) that produce similar set of signals as electrons in various detector components and thus pass the electron ID cuts. In the EG4 experiment, signals from the electromagnetic calorimeter (EC) and Cherenkov counter (CC) are used to identify electrons from pions, but even with stringent conditions on these signals, some of the pions get misidentified as electrons. To avoid limiting statistics too much in order to minimize the final statistical error in a given kinematic bin, a trade-off in purity versus efficiency (statistics) is made by quantifying the amount of this kind of contamination.

3.7.1 Method

First, the whole kinematic space covered by EG4 is divided into 90 two-dimensional bins - 9 in p and 10 in θ ⁷.

For each kinematic bin, a histogram of the number of photo-electrons (variable ' N_{phe} ' in the data ntuple) produced by the electron candidates (selected using the standard particle selection conditions (cuts) except that no cut on ' N_{phe} ' is included is made (see Fig. ??). Likewise, using a very stringent set of cuts, a similar histogram is made for the cleanest possible sample of pion candidates in the same kinematic bin.

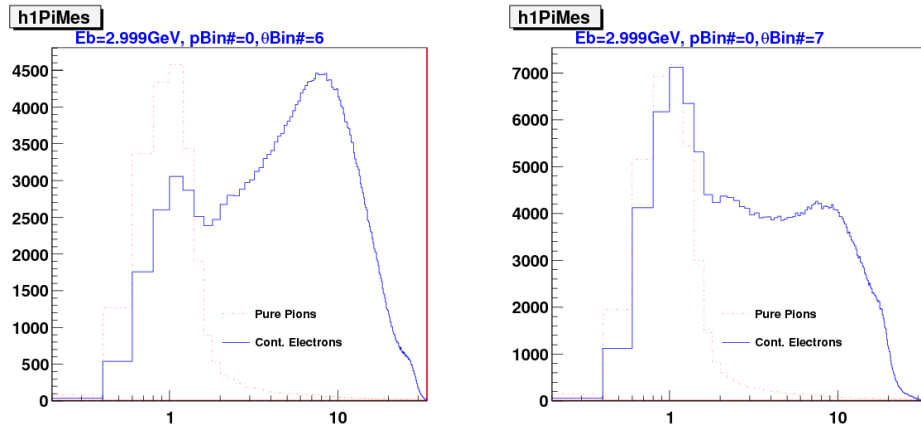
- **Estimating the contamination in each bin:** A 7th order polynomial is fit to the N_{phe} histogram for electrons in the N_{phe} range extending from $N_{phe} = 1.8$ to $N_{phe}=10$. The fit is then extrapolated down to $N_{phe} = 0$ (see Fig. ??). Subtracting the extrapolated fit from the impure electron distribution results in the extraction of the contaminating pion peak⁸. Rescaling the pure pion sample to the extracted

⁷For 2 GeV or higher beam energy data sets, the p -bin boundaries are chosen as (0.30, 0.60, 0.90, 1.20, 1.50, 1.80, 2.20, 2.60, 3.00) and (0.30, 0.45, 0.60, 0.75, 0.9, 1.1, 1.4) for others. And, for θ , the boundaries are (5.0, 6.0, 7.0, 8.0, 9.0, 10.0, 12.0, 15.0, 19.0, 25, 49). The choice of the binning was rather arbitrary. Nevertheless higher statistics region was divided into relatively finer bins (event population peaks around $\theta= 10$ degrees).

⁸Beyond $N_{phe} = 1.8$, the electron sample is nearly pure except for a tiny fraction due to the pion tail, so any function that fits that section of the N_{phe} -distribution is supposed to represent the pure electron distribution. In order to simplify the situation, we chose to fit only from 1.8 to 7.0 rather than covering the full range beyond 7.0.

peak gives us the distribution of the actual pion contamination over
 the complete range of N_{phe} . Finally, the counts corresponding to this
 rescaled pure sample in the region above the standard cut $N_{phe} > 2.5$
 is calculated. Then the ratio of this count to the impure electron count
 in the same standard N_{phe} range gives the measured contamination for
 the bin.

- The contaminations thus evaluated for different momentum bins belonging to a particular θ -bin are then plotted against the corresponding momenta. Then, this is fit to an exponential function.
- The parameters par1 and par2 of the exponential fit performed in different theta bins are next graphed together to see the presumed linear dependence.
- Finally, a global fit is performed on all the contaminations in different θ - and p- bins (not on the fit parameters). The fit parameters from the earlier two fits only give us a hint to the type of the dependence, thus allowing us decide the form of the fit function.



(a) For the first in momentum and seventh in θ bin.
 (b) For the first in momentum and eighth in θ bin.

Figure 3.32: Number of photo-electrons produced in CC by clean pion and contaminated electron samples (3.0 GeV data)

1108 From the study, it is found that the typically pion contamination is less
1109 than 1 %.

1110 **3.8 e^+e^- -Pair Symmetric Contamination Cor-** 1111 **rections**

1112 The next major source of background is the secondary electrons from various
1113 e^+e^- pair production processes. When an electron originating from such a
1114 pair passes through the detector, the detector has no way to distinguish it
1115 from the electrons that actually scattered off the target. Therefore, the detec-
1116 tor simply accepts it as a true scattered electron candidate, thus producing
1117 a contamination that has to be estimated and corrected for. The first such
1118 source is the wide-angle e^+e^- pair production from bremsstrahlung photons
1119 generated in the target. The other major source is hadron decay such as
1120 the Dalitz decay ($\pi^0 \rightarrow e^+e^-\gamma$), $\pi^0 \rightarrow \gamma\gamma$ and then conversion of these photons
1121 into e^+e^- pairs. Likewise, the pseudoscalar particle η , and the vector mesons
1122 ρ , ω , ϕ also decay to e^+e^- , but they are not major contributors because of
1123 their very small decay probabilities as well as the small population compared
1124 to the π^0 and photons. Of all these sources, the biggest contributor to the
1125 secondary electrons is the $\pi^0 \rightarrow \gamma\gamma$ with γ conversion to e^+e^- [34].

1126 The amount of contamination from this type of process can be estimated
1127 by monitoring the amount of positrons that were recorded under the same
1128 experimental and kinematic conditions. Because of the symmetry in the
1129 amount of electrons and positrons produced from these sources, the positron
1130 to electron ratio gives us the amount of the pair-symmetric contamination.
1131 However, due to the presence of the strong magnetic field inside the detector
1132 and the fact that the positrons have opposite charges, their detector accep-
1133 tance would be different in a given setting. By reversing the magnetic field
1134 while keeping everything else the same, it is possible to estimate the con-
1135 tamination. For some of the beam energies used for the NH₃ data of the
1136 EG4 experiment, some data were collected with identical experimental set-
1137 ting but with the torus field reversed. The data from those runs were used
1138 to estimate the amount of positrons in somewhat the same fashion as pion
1139 contamination. For example, Fig. 3.34 shows one estimate (both data points
1140 and the fit) of the contamination in EG4 compared with those determined
1141 for the EG1b experiment [22].

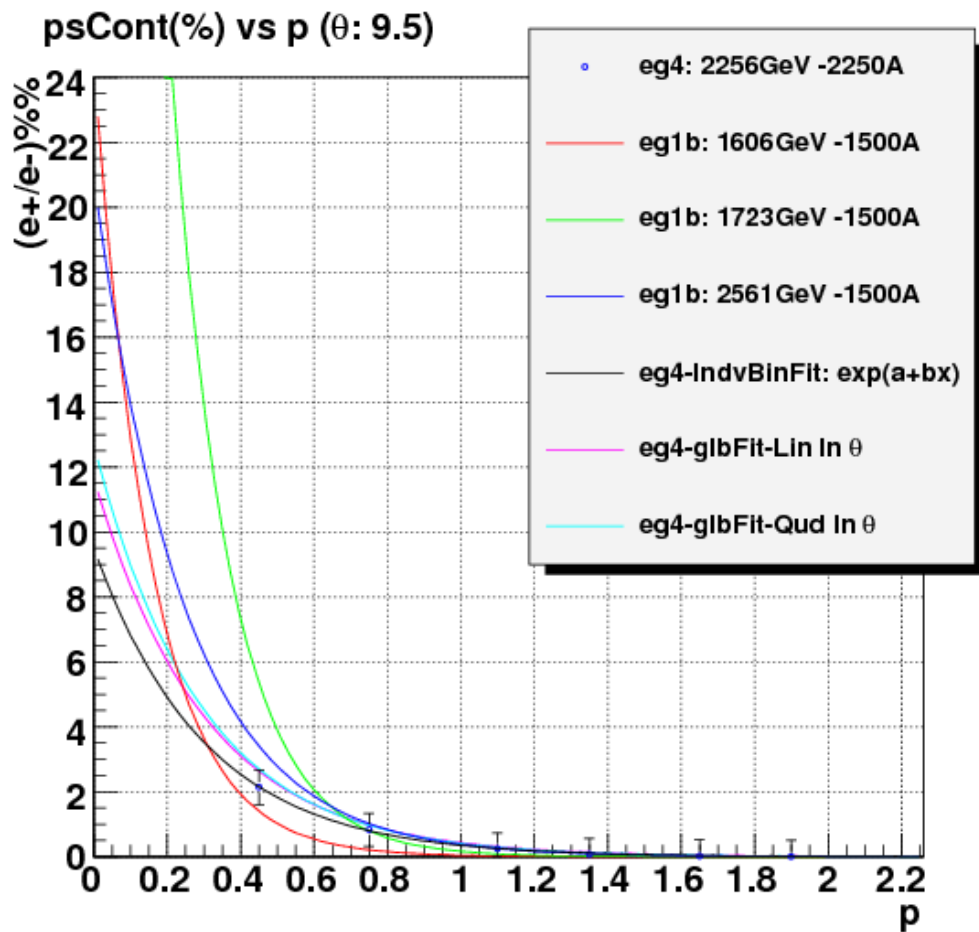


Figure 3.34: Pair-symmetric contamination Fits (%) as a function of electron momentum.

1142 For this analysis, both the pion and e^+e^- pair symmetric contaminations
 1143 are small enough to be ignored. This leads to only a slight increase in the
 1144 systematic error in the final physics results.

1145 **3.9 Study of NH₃ Contamination of EG4 ND₃**
1146 **Target**

1147 In equation (3.1), it is assumed that the ammonia target is 100% pure i.e.
1148 composed of only ¹⁵ND₃ molecules and that the contribution from the
1149 slightly polarized nitrogen is negligible. But, in practice, the standard ND₃
1150 sample is not a 100% pure material. Rather, it contains one or two percent
1151 of ¹⁴ND₃, ¹⁵NH₃ [35], and some traces of other isotopic species of ammonia.
1152 It was reported by the EG1-DVCS experiment at Jlab [36][37] that a higher
1153 than usual amount of NH₃ (about 10%) was observed in the ND₃ target,
1154 indicating that an inadvertent mix-up of NH₃ and ND₃ materials could have
1155 happened during the experimental run. Wondering if the EG4 experiment
1156 had a similar incident, we decided to investigate and estimate the amount of
1157 NH₃ contamination of our ND₃ target by looking at the data from the ND₃
1158 run period of the experiment as described below.

1159 **3.9.1 Procedure**

1160 The method involves using ep elastic (or quasi-elastic in the case of non-
1161 proton target) events and comparing the width in some quantity that reflects
1162 the correlation between the scattered electron (e) and the recoiling proton (p)
1163 due to the kinematic constraints of such events. The most suitable correlation
1164 is the one between the polar angles of the electron and the proton. That is
1165 because of the better angular resolution in CLAS than that for momentum,
1166 and also due to the fact that polar angle (θ) resolution is much better than
1167 that of the azimuthal angle (ϕ) because of the rotational effect (on ϕ) of the
1168 polarized target field as well as the drift chamber resolutions [36].

The θ -correlation can be studied mainly in two ways. The first way is to reconstruct and histogram the beam energy using the measured polar angles and the known target mass and then compare the histogram from the ND₃ target run with that from a pure NH₃ target run. The other equivalent way is to predict the proton polar angles (using the measured electron angles, known target mass and the beam energy) and then histogram the deviation of the measured proton angles from the expected values. We chose to use a slightly modified version of the latter approach in which we histogram the

following quantity⁹:

$$\Delta = p_p \cdot (\sin \theta_q - \sin \theta_p) \quad (3.14)$$

where p_p is the measured proton momentum, θ_p is the measured polar angle of the proton, and θ_q is the expected polar angle of the recoiling proton (which is also the angle of the exchanged virtual photon (q)) given by:

$$\theta_q = \tan^{-1} \left(\frac{M_p}{\tan(\theta/2) \cdot (E_{beam} + M_p)} \right) \quad (3.15)$$

The method exploits the fact that the width of the quantity Δ from data with deuteron target decreases because the Fermi motion of the protons in the deuteron nuclei gives a spread of the order of 50 MeV in transverse momentum, and for longitudinal particle momenta of order of a few GeV, we obtain a polar angle spread about 20 mr, which is much larger than the intrinsic CLAS resolution of about 2 mr.

3.9.2 Event Selection

First, for each data set (corresponding either to NH₃, ND₃ or ¹²C runs), using standard electron and proton identification cuts , events with a well reconstructed scattered electron and a similarly well reconstructed candidate for proton are selected. We accept only events each of which have one electron, one proton and at most one neutral particle candidate (expected to be a neutron coming off from the deuteron target break-up). If the event is of the above type, the following additional cuts are applied to make sure it is elastic or quasi-elastic event:

- $E_X < 0.15$ GeV with $E_X = M_p + E_e - E_{e'} - E_p = M_p + \nu - E_p$
- $P_X < 0.5$ GeV/c with $\vec{P}_X = \vec{0}_p + \vec{P}_e - \vec{P}_{e'} - \vec{P}_{p'} = \vec{P}_e - \vec{P}_{e'} - \vec{P}_{p'}$
- $0.88GeV < M_X < 1.04GeV$
- $\theta_q < 49.0^\circ$
- $||\phi_e - \phi_p| - 180.0^\circ| < 2.0^\circ$

⁹We chose this quantity Δ rather than the simple angle difference ($\theta_q - \theta_p$) because the former is more directly interpretable in terms of transverse missing momentum for the case of quasi-elastic scattering.

1189 where X indicates the missing entity in the $d(e,e'p)X$ channel, which is ex-
1190 pected to be neutron in the case of the quasi-elastic channel, thus E_X is the
1191 missing energy and so on.

1192 If it passes these cuts, the quantity Δ in Eq. 3.14 is calculated for
1193 the event and then histogrammed as shown by the red curves in the top-left
1194 (from ^{12}C runs), top-right (from NH_3 runs), and bottom-right (from ND_3
1195 runs) panels of Fig. 3.35.

1196 After getting the histograms for the quantity Δ for the ep-elastic or
1197 quasi-elastic events from the NH_3 , ND_3 and ^{12}C target data sets, we first
1198 remove the contribution from the non-hydrogen component of NH_3 and ND_3
1199 targets by subtracting the corresponding carbon histogram (properly scaled
1200 to match with the left-shoulders (mainly from the nuclear elastic background
1201 in each of the ammonia data)). Since the carbon data is too low in counts
1202 (hence the raggedness in the histogram), a fit (a 'gaussian' times a 'linear'
1203 function) to the carbon data is obtained, and that fit (shown as the blue
1204 line in the first panel in Fig. 3.35 is used instead of the histogram itself
1205 to remove the background. The blue line in the second (top-right) panel
1206 and the cyan line in the last (bottom-right) panel show the properly scaled
1207 carbon fits which are subtracted from the NH_3 and ND_3 histograms (shown
1208 by red lines) respectively. After the subtraction, we get new histograms
1209 that represent 'pure' elastic or quasi-elastic data from protons and deuterons
1210 (shown by the magenta lines in the third and last panels respectively).

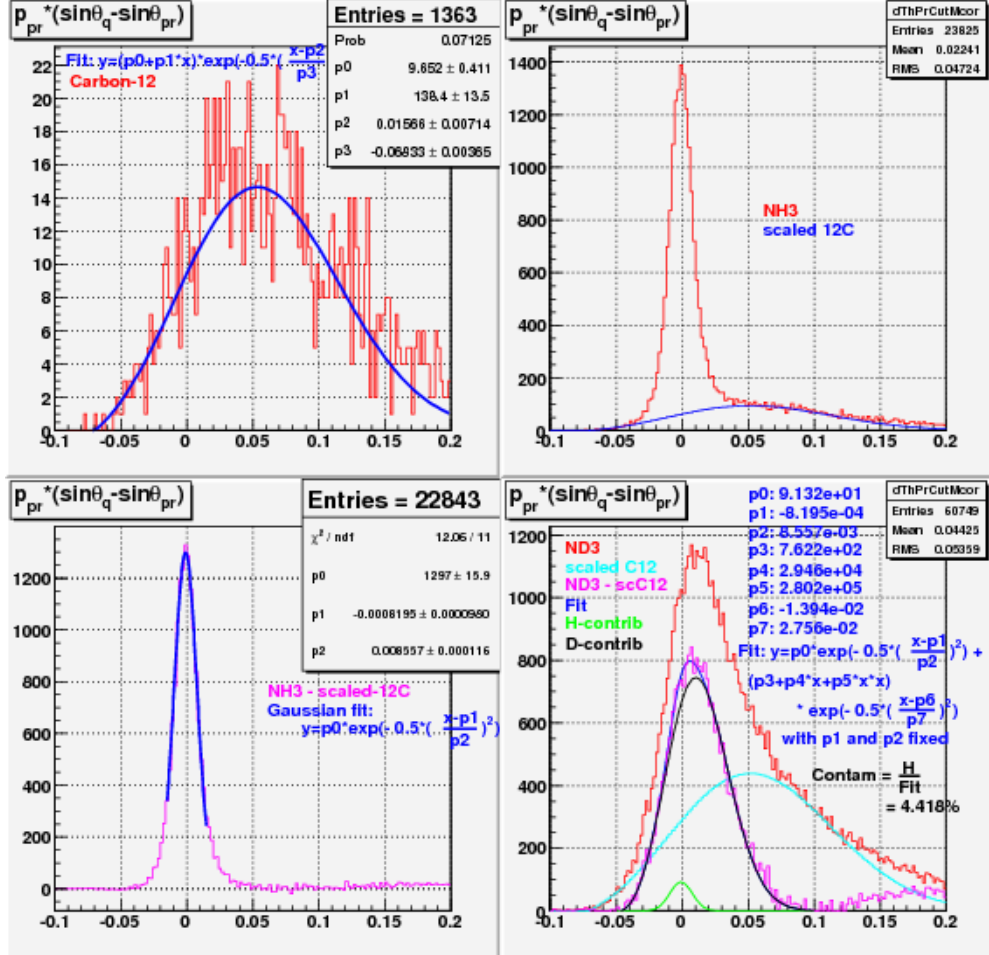


Figure 3.35: Histograms showing the quantity $\Delta = p_p \cdot (\sin \theta_q - \sin \theta_p)$ for elastic or quasi-elastic events from carbon-12 (top-left), NH₃ (top-right) and ND₃ (bottom-right) target runs respectively. The third (bottom-left) panel shows the background removed elastic events from the NH₃ data. In the fourth panel, various Δ are shown - red is the raw ND₃, light green is the scaled-¹²C for the nuclear background, brown is for the difference between the two.

3.9.3 Extracting the Contamination

After we have the 'pure' elastic or quasi-elastic data from NH₃ and ND₃ runs, we get the mean and the spread (standard deviation σ) of the proton elastic peak by fitting the NH₃ data to a Gaussian function $f_p(x)$ (the blue line in

1215 the third panel with parameters p0=height, p1=mean and p2= σ). After
 1216 we have the fit for the proton elastic peak, we fit the background subtracted
 1217 deuteron data to a function $f(x)$ that is a linear combination of the pure
 1218 proton fit and a pure deuteron fit (the latter with the form of **a quadratic**
 1219 **function \times a Gaussian**¹⁰) as follows:

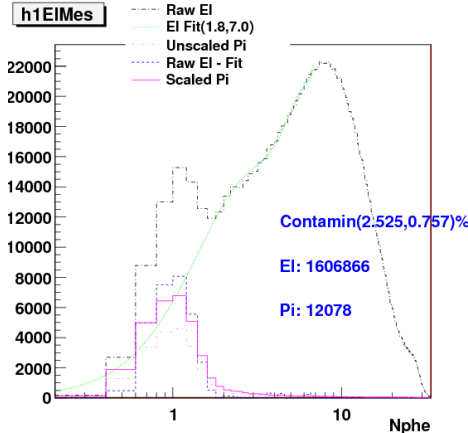
$$f(x) = p_0 \cdot f_p(x) + (p_1 + p_2 \cdot x + p_3 \cdot x^2) \cdot e^{-0.5 \cdot \left(\frac{x-p_4}{p_5}\right)^2} \quad (3.16)$$

1220 where p_i ($i = 0, 2, \dots, 5$) are the free parameters which are determined by
 1221 fitting of $f(x)$ to the deuteron data. The first term $p_0 \cdot f_p(x)$ in $f(x)$ represents
 1222 the contribution from the contaminant (i.e., protons in ND_3) and the rest
 1223 of the term in $f(x)$ represents the contribution from the deuterons in ND_3 .
 1224 The total fit function $f(x)$, the proton contribution and the deuteron part are
 1225 shown by the blue, green and black lines in the fourth panel. The ratio of
 1226 the area under the green line to that under the blue line gives us the relative
 1227 amount of the NH_3 contamination in the ND_3 target.

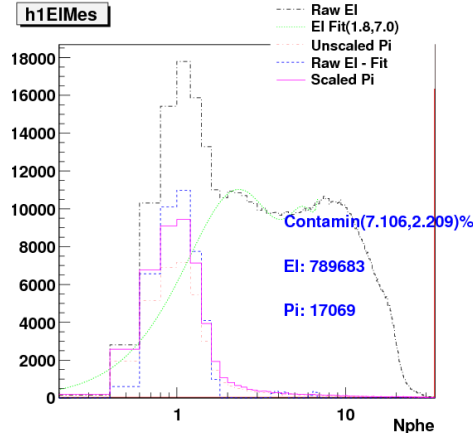
1228 3.9.4 Results and Conclusion

1229 From the calculation as described above, the estimate for the ND_3 contam-
 1230 ination came out to be 4.4% It was not possible to do a similar analysis on
 1231 the 1.3 GeV ND_3 data, because the CLAS acceptance constraints did not al-
 1232 low for the coincident detection of e and p from the exclusive (quasi-)elastic
 1233 events. The basic conclusion is that at 2 GeV, we cannot get a 'pure' Gaus-
 1234 sian spectrum for deuteron, and therefore, there is no way to unambiguously
 1235 separate deuteron from proton in ND_3 . The fact that the fit looks reason-
 1236 ably well (with contamination coming out to be only a few percent) and that
 1237 we clearly do not see a narrow peak on top of a wider one (unlike in EG1-
 1238 DVCS) should be sufficient to ascertain that EG4 did NOT have the same
 1239 contamination problem as EG1-DVCS (which still has not been explained
 1240 yet) [26]. To accommodate the fact that the contamination measurement is
 1241 not reliably unambiguous, we will assume a rather generous systematic error
 1242 due to the contamination.

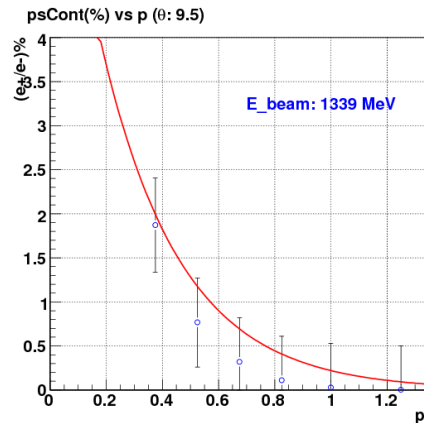
¹⁰A pure Gaussian and other forms for the deuteron spectrum were tried but the overall fit was not as good.



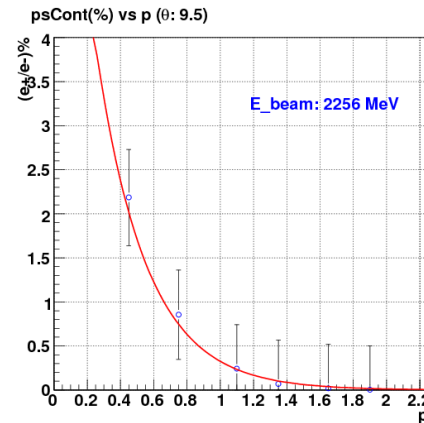
(a) For the first bin in momentum and seventh bin in θ .



(b) For the first bin in momentum and eighth bin in θ .



(c) Fits in the $\theta(9.0, 10.0)$ bin for 1.339 GeV data.



(d) Fits in the $\theta(9.0, 10.0)$ bin for 2.0 GeV data.

Figure 3.33: The top row plots show the calculation of pion contamination of electrons for the given kinematic bins of 3.0 GeV data. The dotted black line indicated by the label “Raw El” in the legends of each of the two plots are the contaminated electrons. Likewise, the line labeled “El Fit” is a polynomial fit to the electron distribution (in this case fitted from Nphe=1.8 to 7.0, but extrapolated down to Nphe=0). The line labeled “Unscaled Pi” is the pure pion distribution obtained with stringent set of cuts. “Raw El - Fit” is the difference between the contaminated electron sample and the polynomial fit and finally “Scaled Pi” is the pure pion-sample but after its scaled to match with the “Raw El - Fit” at the pion peak position (around 1 Nphe). The bottom row plots show the fits of the contaminations as a functions of momentum (p) in a given θ bin.

₁₂₄₃ **Chapter 4**

₁₂₄₄ **Monte Carlo Simulations and**
₁₂₄₅ **Extraction of g_1 and $A_1 F_1$**

₁₂₄₆ **4.1 Simulation and Approach to Analysis**

The EG4 data consist of a table numbers of electrons reconstructed within various (W, Q^2) bins that are scattered off polarized hydrogen (NH_3) or deuteron (ND_3), divided by the (life-time gated) integrated charge, for two different combinations of target polarization and beam helicity:

$$n^\pm = N^\pm / FC^\pm, \quad (4.1)$$

where “+” refers to beam helicity and target polarization anti-parallel, while “−” refers to the parallel case. The difference between these two normalized counts is given by

$$\Delta n(W, Q^2) = n^+(W, Q^2) - n^-(W, Q^2) = \mathcal{L}_r \cdot P_b P_t \cdot \Delta\sigma(W, Q^2) \cdot AccEff(W, Q^2) + Bg \quad (4.2)$$

₁₂₄₇ where the “relative luminosity” \mathcal{L}_r is a constant factor containing the density of polarized target nuclei per unit area and the conversion factor from ₁₂₄₈ Faraday cup counts to integrated number of electrons incident on the target; ₁₂₄₉ P_b and P_t are the beam and target polarization, ₁₂₅₀ Acc and Eff are the ₁₂₅₁ geometric acceptance and detection efficiency of CLAS for electrons within ₁₂₅₂ the kinematic bin in question (including cuts and trigger efficiency), and ₁₂₅₃ the background Bg comes from several sources, including pions misidentified ₁₂₅₄ as electrons, electrons from $e^+ e^-$ pair production, and electrons scattered off ₁₂₅₅ (partially) polarized target nucleons and nuclei that are not the

intended species (e.g., bound protons in ^{15}N , free proton contamination in nominal ND_3 targets, and bound proton-neutron pairs in any ^{14}N contamination present)¹.

Our main goal is to extract the spin structure function g_1 and calculate its moments. The cross section difference $\Delta\sigma(W, Q^2)$ on the right side of the above equation is what contains the information on $g_1(W, Q^2)$ along with various other contributions.² This means we can, in principle, calculate the cross section (and then use that to extract g_1), from the background corrected measured quantity $\Delta n(W, Q^2)$ by putting in the values for all the rest of the quantities involved in Eq. 4.2. But, in reality, having an accurate knowledge of Acc and Eff is challenging and the available measurements of polarizations and luminosities are not reliable enough. So, experimentalists usually resort to Monte-Carlo simulation to determine some or all of those factors that are involved in the relation between the counts and cross-section differences.

A standard way to extract the sought-after Physics quantities from these kinds of measurements proceeds along the following steps [38]:

1. Use a full simulation of CLAS with a “realistic” event generator, detector simulation and event reconstruction including cuts to obtain the product AccEff as the ratio of events reconstructed in a particular bin, divided by events thrown in that same bin.
2. Extract the product $\mathcal{L}_r \cdot P_b P_t$ from the ratio of the acceptance and efficiency corrected Δn in the (quasi-)elastic region ($0.9 < W < 1.0$) to the well-known theoretical cross section difference for elastic (or quasi-elastic) scattering off the proton (deuteron).
3. Estimate and correct for Bg .
4. Apply radiative corrections, which use a model of the unradiated Born cross section and a calculation of the radiated cross section based on programs like RCSLACPOL (see below).

¹While this background is a small correction for hydrogen targets, in the case of deuteron targets, it must be corrected for (see Sec. 5.1).

² $\Delta\sigma(W, Q^2)$ also has contributions from the unmeasured g_2 or, equivalently, from the product $A_2 F_1$. Moreover, the cross section receives modifications and tails from radiative effects (both internal and external radiation) and kinematic resolution smearing.

- 1285 5. Express the extracted Born cross section difference in terms of the de-
 1286 sired quantity (here: g_1) and additional inputs (e.g., A_2F_1). Use a
 1287 model for the latter to extract g_1 only. Vary the model (concurrently
 1288 with the model input to the previous step) to assess systematic uncer-
 1289 tainties.

1290 One conceivable problem with this approach lies in the first step, and in
 1291 particular with the choice of the “realistic event generator”. However, this
 1292 choice would not matter at all if two conditions are fulfilled [38]:

- 1293 1. The kinematic bins are chosen so small that the variation of the cross
 1294 section over the bin (and/or the corresponding variation of the accep-
 1295 tance times efficiency) do not lead to any significant deviations for the
 1296 *average AccEff* between the simulation and the real detector.

 1297 2. The counts reconstructed within any one bin are directly proportional
 1298 to the number of initial electrons generated within that *same* bin (the
 1299 proportionality constant being *AccEff*), without any “bin migration”
 1300 from other kinematic bins. (Otherwise, the ratio reconstructed/generated
 1301 depends on those “migration tails”, and the simulation will give differ-
 1302 ent results from the “true value” if the overall cross section model of
 1303 the generator is not accurate enough.)

1304 Unfortunately, assumption 1 tends to directly contradict assumption 2
 1305 because 1 favors small bins and 2 favors large bins! For most precision
 1306 experiments, bin migration effects are significant. This is aggravated by
 1307 the difficulty of making a clean separation between bin migration due to
 1308 detector resolution alone and the contribution from radiative effects. For
 1309 instance, GEANT and therefore GSIM includes (at least by default) photon
 1310 radiation as part of the simulation of outgoing electron tracks throughout
 1311 the gas and building materials of all detectors. It is very important not to
 1312 “double count” when simulating an experiment; the radiative calculations in
 1313 step 4 above should not include any “after” radiation beyond the limit of
 1314 the target itself (which, in turn, should then **NOT** be included in the GSIM
 1315 simulation as material to be traversed).

1316 This is a problem for all CLAS experiments attempting to extract abso-
 1317 lute cross sections (or, here, cross section differences); however, the problem
 1318 is magnified for our case: Since the cross section difference itself is not re-
 1319 quired to be positive, one can have both positive and negative tails migrating

1320 into adjacent bins. In any case, it is clear that using the average, **unpolarized**
1321 cross section as a model for the generator is not really appropriate (unless
1322 one is confident that the asymmetry is fairly constant or slowly-varying – not
1323 a good assumption in the resonance region where the $\Delta(1232)$ with negative
1324 asymmetry is adjacent to the S11 with positive asymmetry). Using a (hope-
1325 fully realistic) model of the cross section difference instead would be much
1326 better, but this causes two new problems [38]:

- 1327 1. Prima facie it is unclear how to simulate a negative cross section (dif-
1328 ference). This problem can be circumvented fairly easily (see below),
1329 albeit at extra cost in terms of simulation effort.
- 1330 2. It obviously becomes impossible to extract $AccEff$ from a simple ratio
1331 of reconstructed divided by generated events; both of these quantities
1332 could be positive, negative (even different sign under extreme circum-
1333 stances), or simply zero (which is particularly bad for the denominator).
1334 From this discussion, it is also clear that such a ratio would depend very
1335 sensitively on the cross section model and bin migration tails and be a
1336 very poor indicator of the actual product $AccEff$.

1337 For this reason, we decided to try a different approach outlined in the
1338 following. The basic idea is to study the dependence of the reconstructed
1339 count difference on the model input (in particular g_1) directly through the
1340 whole chain of simulation and reconstruction, and then use tables of Born
1341 and radiated cross section differences for various model inputs as estimates
1342 of systematic uncertainties³.

1343 4.1.1 Outline of the method

1344 The basic idea is the following: If we already had a perfect model of g_1 and all
1345 other ingredients that go into Δn (including a perfect simulation of CLAS), a
1346 simulation of Δn would agree 100% with the data (within statistical errors).
1347 Any (larger than statistical) deviation between such a simulation of Δn and
1348 the data can only be due to the following possible sources:

- 1349 1. The model for g_1 is not perfect and, therefore, must be adjusted to
1350 reflect the “true” g_1 . This is the default assumption which we will use

³We developed this method for the case of an ND₃ target; however, it could, of course, easily be adopted to NH₃, as well

1351 to extract g_1 from the data. This will be done by finding the proportionality factor between *small* changes in g_1 and the reconstructed Δn
1352 and then adjusting g_1 to fully account for the observed Δn .
1353

- 1354 2. There could be a systematic error on this proportionality factor (which,
1355 after all, will come from simulation); for instance, there could be sys-
1356 tematic deviations from the simulated results for acceptance and effi-
1357 ciency (in particular efficiencies of the CC, EC, or tracking, that are
1358 not perfectly simulated by GSIM). This is a multiplicative uncertainty
1359 that must be carefully estimated and applied to the final data.
- 1360 3. Any imperfect simulation of the “background” due to all events not
1361 originating in the bin in question (migration, radiation), or due to
1362 undesired target components (hydrogen, bound polarized nucleons in
1363 nitrogen), or from misidentified pions or e^+e^- pairs, or due to contribu-
1364 tions to $\Delta\sigma$ from A_2 can lead to an additive systematic deviation
1365 that would then be misinterpreted as a change in g_1 . This systematic
1366 uncertainty must be studied by varying model inputs, parameters etc.
1367 in the simulation.

1368 4.2 Radiative Corrections

1369 The physics quantities that we seek to extract from measurements are theo-
1370 retically defined or interpreted and calculated in terms of the cross-section of
1371 the so called “Born” scattering process, which is represented by the simplest
1372 possible Feynman diagram i.e., by the lowest order approximation of a single
1373 photon exchange process. However, the measured cross-sections also contain
1374 contributions from higher order electromagnetic processes, which must be
1375 accounted for before extracting the quantities of our interest. These additional
1376 contributions are grouped into two categories - **internal and external**
1377 radiative corrections.

1378 The **internal corrections** are the contributions from the higher order
1379 QED processes (higher order Feynmann diagrams) which occur during the
1380 interaction. These include the correction for the internal Bremsstrahlung
1381 (i.e., the emission of a real photon while a virtual photon is being exchanged
1382 with the target) by the incoming or the scattered electron), the vertex correc-
1383 tion (in which a photon is exchanged between the incoming and the scattered
1384 electron), and the correction for the vacuum polarization of the exchanged
1385 virual photon (e^+e^- loops).

1386 External corrections include those that account for the energy loss (mainly
1387 by the Bremsstrahlung process) of electrons well before or after the interac-
1388 tion while passing through the target material and the detector.

1389 If the beam electron radiates a photon before the scattering, the kinemat-
1390 ics of the actual process will be different from the the one calculated with the
1391 nominal beam energy. Likewise, if the radiation occurs after the scattering,
1392 the actual energy and momentum of the scattered electron will be different
1393 from what is calculated normally (i.e., without any radiation). The effect
1394 can be quite large for elastic scattering.

1395

1396 4.3 “Standard” simulation

1397 The simulation process consists of mainly three parts - generating inclusive
1398 events similar to the ones produced in the double polarization scattering
1399 process, simulating the CLAS detector response, and finally the event recon-
1400 struction from the simulated detector signals.

1401 The first part is accomplished by using a program that is made by com-

1402 bining the essential elements of an updated version of the “RCSLACPOL”
1403 program (for cross section generation) and some parts of the “STEG” (SimplesT Event Generator) event generator (see sections 4.3.1 and 4.3.2). The
1404 second part is done by two standard CLAS software packages running in
1405 succession - “GSIM” and “GPP”(see sections 4.3.3 and 4.3.4). And, finally,
1406 the standard CLAS package “RECSIS” is used to reconstruct the events in
1407 the same way as for the real CLAS data.
1408

1409 4.3.1 RCSLACPOL

1410 The simulation for the standard model cross sections proceeds as follows.
1411 We use the code “RCSLACPOL” [39] that can generate polarized and un-
1412 polarized cross sections (both Born and radiated) based on the approach by
1413 Shumeiko and Kuchto [40] as well as Mo and Tsai [41], including external
1414 radiation in the target. This code has been extensively tested and used for
1415 the analysis of SLAC experiments E142, E143, E154, E155 and E155x as
1416 well as Jefferson Lab experiments like EG1a and EG1b. It has been updated
1417 with the most recent models on polarized and unpolarized structure func-
1418 tions (F_1 , F_2 , A_1 and A_2) [39, 42–44] and an implementation of the folding
1419 algorithm developed by W. Melnitchouk and Y. Kahn [45] for structure func-
1420 tions of the deuteron. The models have been fitted to and tested with data
1421 from EG1b as well as world data on both A_1 and A_2 over a wide range of Q^2
1422 and W , including the resonance region and the DIS region.

1423 For EG4, we have combined the “RCSLACPOL” code with that of the
1424 “STEG” event generator. This generator uses a grid of (radiated⁴) cross sec-
1425 tions generated by our modified version of RCSLACPOL to generate events
1426 that are distributed according to these cross sections (i.e., the number of
1427 events generated in a given bin is proportional to the cross section integrated
1428 over this bin).

1429 4.3.2 Event Generator

1430 The concept and some part of the generator skeleton was inherited from the
1431 STEG (SimplesT Event Generator) program obtained from INFN, in Genova,
1432 Italy. The old event sampling part (which made the program run extremely

⁴Radiative effects are simulated by passing RADB and RADA as input parameters to the RCSLACPOL program, where RADB and RADA are the average radiation lengths of the materials that the electron passes through before and after scattering.

1433 slow) of the code was replaced by a new one developed by myself which
1434 made the event generation process much faster. The cross section calculating
1435 part was replaced by codes from an updated version of RCSLACPOL (see
1436 Sec. 4.3.1).

1437 The generator works in two steps. First, it generates two separate two-
1438 dimensional maps or tables (in $(p, \cos \theta)$ space) of radiated inclusive polarized
1439 cross differences (for the scattering of polarized electrons from a longitudinally
1440 polarized deuteron target, by using RCSLACPOL) in various kinematic
1441 bins encompassing the kinematic region covered by EG4 data. One map is for
1442 positive values of polarization $\Delta\sigma$ and the other is for negative values of the
1443 polarization. These cross section maps (and the corresponding events later
1444 on) were generated in the following angular and momentum ranges: 5.0-45.0
1445 degrees for θ , 250.0-325.0 degrees for ϕ (to ensure the CLAS 6th sector is
1446 completely covered) and $(0.2, E_{beam})$ GeV for the momenta ($p \approx E'$), where
1447 the beam energy E_{beam} took values of 1.337 and 1.993 GeV, corresponding to
1448 the two ND₃ data sets of EG4. In our case, the map was created by dividing
1449 the kinematic phase space into a grid of small rectangles and then calculating
1450 the differential cross-section at the geometric center of each of those squares
1451 (such as ABCD in Fig. 4.1). For our application, we need to generate two
1452 such maps (because of the impossibility of generating events according to
1453 negative cross-sections) and run the program twice - once corresponding to
1454 positive $\Delta\sigma$ and the next for the negative one. For all bins in which the integrated
1455 cross section $\Delta\sigma \geq 0$, we fill the first table (“positive map”) which is
1456 therefore positive-definite. For all bins in which this cross section is below 0,
1457 we fill a second table (“negative map”), but with the absolute (i.e. negative)
1458 value of this cross section.

1459 In the second stage, events are thrown according to the cross section maps
1460 produced in the first stage. The events are given vertex coordinates that are
1461 uniformly distributed over the volume of a 1 cm long cylinder with radius
1462 0.01 cm around the beam line - with the center of this volume being at the
1463 EG4 target position of (0,0,-100.93 cm). Nearly equal numbers of events are
1464 generated for each sign of $\Delta\sigma$; they are finally normalized according to their
1465 total cross sections (integrals of the corresponding maps).

1466 The kinematic and other information (positions, momenta, charge) of
1467 these generated events are recorded and saved in the BOS format⁵ output
1468 files which organizes data into banks. In our case, HEAD, MCEV, MCTK,

⁵Existing versions of GSIM, GPP and RECSIS accept only BOS format for input files.

1469 and MCVX banks are used for the generator output. The generator is also
 1470 capable of producing output in the hbook format which makes it possible
 1471 to study the Monte Carlo data using PAW (or ROOT because the h2root
 1472 program easily converts “hbook” files into “root” files).

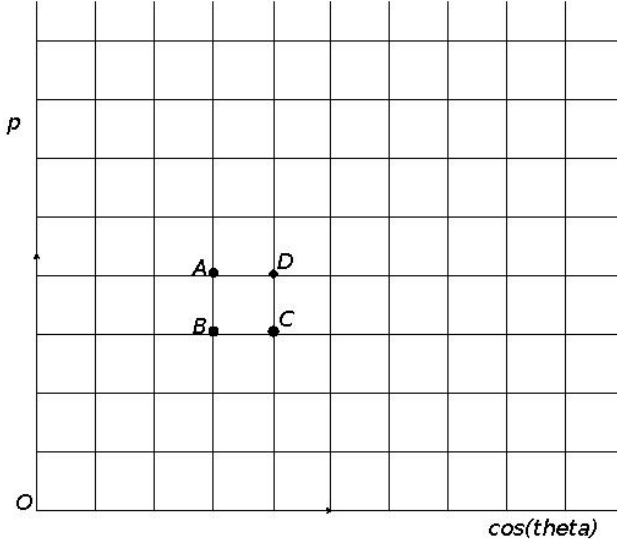


Figure 4.1: Corners of a typical bin highlighted in the kinematic space covered by the event generator.

1473 **4.3.3 GSIM - CLAS Detector Simulation**

1474 The Monte Carlo events thus generated are next fed into GSIM - the CLAS
 1475 Monte Carlo simulation program using GEANT 3.21 libraries from CERN
 1476 [46]. It simulates the CLAS detector response by implementing a complete
 1477 model of the detector as well as the propagation of particles through different
 1478 materials including all physics processes, such as multiple scattering, energy
 1479 loss, pair production, and nuclear interactions. The program takes the in-
 1480 put event particles and then, based on their types, momenta and positions,
 1481 “swims” (traces) them through all volumes of different materials that are
 1482 defined using various library routines and the detector parameters. Charged
 1483 particles are also subjected to the effects of the torus and target magnetic
 1484 fields of the same strength as in the actual experiment (for this the same field
 1485 maps are used as in the track reconstruction process using RECSIS). All the

1486 ingredients of the program (field maps, active detection volumes, passive vol-
1487 umes of detector support structures etc) are modeled as accurately as possible
1488 with the help of engineering designs and actual detector measurements. Spe-
1489 cial subroutines corresponding to various active parts of the detector produce
1490 outputs resembling the real detector signals which can then be reconstructed
1491 and analyzed just as the real experimental data [47][48]. GSIM is configured
1492 to match with the conditions of a given experiment by giving it proper val-
1493 ues of input parameters via a command line input file which contains various
1494 “ffread cards” some of which are listed in table-A.1 along with their values
1495 that were used in our simulation.

1496 4.3.4 GSIM POST PROCESSOR (GPP)

1497 The GSIM output is next passed onto GPP - another standard CLAS soft-
1498 ware package - to process the simulated data further so that the detector
1499 response is accounted for more accurately. This package improves the re-
1500 sponse by smearing the detector signals and removing them if there are dead
1501 regions (determined by querying a data base which in turn is made by looking
1502 at the raw data of the experiment).

1503 A lot of known, unknown, quantified, and unquantified factors such as
1504 temperature, alignment, dead channels, electronic malfunction etc affect the
1505 performance of the CLAS detector. But, GSIM does not include all these
1506 effects and, hence, the efficiency of the detector is always less than what
1507 the simulation provides us. To make the simulation more realistic by taking
1508 into account some of those effects, another CLAS software called GSIM Post
1509 Processor (GPP) is used to process the GSIM output. The GPP can change
1510 the DC, SC, CC and EC signals produced in the simulation⁶.

1511 As the experimental conditions and detector configurations can change
1512 from one experiment to another, in order to run the GPP, we must have
1513 our own experiment specific calibration constants and parameters such as
1514 the run number (R), the DC smearing scale values for regions 1, 2 and 3
1515 (a, b, c) and the SC smearing scale value (f). Even for a given experiment,

⁶The DC signals can be changed by (a) accounting for the dead wires according to the calibration database, (b) shifting the DOCA mean value, and (3) smearing the hit signals according to the resolution determined by the calibration database or according to the command line input. Likewise, SC signals can be changed with a parameter input for smearing the time resolution. And, for EC signals, the GPP can use the hardware thresholds [49].

1516 these constants and parameters are determined to be different for different
1517 data sets (corresponding to a given beam energy, for example). The value
1518 for R can be any run number belonging to a specific data set. This number
1519 is used to identify the entry of the calibration constants in the database that
1520 corresponds to the given data set. In order to simplify the job, we decided to
1521 use the timing resolutions determined by the calibration database assuming
1522 that they are good enough and need only to determine new values for the
1523 DC smearing. To further simplify the job, we assumed that the three DC
1524 Regions had identical resolutions, so the DC smear parameters a, b, and c
1525 would have the same values, and the common DC-smear value is what is
1526 determined from the procedure described below.

1527 In order to determine the DC-smear, we generated a statistically signif-
1528 icant number (about half million) of elastic-electron events distributed ac-
1529 cording to the elastic cross section and then ran them through GSIM, GPP
1530 and RECSIS. The pure proton target events, turning off the radiative effects
1531 are generated using the existing STEG event generator.

1532 The simulated elastic events are then fed into GSIM, GPP and RECSIS,
1533 with GSIM and RECSIS used in the same configuration as when processing
1534 the CLAS data during the “pass-1” phase, and GPP run with different values
1535 of DC-smear scales as inputs. The reconstructed data coming out of RECSIS
1536 corresponding to a given value of DC-smear is then histogrammed in ΔE
1537 again and fitted to a Gaussian to get its σ (characterizing width) and mean
1538 (characterizing position). As we can see in figures 4.2(a) and 4.2(b), the width
1539 of the elastic peak increases with the DC-smear but the position stays more
1540 or less the same as expected. In fact, when the two are plotted against DC-
1541 smear (as in figures 4.3(a) and 4.3(b)) the width shows a linear dependance.

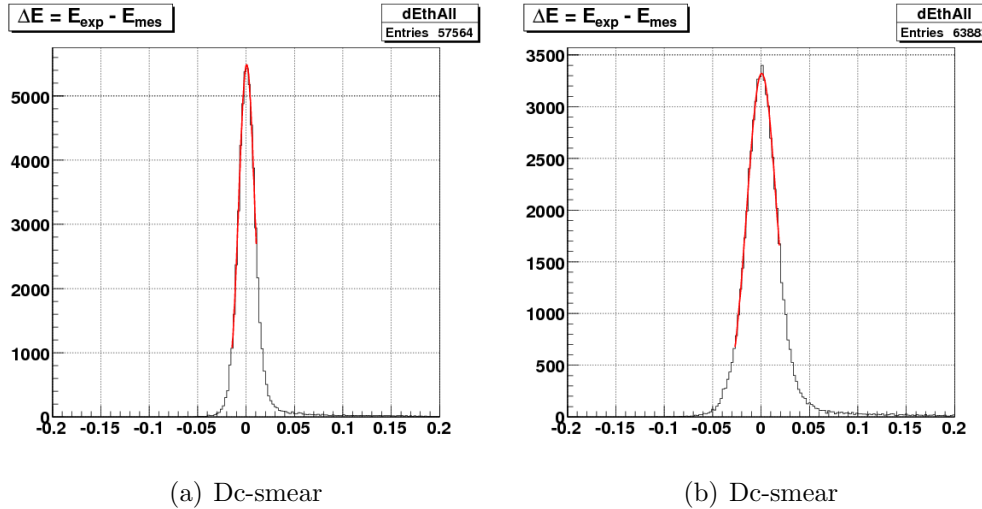


Figure 4.2: ΔE of 2.3 GeV simulated elastic-only proton-target events passing through GSIM, GPP (with two different Dc-smear scales of 1.3 (a) and 2.9 (b)), and RECSIS.

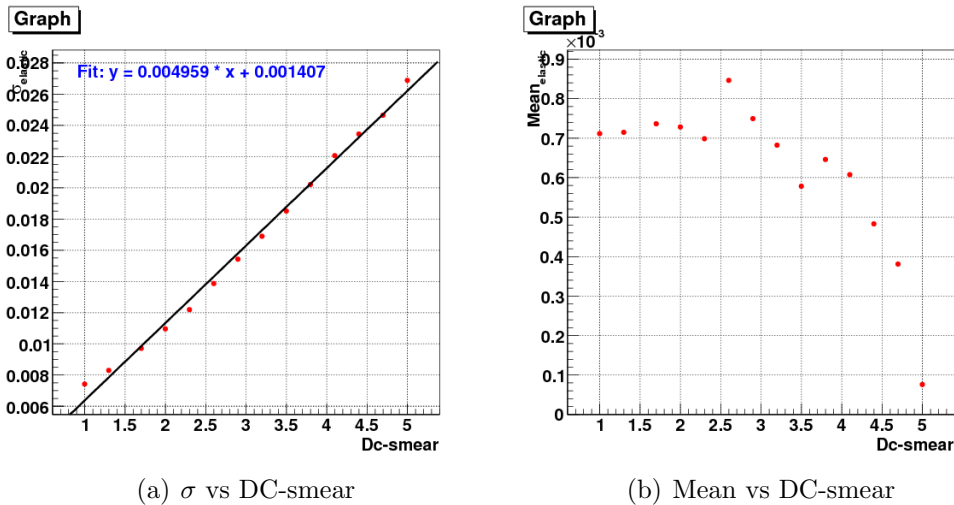


Figure 4.3: Graphs showing the dependence of width and position (obtained from the Gaussian fits as shown in the fig (??) of the elastic peaks on the DC-smear applied to GPP.

With the knowledge of the DC-smear dependence of energy resolution

1543 (Fig. 4.3(a)), we can look at the resolution in the real data such as the
 1544 one estimated in Fig. 3.26, and then determine the right value of DC-smear
 1545 which would make the resolution in the simulation comparable with that
 1546 in the real data. By repeating this process of comparing the experimental
 1547 and simulated resolutions for each of the beam energies, the values of the
 1548 DC-smear parameters for the GPP were determined as listed in Table. 4.1
 1549 below.

Table 4.1: DC-smearing scales determined for different beam energies.

E_{beam} (GeV)	1.054	1.339	1.989	2.256	2.999
DC-smear	2.6	2.0	2.0	2.0	1.7

1550

1551 4.4 Comparison of Data and Simulation

1552 Using our final values for the smear parameters, the simulated data were
 1553 passed through GPP and then reconstructed with RECSIS. Finally, all ap-
 1554 plicable cuts and corrections were applied to both sets of polarized simula-
 1555 tion data. Because the CC was turned off in GSIM for the simulation, all
 1556 experimental data cuts except those depending on CC were applied to the
 1557 simulated data. However, the cuts were modified (see Sec. 3.3) to account
 1558 for differences between simulation and data.

1559 In the end, we had two sets of simulated events (for the two cases of
 1560 $\Delta\sigma \geq 0$ and $\Delta\sigma < 0$) in each kinematic bin. The number of these two
 1561 type of events in each bin were then cross-normalized with respect to each
 1562 other by their respective cross-section map integrals and the number of gener-
 1563 ated Monte-Carlo events and then combined to make the simulated polarized
 1564 count difference Δn . To do that, the number of simulated event counts in
 1565 a kinematic bin corresponding to the positive $\Delta\sigma$ was kept unchanged but
 1566 the one corresponding to the negative $\Delta\sigma$ was multiplied with the following
 1567 normalization factor:

$$norm^- = \frac{\sigma_{tot}^-}{\sigma_{tot}^+} \times \frac{N^+}{N^-} \quad (4.3)$$

1568 where $\sigma_{tot}^{+/-}$ and $N^{+/-}$ are the total integral of the cross section map and

1569 the corresponding number of Monte-Carlo events generated for each of the
1570 polarization cases (+/-).

1571 The next step was to properly cross-normalize the simulated events to
1572 the data. For this, we found the scale factor SF necessary to have the same
1573 Δn in the quasi-elastic region (e.g., $0.9 \leq W \leq 1.0$). This factor represents
1574 the ratio

$$SF = \frac{n^+ - n^-}{\Delta n(simul)} \quad (4.4)$$

1575 since the physics of QE is known (from form factors etc), we expect the
1576 simulation in this region is reliable and all other factors⁷ are common to the
1577 simulation and the data. In fact, we chose one Q^2 bin (the 20th one - for
1578 which the agreement between the data and simulation was among the best)
1579 and calculated above ratio to get the global preliminary value of the scaling
1580 factor SF_{20} . The simulated Δn was then multiplied with this factor to get
1581 our best “prediction” of the real data in all the kinematic bins, in order to
1582 directly compare it with the real data (see Figs. 4.4 and 4.5).

⁷The scaling factor (SF) accounts for the luminosity, the product of the beam and target polarization ($P_b P_t$, and all other constant efficiency factors such as dead time, overall trigger efficiency, average tracking efficiency etc.

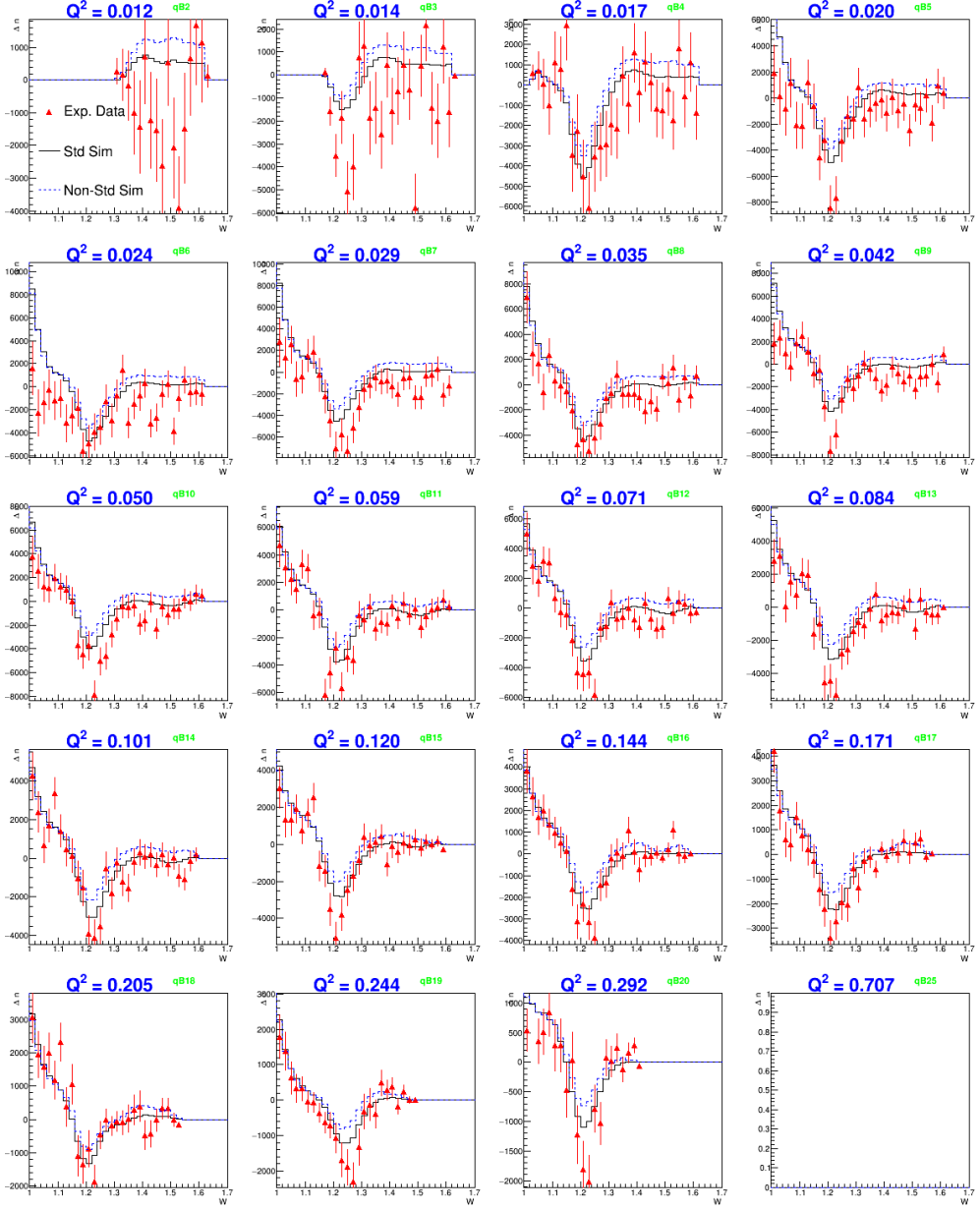


Figure 4.4: Comparison (in different Q^2 bins) of polarized count differences from 1.3 GeV experimental (red points with error bars) and two versions of normalized simulation data. The black continuous histograms are for “standard” simulation with values of A_1 in the inelastic region as given by the model used in the simulation. The blue dotted histograms are for “non-standard” simulated data with A_1 changed to $A_1 + 0.1$.).

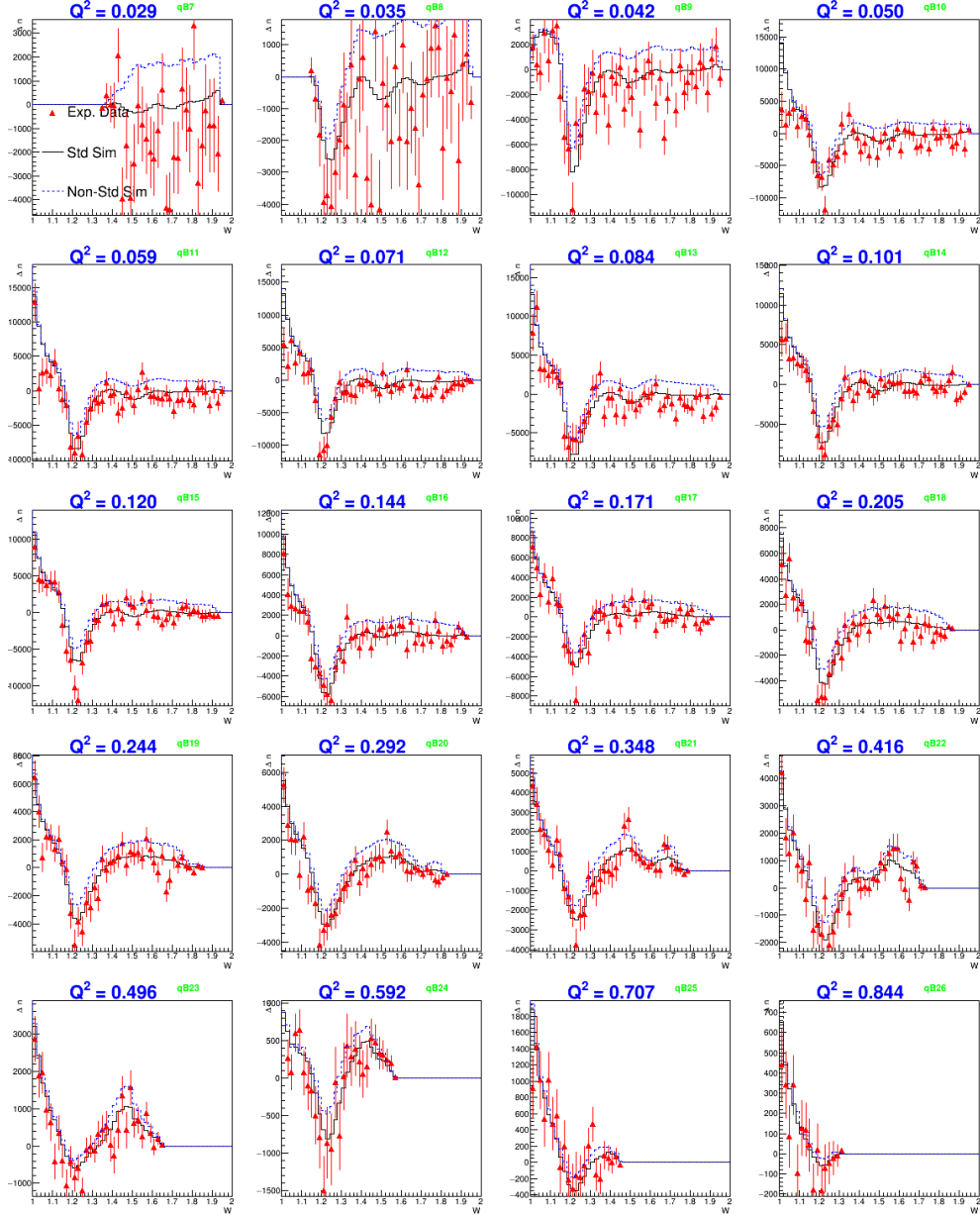


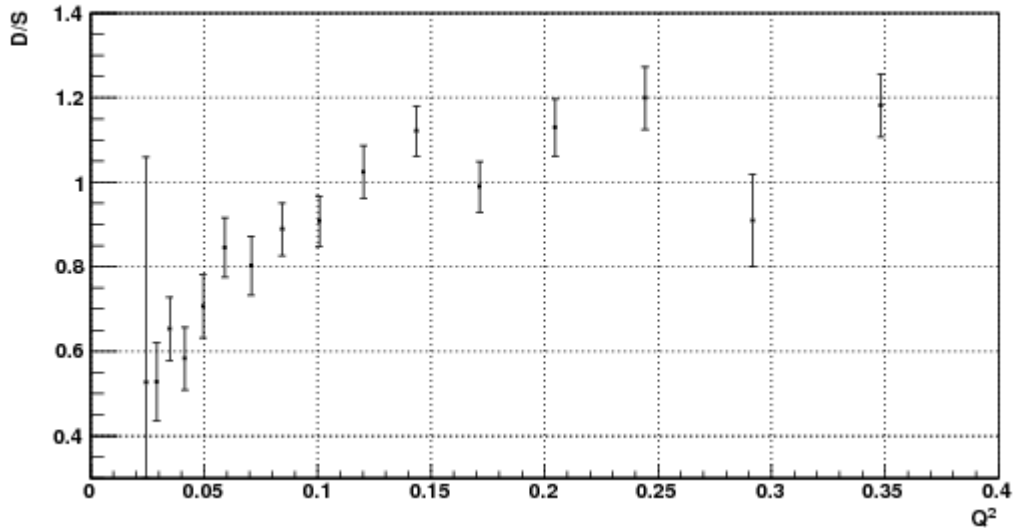
Figure 4.5: Comparison (in different Q^2 bins) of polarized count differences from 2.0 GeV experimental (red points with error bars) and two versions of normalized simulation data. The black continuous histograms are for “standard” simulation with values of A_1 set as given by the used model. The blue dotted histograms are for “non-standard” simulated data with A_1 changed to $A_1 + 0.1$.

1583 After this normalization, the ratios $(n^+ - n^-)/\Delta n(simul)$ in the quasi-
1584 elastic region for all Q^2 bins were calculated and plotted versus Q^2 as well
1585 as θ (see Figs. 4.6(a) - 4.9(a)) along with the corresponding statistical errors
1586 as given by $\sqrt{(n^+ + n^-)/\Delta n(simul)}$. As the figures show, the ratio in the
1587 quasi-elastic region drops off rapidly at small Q^2 . The fall-off is likely due to
1588 CC inefficiencies for very high momenta and very forward angles. Also, our
1589 simple cross section model for the deuteron is less accurate at low Q^2 . Figs.
1590 4.6(b) - 4.9(b) show that the Δ -resonance region does not suffer from similar
1591 problems as the Delta model is quite reliable too (just like QE model).

1592 The final normalization was obtained by calculating the error weighted
1593 average $SF_{average}$ of above ratios in the quasi-elastic region. The average was
1594 calculated using only those Q^2 bins which had ratios reasonably stable and
1595 closer to each other. Because, the ratios are reasonably stable only above
1596 $Q^2 \approx 0.045 \text{ GeV}^2$ and $Q^2 \approx 0.09 \text{ GeV}^2$ in the 1.337 and 2.0 GeV data sets
1597 respectively (as can be seen from Figs. 4.6(a) and 4.8(a)), only those Q^2 bins
1598 above these two limits were used in calculating the weighted average of these
1599 ratios. In addition, even above those two limits, some of those which had
1600 too large ratios - greater than 2.0 (or 2.5) for 1.337 (or 2.0) GeV data set-
1601 were not used in the weighted average. However, it should be noted that the
1602 bins not used in the average ratio calculations were not entirely discarded
1603 from the final analysis. Only those below $Q^2 = 0.02 \text{ GeV}^2$ were completely
1604 thrown out from the final analysis because they did not cover the resonance
1605 (particularly the Δ) region very well. The resulting simulated data in the
1606 form of count differences Δn in various Q^2 bins are shown in Figs. 4.4 and
1607 4.5 along with the corresponding experimental data.

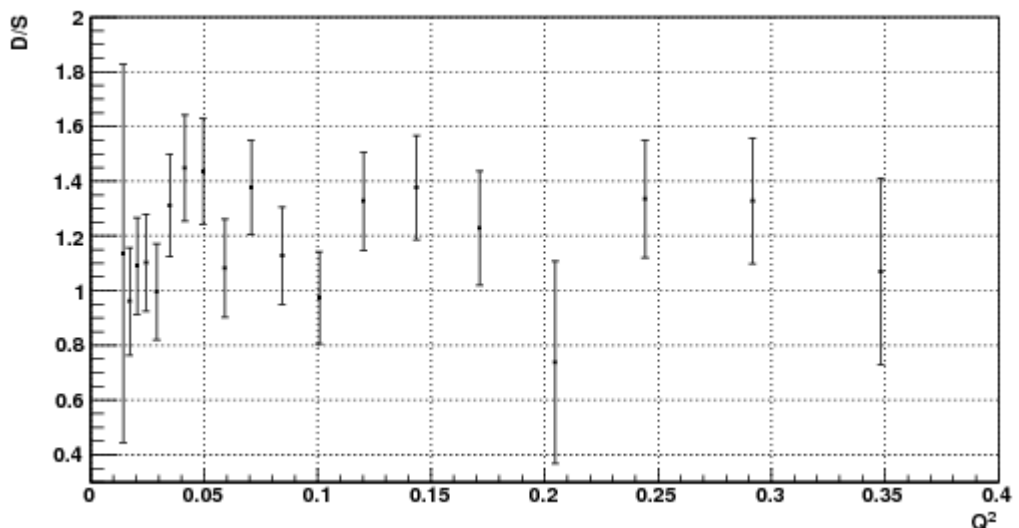
1608 A complete systematic error analysis was done to study the effect of the
1609 overall scaling factor SF on the extracted g_1 (see below) and to estimate
1610 its statistical (due to the number of counts) and systematic (due to model
1611 uncertainties and backgrounds) error.

Data/Sim for W(0.9,1.05)



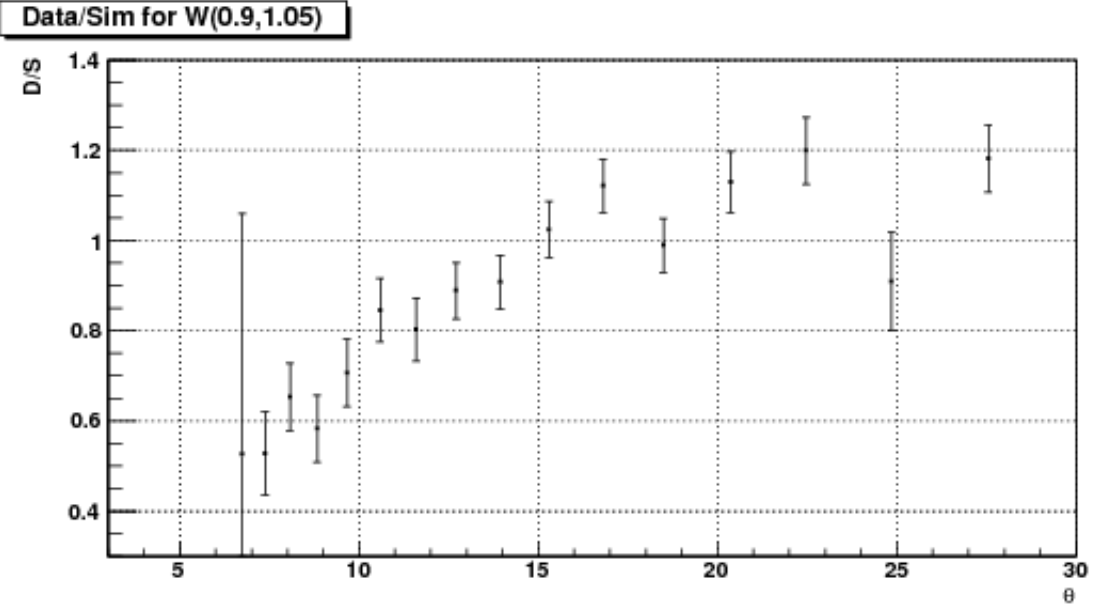
(a) Data/Sim ratio vs Q^2 in 1.3 GeV quasi-elastic data.

Data/Sim for W(1.15,1.3)

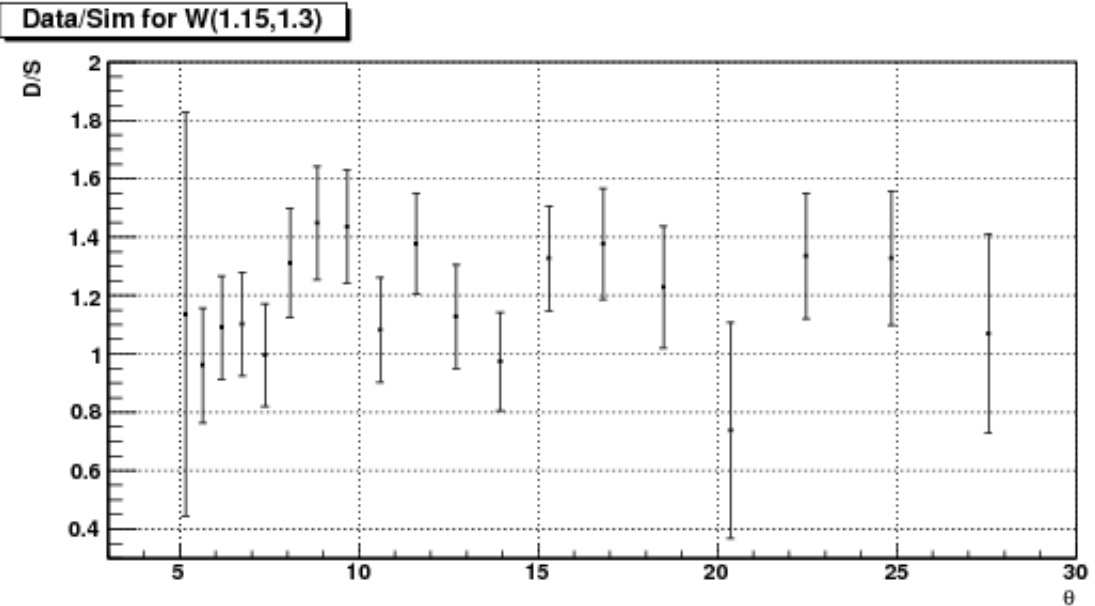


(b) Data/Sim ratio vs Q^2 in Δ -resonance region of 1.3 GeV data.

Figure 4.6: Q^2 dependence of ratios of 1.3 GeV data and simulation in the quasi-elastic and Δ -resonance regions.



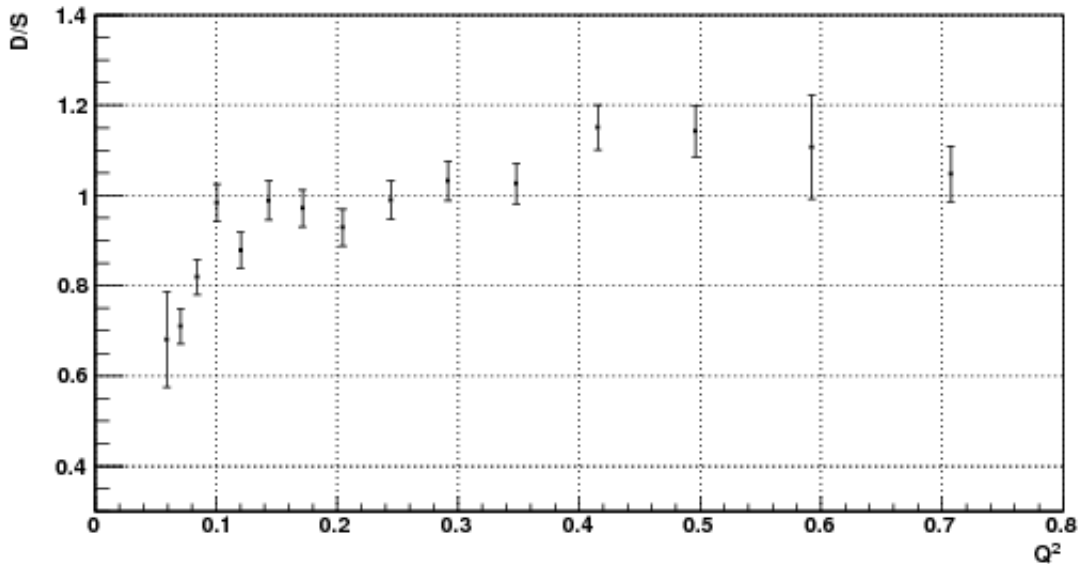
(a) Data/Sim ratio vs θ in 1.3 GeV quasi-elastic data.



(b) Data/Sim ratio vs θ in Δ -resonance region of 1.3 GeV data.

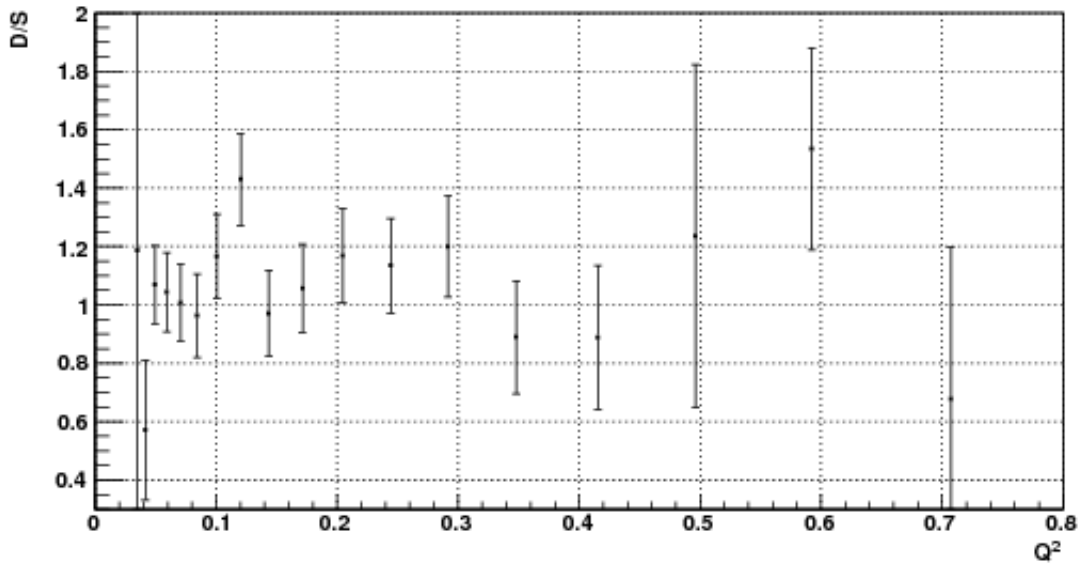
Figure 4.7: The same data as in Fig. 4.6, but plotted versus average scattering angle (θ). Here we can see that the data for $\theta > 10^{\circ}$ are reasonably stable with $\pm 10\%$ fluctuation (which will be taken into account while calculating the systematic uncertainty later.

Data/Sim for W(0.9,1.05)



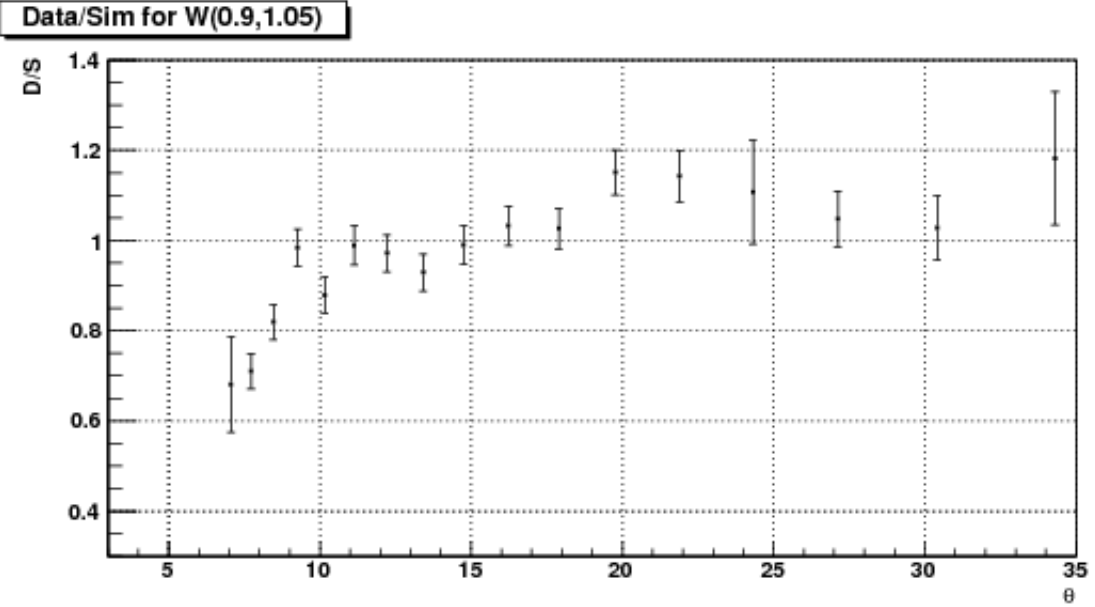
(a) Data/Sim ratio vs Q^2 in 2.0 GeV quasi-elastic data.

Data/Sim for W(1.15,1.3)

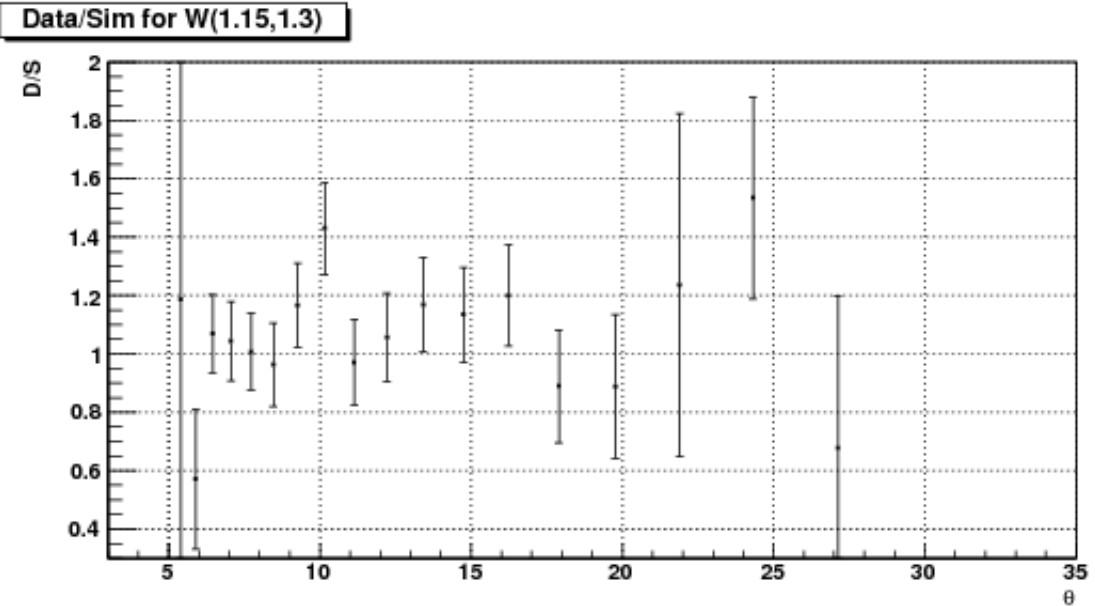


(b) Data/Sim ratio vs Q^2 in Δ -resonance region of 2.0 GeV data.

Figure 4.8: Q^2 dependence of ratios of 2.0 GeV data and simulation in the quasi-elastic and Δ -resonance regions.



(a) Data/Sim ratio vs θ in 2.0 GeV quasi-elastic data.



(b) Data/Sim ratio vs θ in Δ -resonance region of 2.0 GeV data.

Figure 4.9: The same data as in Fig. 4.8, but plotted versus average scattering angle (θ). Here we can see that the data for $\theta > 10^{circ}$ reasonably stable with $\pm 10\%$ fluctuation (which will be taken into account while calculating the systematic uncertainty later.

1613 4.5 Method to Extract g_1 and $A_1 F_1$

1614 4.5.1 ‘Variation’ of the standard simulation

The whole chain of steps outlined in the previous sections for the standard simulation is repeated with just one major difference: the model input for the asymmetries A_1 for both the proton and the neutron are increased by a constant value⁸ of 0.1. With all other model ingredients being kept constant, this change leads to a change of the spin structure function g_1 that can be straightforwardly calculated for each kinematic bin within the model:

$$\delta g_1(W, Q^2) = \delta A_1 \times F_1 \frac{\nu^2}{\nu^2 + Q^2} \quad (4.5)$$

1615 Correspondingly, the simulated count difference $\Delta n(W, Q^2)$ will change to
 1616 a new value $\Delta n'$. This ‘non-standard’ simulation with $A_1 = A_1(\text{standard}) +$
 1617 0.1 is performed generating an about equal number of Monte-Carlo events.
 1618 The final reconstructed data is then multiplied with the same overall scaling
 1619 factor SF as for the standard simulation and then further (cross-)normalized
 1620 by one additional factor $SF_{ext} = (\sigma_1^p / \sigma_2^p) / (N_1 / N_2)$ to account for the change
 1621 in cross section map and the (slight) difference in the number of the generated
 1622 events between the standard and non-standard simulations. Here, σ_1^p and σ_2^p
 1623 are the total cross sections for the positive $\Delta\sigma$ maps used for the standard and
 1624 non-standard simulations and, N_1 and N_2 are the corresponding numbers of
 1625 generated events. See Fig. (4.10) to see how the polarized count differences
 1626 look (in one particular Q^2 bin) in experimental and simulated data after such
 1627 normalizations (for all other Q^2 bins, see Figs. 4.4 and 4.5).

This change of the simulated $\Delta n(W, Q^2)$ to a new value $\Delta n'$ can be correlated to the increase in g_1 by solving for the two parameters A and B of the linear equation,

$$\Delta n(\text{simul}) = A + B \cdot \delta g_1, \quad (4.6)$$

where $A(W, Q^2)$ is the result for the simulated Δn for the standard set of model inputs i.e., $A(W, Q^2) = \Delta n^{\text{standard}}(W, Q^2)$, and $B(W, Q^2)$ is the proportionality factor representing the change in $\Delta n(\text{sim})$ per unit change in

⁸We arbitrarily chose 0.1 in the inelastic region, but could also have used any other value (not too big, however).

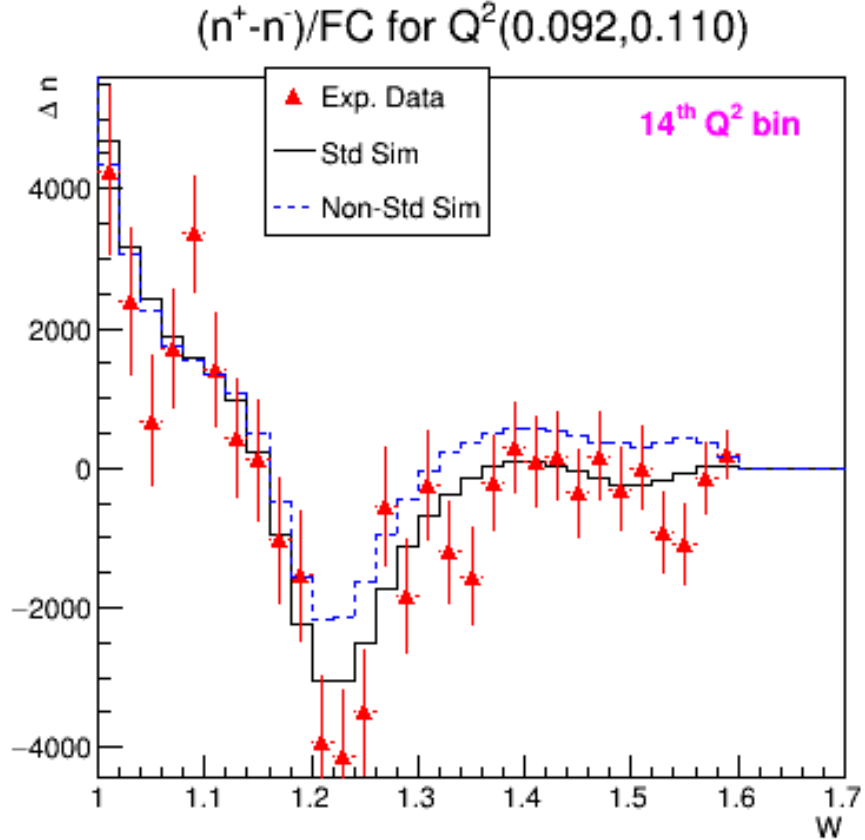


Figure 4.10: Δn of experimental data and two versions of simulations in one particular Q^2 bin for 1.3 GeV case (for data on more Q^2 bins, see Fig. 4.4).

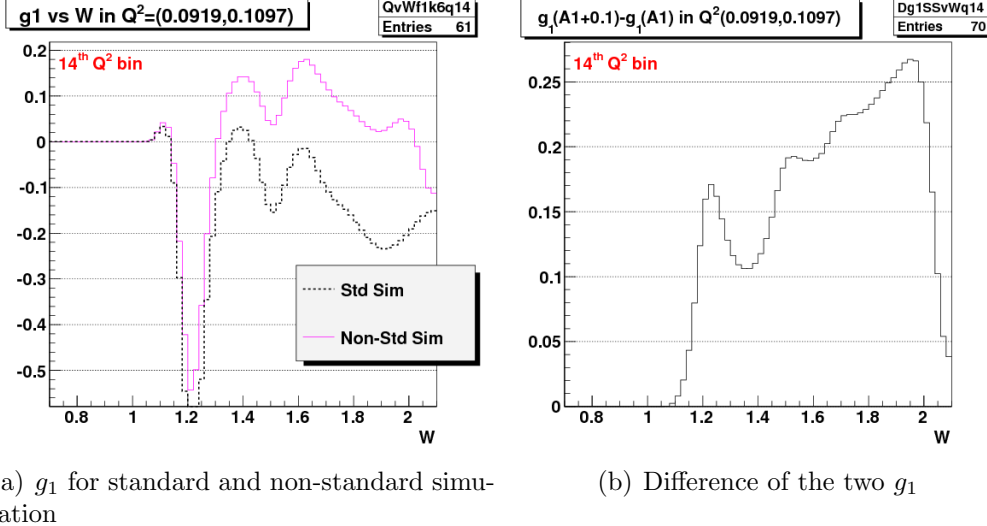
g_1 , as given by:

$$B(W, Q^2) = \frac{\Delta n' - \Delta n}{\delta g_1}. \quad (4.7)$$

Similarly, in case of $A_1 F_1$ evaluation, the factor is given by:

$$B(W, Q^2) = \frac{\Delta n' - \Delta n}{\delta A_1 F_1}. \quad (4.8)$$

The proportionality factor $B(W, Q^2)$ is then determined for each of the kinematic bins (in (W, Q^2)) in which the experimental data has been histogrammed. For this purpose, using the RCSLACPOL program, we produce two values of structure function g_1 in each kinematic bin - one is $g_1^{Standard}$



(a) g_1 for standard and non-standard simulation

(b) Difference of the two g_1

Figure 4.11: Plots showing the change in model g_1 due to the change of A_1 to $A_1 + 0.1$.

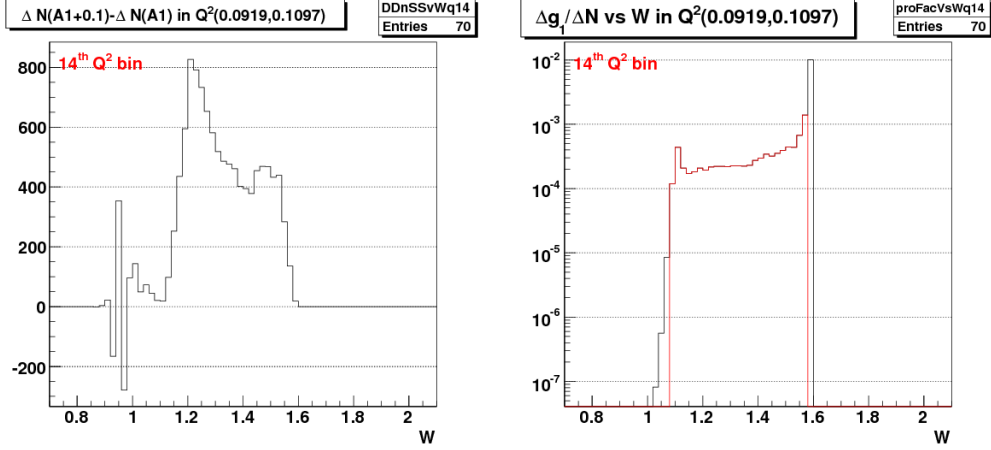
corresponding to the standard simulation and the other is $g_1^{non-standard}$ corresponding to the non-standard simulation. By dividing the above change in the count difference with the difference Δg_1 of these two structure functions, we get the factor $B(W, Q^2)$ for the bin. The similar procedure is followed to get the corresponding values of $B(W, Q^2)$ in the case of $A_1 F_1$ evaluation.

In principle (and ignoring the other enumerated possible sources of disagreement between data and simulation), we can then easily find the “amount of change” δg_1 to be added to the standard model g_1 to get perfect agreement:

$$\delta g_1 = g_1^{extr}(W, Q^2) - g_1^{Standard} = \frac{\Delta n^{data}(W, Q^2) - \Delta n^{standard}(W, Q^2)}{B(W, Q^2)} \quad (4.9)$$

where the values of Δn^{data} and $\Delta n^{standard}$ come from the polarized count differences Δn in the experimental data and the standard simulation respectively (as shown, for example, by the red points and black histograms in Fig. 4.10 for one particular Q^2 bin).

It is also straightforward to propagate the statistical uncertainty to the extracted g_1 . The statistical uncertainty in this extracted quantity totally comes from the uncertainty in the experimental counts Δn^{data} (assuming



(a) Change in $\Delta n(sim)$ simulated count difference i.e. $\Delta N = \Delta n'(A_1 + 0.1) - \Delta n(A_1)$ due to the change of A_1 to $A_1 + 0.1$ (for 1.3 GeV case).

(b) Proportionality factor ($1/B(W, Q^2)$) for 1.3 GeV case. Black is the original values. Red is the ones kept after discarding the first or last few (low statistics bins) that had unreasonably high (suddenly changing) ratios. This ensures we only show final data with “good” proportionality factor.

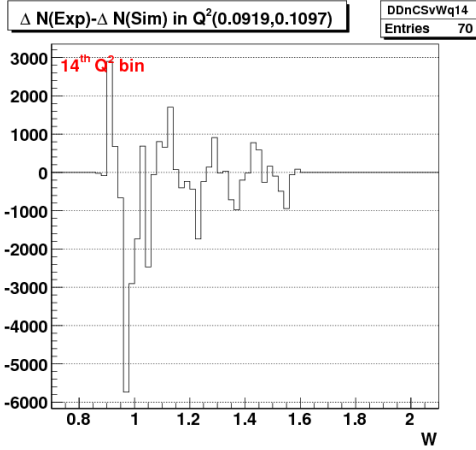
Figure 4.12: Plots for $\Delta n(sim)$ and the corresponding proportionality factors.

there is no uncertainty in the model quantities involved and also in the simulation counts because we did our simulation with large enough statistics to warrant ignoring the uncertainties) as follows:

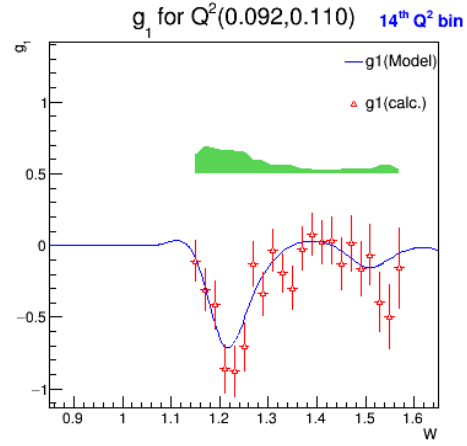
$$\sigma(g_1^{extr}(W, Q^2)) = \frac{\sigma(\Delta n^{data}(W, Q^2))}{B(W, Q^2)}. \quad (4.10)$$

The values of g_1 and its uncertainties thus extracted from 1.3 GeV data for one Q^2 bin is shown in Fig. (4.13(b)). Similar results for all the bins from two beam energy data sets in different kinematic bins can be seen in Fig. 6.1.

Because we are also interested in measuring the forward spin polarizability and the extended GDH integral, we also extract the product $A_1 F_1$ which enters these integrals. We followed the exact same procedure for g_1 as outlined above. We determined new proportionality factors in each kinematic bin, again using Eq. 4.12 as before but with the denominator replaced, this time, with the corresponding change in $A_1 F_1$ (instead of the change in g_1).



(a) $\Delta n(data) - \Delta n(sim)$ (for 1.3 GeV case).



(b) Calculated g_1 from 1.3 GeV data.

Figure 4.13: Plots for $\Delta(\Delta n)$ and the corresponding extracted g_1 . On the left, $\Delta(\Delta n)$ are the difference of the normalized count differences from the experimental and simulated (using 'standard' model) data. In other words, this gives the common numerator for Eqs. 4.12 , 4.8. On the right, the blue line is that of the model g_1 that was used in the simulation when the quasi-elastic part was turned off. We used $g_1^{extracted} = g_1^{q.e.Off} + \delta g_1$ to get the measured g_1 , where δg_1 is the calculated deviation (using Eq. 4.9) of the experimental g_1 from the model value which is derived from the deviation of the experimental polarized counts from the corresponding simulated counts.

1651 Then we can use the following expression (similar to equation 4.9) to extract
 1652 $A_1 F_1(W, Q^2)$:

$$\delta A_1 F_1 = A_1 F_1^{extr}(W, Q^2) - A_1 F_1^{Standard} = \frac{\Delta n^{data}(W, Q^2) - \Delta n^{standard}(W, Q^2)}{B_{A_1 F_1}(W, Q^2)} \quad (4.11)$$

where

$$B_{A_1 F_1}(W, Q^2) = \frac{\Delta n' - \Delta n}{\delta A_1 F_1}. \quad (4.12)$$

1653 And, the uncertainties on $A_1 F_1$ can also be dealt in the same way as on
 1654 g_1 .

- 1655 **Chapter 5**
- 1656 **Systematic Uncertainties**
- 1657 There is always a possibility that the final result(s) produced from any data
1658 analysis will be shifted from the true or ideally expected value(s) because the
1659 final result(s) are derived using the measured, modeled or estimated values
1660 of one or more other input parameters, whose values themselves usually have
1661 some systematic measurement or estimation uncertainties.
- 1662 The systematic effects due to a particular variable are studied by making a
1663 small change in the variable while holding the others constant, and measuring
1664 by how much the end result(s) changed.
- 1665 In this analysis, ten sources of systematic uncertainties are studied as
1666 listed below:
- 1667 1. Possible Uncertainty in the overall scaling factor
 - 1668 2. Effect due to the contaminations from polarized H in the target and
1669 from misidentified π^- in the scattered electrons sample.
 - 1670 3. Potential deviations in the reconstructed kinematics
 - 1671 4. Possible uncertainty in the CC-inefficiency estimation
 - 1672 5. Effect due to the e^+e^- pair symmetric contamination
 - 1673 6. Possible uncertainty in the estimation of radiation lengths
 - 1674 7. Model variation using preliminary version (v1) of A_1 model by Guler/Kuhn
1675 (2008-9)
 - 1676 8. Model variation using old version of A_2 resonance model

1677 9. Model variation of F_2 (and proportionally of F_1) while keeping R con-
1678 stant

1679 10. Model variation of R or F_1 (with F_2 unchanged)

1680 For the ease of description later on, these ten components will be referred to
1681 by the index "k" with its value indicating the position in the list. So, the
1682 uncertainty due to scaling factor will be identified with k=1 and so on.

1683 5.1 Evaluation of Experimental Systematics

Possible Uncertainty due to the overall scaling factor This uncer-
tainty is due to the uncertainties in the overall scaling factor (SF), which is a
convolution of various unmeasured constants such as $P_b P_t$, packing fraction
etc (see Sec. 4.1.1). This contribution is estimated by assuming that the
uncertainties in SF is not more than 10%. Thus considering the worst case
scenario of 10% uncertainty in SF, we estimate the corresponding uncertainty
in g_1 as follows:

$$\Delta g_1^{SF}(W, Q^2) = g_1^{std}(W, Q^2) + \frac{\Delta n^{data}(W, Q^2) - 1.1 \cdot \Delta n^{std}(W, Q^2)}{1.1 \cdot B(W, Q^2)} - g_1^{data}(W, Q^2) \quad (5.1)$$

1684 with "std" shorthand used for "standard" model or the corresponding sim-
1685 ulation i.e. the ones provided by RCSLACPOL when the asymmetry A_1
1686 was not artificially increased to $A_1 + 0.1$. Here, Δn^{data} and Δn^{std} represent
1687 the polarized count differences for the experimental and simulated (without
1688 artificially changing A_1) data respectively.

Uncertainty from Polarized H in target and π^- contaminations This
contribution from polarized H in target and π^- contamination is evaluated as
follows,

$$\Delta g_1^{cont}(W, Q^2) = g_1^{std}(W, Q^2) + \frac{\Delta n^{data}(W, Q^2) \cdot 1.025 - \Delta n^{std}(W, Q^2)}{B(W, Q^2)} - g_1^{data}(W, Q^2) \quad (5.2)$$

1689 where we assume that the contamination is not more than 2.5%, which is
1690 consistent with what was found from our own study of the contamination.

Possible uncertainty in the beam energy measurement This contribution is evaluated assuming the uncertainty in beam energy measurement is not more than 10 MeV, so either the experimental data or the standard-simulation data can be analyzed assuming the beam energy was different by 10 MeV. In this analysis, the simulated data was analyzed assuming that the beam energy was 10 MeV more than that used during the event generation or simulation which was the same as that used for analyzing the experimental data. For example, for the lower beam energy data set, 1339 MeV was used to analyze the experimental data as well as to simulate the corresponding data, but during the analysis of the simulated data, the energy value used was 1349 MeV. Here, the change in energy results in changes in both Q^2 and W .

$$\Delta g_1^{Eb}(W, Q^2) = g_1^{std}(W, Q^2) + \frac{\Delta n_{E\bar{b}+}^{data}(W, Q^2) - \Delta n_{E\bar{b}+}^{std}(W, Q^2)}{B(W, Q^2)} - g_1^{data}(W, Q^2) \quad (5.3)$$

1691 where $\Delta n_{E\bar{b}+}^{std}$ is now the simulated Δn^{std} obtained by analyzing the data
1692 from the standard simulation as usual but with a beam energy that was 10
1693 MeV more than the standard value.

Possible uncertainty in the CC-inefficiency estimation This contribution is estimated by assuming a maximum of 50% uncertainty in the estimated inefficiency as follows: The the 50% error is justified because the uncertainty in inefficiency is no more than 50% for $nphe > 2.5$ (see Fig. 3.30).

$$\Delta g_1^{Eb}(W, Q^2) = g_1^{std}(W, Q^2) + \frac{\Delta n_{0.5CCi}^{data}(W, Q^2) - \Delta n_{0.5CCi}^{std}(W, Q^2)}{B(W, Q^2)} - g_1^{data}(W, Q^2) \quad (5.4)$$

1694 where $\Delta n_{0.5CCi}^{std}$ is now the simulated Δn^{std} obtained after applying 50% more
1695 inefficiency instead of the actually estimated value. This considers the worst
1696 case scenario of 50% inefficiency and evaluates the corresponding systematic
1697 uncertainty to be the deviation of the extracted quantity from the one that
1698 would be obtained when there were to be a 100% efficiency.

Possible uncertainty due to e^+e^- pair symmetric contamination The contribution due to e^+e^- pair symmetric contamination is calculated as fol-

lows:

$$\Delta g_1^{Eb}(W, Q^2) = g_1^{std} + \frac{\Delta n^{data} \cdot \frac{1}{1+f(e^+e^-)} - \Delta n^{std}}{B(W, Q^2)} - g_1^{data}(W, Q^2) \quad (5.5)$$

1699 where $f(e^+e^-)$ is the fraction of electrons in a given bin that come from pair-
 1700 symmetric e^+e^- produced as estimated with EG1b fit by N. Guler [22] (used
 1701 the closest available energies).

Radiative correction uncertainty Here, we need to change the parameter that most influences radiative corrections i.e., the number of radiation lengths before (RADB) and after (RADA) the scattering. By increasing both numbers by 10%, we should have a safe upper limit on practically all uncertainties coming from the radiative procedure itself. But, to simplify the situation, we increased the RADA parameter in RCSLACPOL by 20% and repeated the full-statistic simulation. As a result, this particular contribution to the systematic uncertainty in a given kinematic bin is calculated as:

$$\Delta g_1^{rad}(W, Q^2) = g_1^{std} + \frac{\Delta n^{data}(W, Q^2) - \Delta n^{rad}(W, Q^2)}{B(W, Q^2)} - g_1^{data}(W, Q^2) \quad (5.6)$$

1702 where the proportionality factor $B(W, Q^2)$ for the bin is exactly the same as
 1703 that used to calculate g_1 earlier.

1704 5.2 Model uncertainties

1705 The remaining four components in the total systematic uncertainty (the last
 1706 four in the list 5) account for the model uncertainty contributions. For this
 1707 purpose, we changed the values of two of the model parameters “Asym-
 1708 Choice” and “SFchoice” (each takes value of 11, in the standard case)

1709 We repeated the full statistics simulation four more times by changing
 1710 the values of two RCSLACPOL parameters “AsymChoice” and “SFchoice”
 1711 (which controls the values of model asymmetries and the structure functions,
 1712 with each taking a value of 11 in the standard case) one by one corresponding
 1713 to the following four model variations:

1714 1. Variation-1: AsymChoice=12, SFchoic=11

1715 2. Variation-2: AsymChoice=15, SFchoic=11

1716 3. Variation-3: AsymChoice=11, SFchoic=12

1717 4. Variation-4: AsymChoice=11, SFchoic=13

1718 where, the different values of the two RCSLACPOL parameters correspond
1719 to the following model choices:

1720 1. **AsymChoice** values are used to determine specific A_1/A_2 models used
1721 in the RCSLACPOL program

1722 (a) 11: Standard Resonance Model 2008-9 Guler/Kuhn (**Used for**
1723 **standard simulation**)

1724 (b) 12: Variation of A_1 model (earlier fit)

1725 (c) 15: Variation of A_2 resonance model: Vary the virtual photon
1726 asymmetry A_2 in the resonance region within its fit uncertainties.

1727 2. **SFchoice** values are used to determine specific F_1/F_2 models.

1728 (a) 11: 2009 version of $F_1^n/F_1^p/F_1^d$ by Peter Bosted/Eric Christie 2009,
1729 HERMES (**Used for standard simulation**) (with d in F_1^d de-
1730 noting a deuteron).

1731 (b) 12: Same version as 11, but with fit uncertainties added to F_2
1732 (and proportionally F_1)

1733 (c) 13: Same version as 11, but with fit uncertainties subtracted from
1734 R (F_2 unchanged)

After the simulation data for the above four cases (see 5.2) were available, four more data tables (TM1,TM2,TM3 and TM4) were produced for the corresponding model values of g_1 , A_1 , F_1 etc. Then, the contributions to the systematic uncertainty from each of these four cases of model variation were given as follows:

$$\Delta g_1^i(W, Q^2) = g_1^{std}(W, Q^2) + \frac{\Delta n^i(W, Q^2) - \Delta n^{std}(W, Q^2)}{B(W, Q^2)} - g_1^i(W, Q^2) \quad (5.7)$$

1735 with “i” indicating any of the four cases of model variation, g_1^i being the
1736 model prediction for the i^{th} case as obtained from the corresponding data
1737 table “TMi” and the proportionality factor $B(W, Q^2)$ again being exactly
1738 the same as used to calculate g_1 as earlier.

1739 5.3 Combining uncertainties

1740 Contributions from the 10 individual components are estimated and then a
 1741 total contribution is estimated by first combining the corresponding individ-
 1742 ual components for each of the two beam energies and finally combining them
 1743 all by calculating the RMS of the ten combined contributions.

1744 In principle, each of the individual contributions to the systematic uncer-
 1745 tainty can also be combined using the same equations as for combining g_1
 1746 and $A_1 F_1$ (see above). However, we must be careful to distinguish between
 1747 correlated and uncorrelated uncertainties. If for a given (W, Q^2) bin, data
 1748 is available only from one beam energy, then combined uncertainty for the
 1749 k^{th} component is simply the uncertainty from that beam energy. If there are
 1750 measurements from both beam energies, we combine them with statistical
 1751 weights as follows:

- 1752 1. The variations due to scale factor ($k=1$), beam energy ($k=3$) and CC-
 1753 efficiency ($k=4$) are all un-correlated and, therefore, added in quadra-
 1754 ture as follows:

$$\delta g_1(k=8,10,11, \text{ combined}) = \sqrt{\left(\sum_i \frac{(\delta g_1)^2(i)}{(\Delta g_1)^2(i)} \right) / \text{Sum2}} \quad (5.8)$$

1755 where, δ represents the k^{th} component of the systematic uncertainty,
 1756 whereas, 'Sum2', 'i' and Δ have the same meanings as before, with
 1757 'Sum2' given by

$$\text{Sum2} = \sum_i \frac{1}{(\Delta g_1)^2(i)} \quad (5.9)$$

1758 which provides the statistical weight, where the index 'i' represents
 1759 two beam energy (1.3 and 2.0 GeV) data sets, and Δg_1 indicates the
 1760 statistical uncertainty in g_1 in the corresponding kinematic bin.

- 1761 2. All other variations are correlated between the two beam energies and
 1762 should be averaged linearly (WITH sign):

$$\delta g_1(\text{other } k, \text{ combined}) = \left(\sum_i \frac{(\delta g_1)(i)}{(\Delta g_1)^2(i)} \right) / \text{Sum2} \quad (5.10)$$

Once each of the k^{th} component of the systematic uncertainties are combined between the two beam energies, we then proceed to combine them all to get a grand total. This is done by simply adding the ten E_b -combined systematic uncertainties in quadrature and taking the square-root of the sum as follows:

$$TotalSystematicUncertainty = \sqrt{\sum_{k=1}^{10} (\Delta g_1)_k^2} \quad (5.11)$$

Figs. (5.2 and 5.3) show, for example, the different components of the systematic uncertainties along with the grand total on g_1 (from 1.3 GeV data) evaluated in the manner just outlined. Likewise, Figs. (5.4 and 5.5) show similar plots for the 2.0 GeV data.

These ten different components of systematic uncertainties on g_1 and similarly on $A_1 F_1$ thus calculated separately for both beam energies are later combined as described below.

5.3.1 Combining data from the two beam energies

Once the data g_1 and $A_1 F_1$ and their corresponding uncertainties are evaluated from each beam energy data set, they are combined as follows [26] (to make the description simple, the procedure is described only for g_1 , but, in the end, the exact same procedure is followed for $A_1 F_1$ as well):

1. First a table is made, separately for each beam energy, of all (Q^2, W) bins with calculated values of g_1 , their statistical uncertainties and each of the ten components of the systematic uncertainties (making sure to keep the correct signs of the systematic changes).
2. Then another table is made for the combined values of g_1 , which are evaluated as follows:
 - (a) If for a given (W, Q^2) bin, g_1 comes only from one beam energy, then all the entries from that energy go into the "combined" table
 - (b) If g_1 has measurements from both beam energies, we combine them with statistical weights as follows:

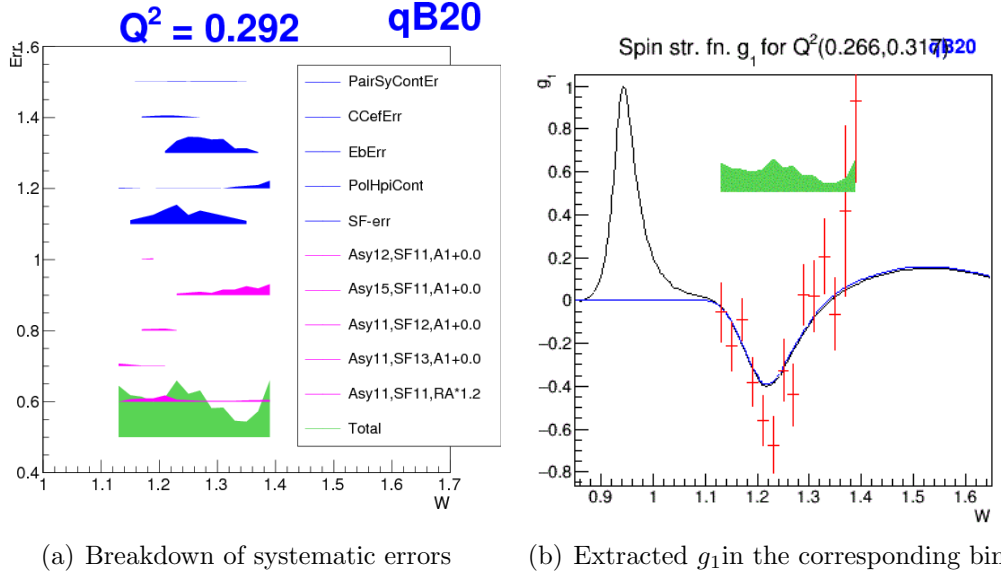


Figure 5.1: On the left: various components of systematic uncertainty (see Sec. 5 on g_1 vs W in a Q^2 bin (1.3 GeV data). The band width represents the size of the uncertainties. The vertical position of each band has no physical meaning (arbitrarily chosen for the convenience of display). The first five (blue) bands are the contributions due to e^+e^- -contamination , CC-inefficiency , uncertainties in beam energy measurement , polarized background (H, π^- etc) and scaling factor uncertainties respectively. The first (top) magenta band is the contribution due to the uncertainties in the radiative corrections , next four (magenta) are due to model uncertainties and the last (green) one is the total uncertainty after properly combining all components. For similar plots in other Q^2 bins see Figs. 5.2 and 5.3. On the right: extracted g_1 vs W shown along with the total systematic uncertainty.

$$Sum1 = \sum_i \frac{g_1(i)}{(\Delta g_1)^2(i)} \quad (5.12)$$

$$g_1(combined) = Sum1/Sum2 \quad (5.13)$$

$$\sigma g_1(combined) = \sqrt{1/Sum2} \quad (5.14)$$

1790 where the index 'i' represents two beam energy (1.3 and 2.0 GeV)
 1791 data sets, Δg_1 indicates the statistical uncertainty in g_1 and $Sum2$
 1792 is again given by Eq. 5.12 above.

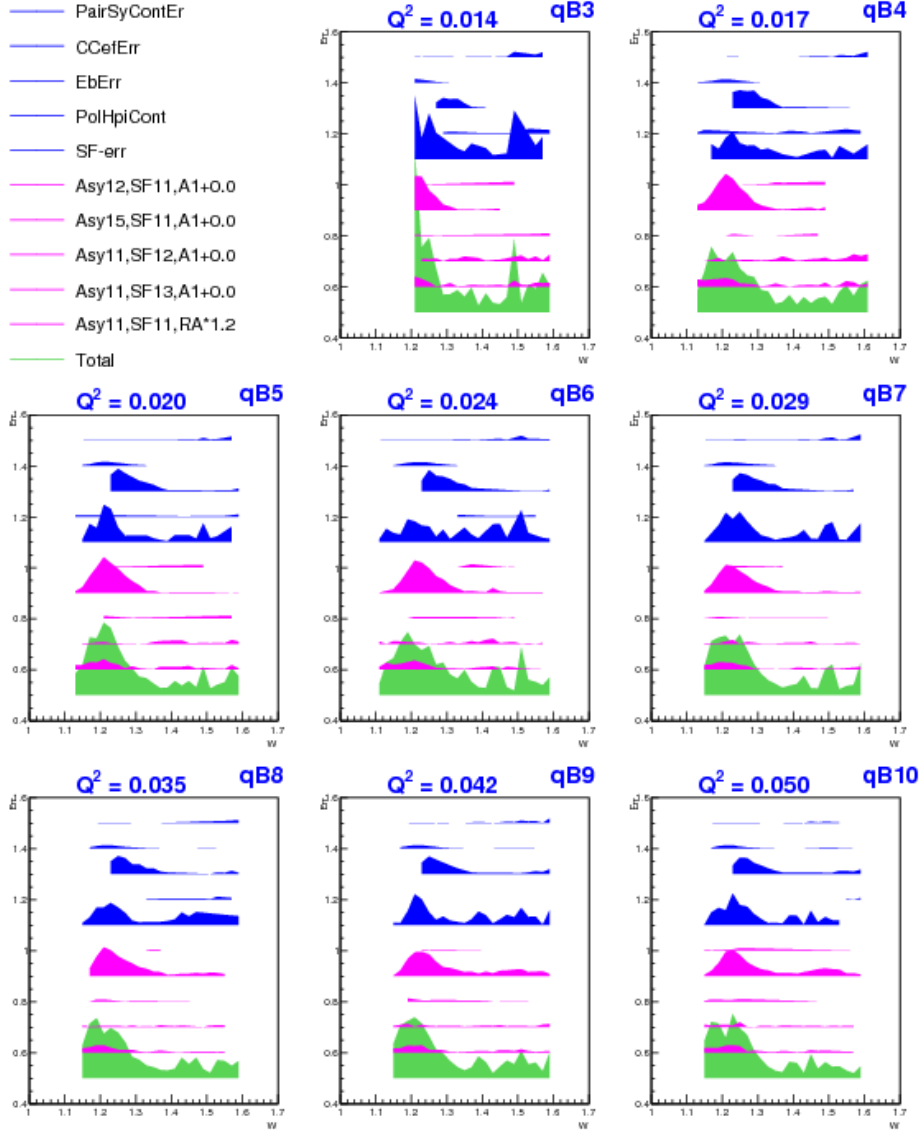


Figure 5.2: Plots like that shown in Fig. 5.1 showing various components of systematic uncertainty on g_1 vs W in different Q^2 bins for 1.3 GeV data.

1793 Figures 5.6 and 5.8 show the breakdown of the total contribution to the
 1794 systematic uncertainty from different sources. We can see that the dominant
 1795 contribution comes from the uncertainties in the overall scale factor (the cyan
 1796 band indicated with SF-err in the legend) which is used to normalize the sim-

ulated data to make them comparable with data. One of the big part of this uncertainty comes from those in $P_b P_t$ and target size measurements. Next big contributions seem to come from the model (in particular the model for the unmeasured A_2) and radiative corrections. Near the Δ -resonance region, the effect of beam energy uncertainty also seems to be very pronounced. The breakdown of the different components (but combined between the two beam energies) of the total systematic uncertainties are also shown separately in the Figs. 5.6 and 5.8.

It should be noted here that the same methods were used to calculate the systematic uncertainties on $A_1 F_1$ and on all integrals directly (i.e., they are not calculated from propagated systematic uncertainties on g_1 or $A_1 F_1$ but directly from variations of the integrals.

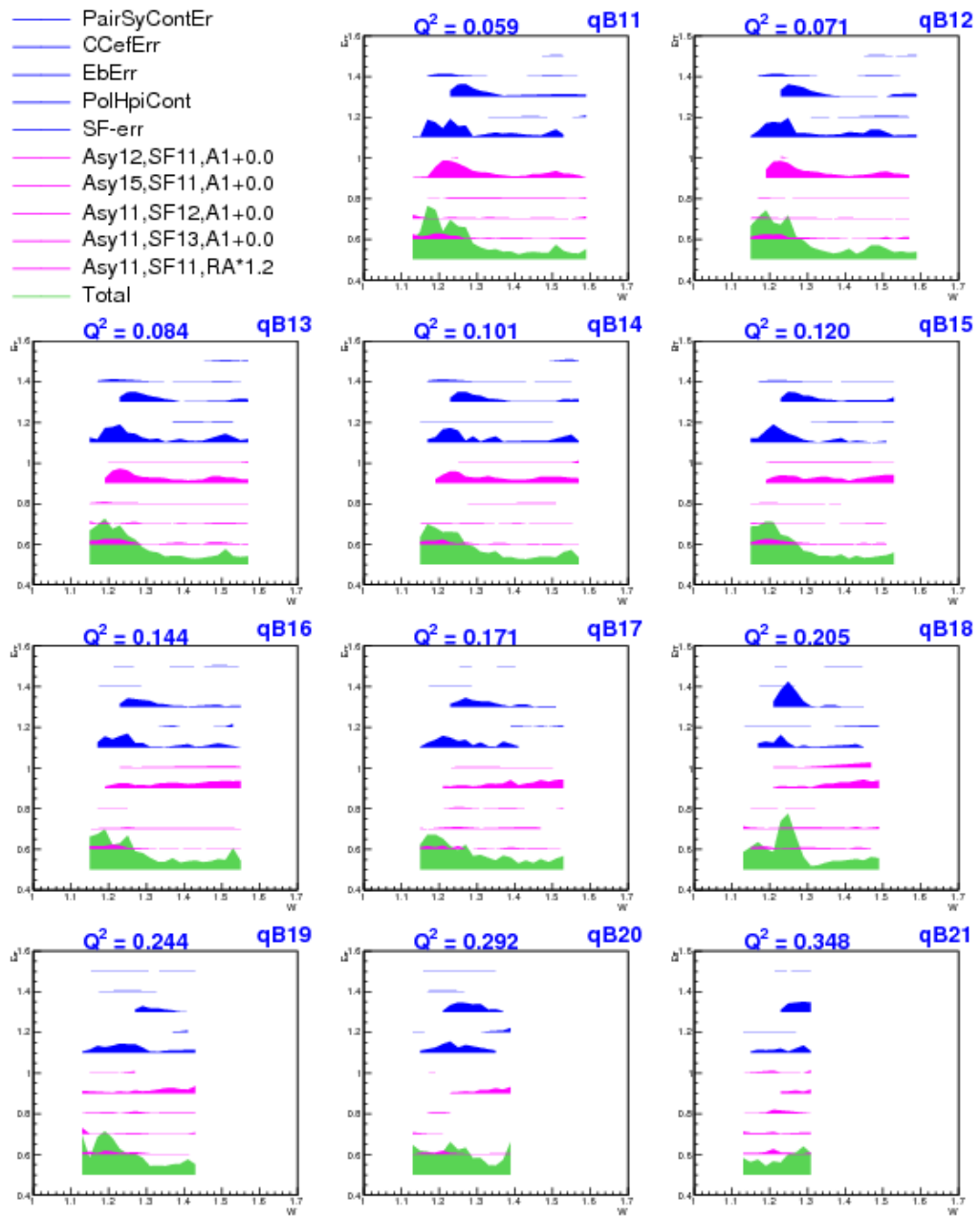


Figure 5.3: Systematic uncertainty components in remaining Q^2 bins (continuation of Fig. 5.2).

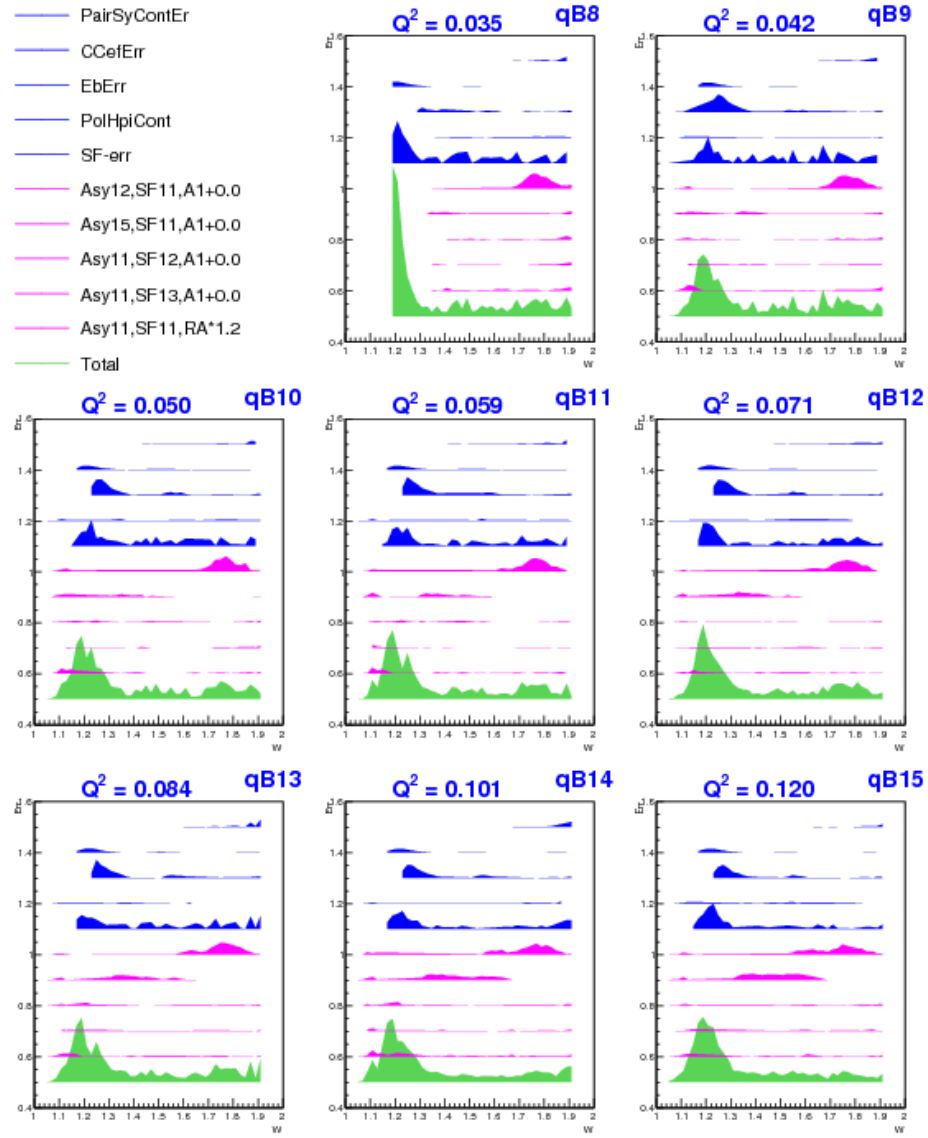


Figure 5.4: Plots similar to those shown in Fig. 5.2 but for 2.0 GeV, showing various components of systematic uncertainty on g_1 vs W in different Q^2 bins.

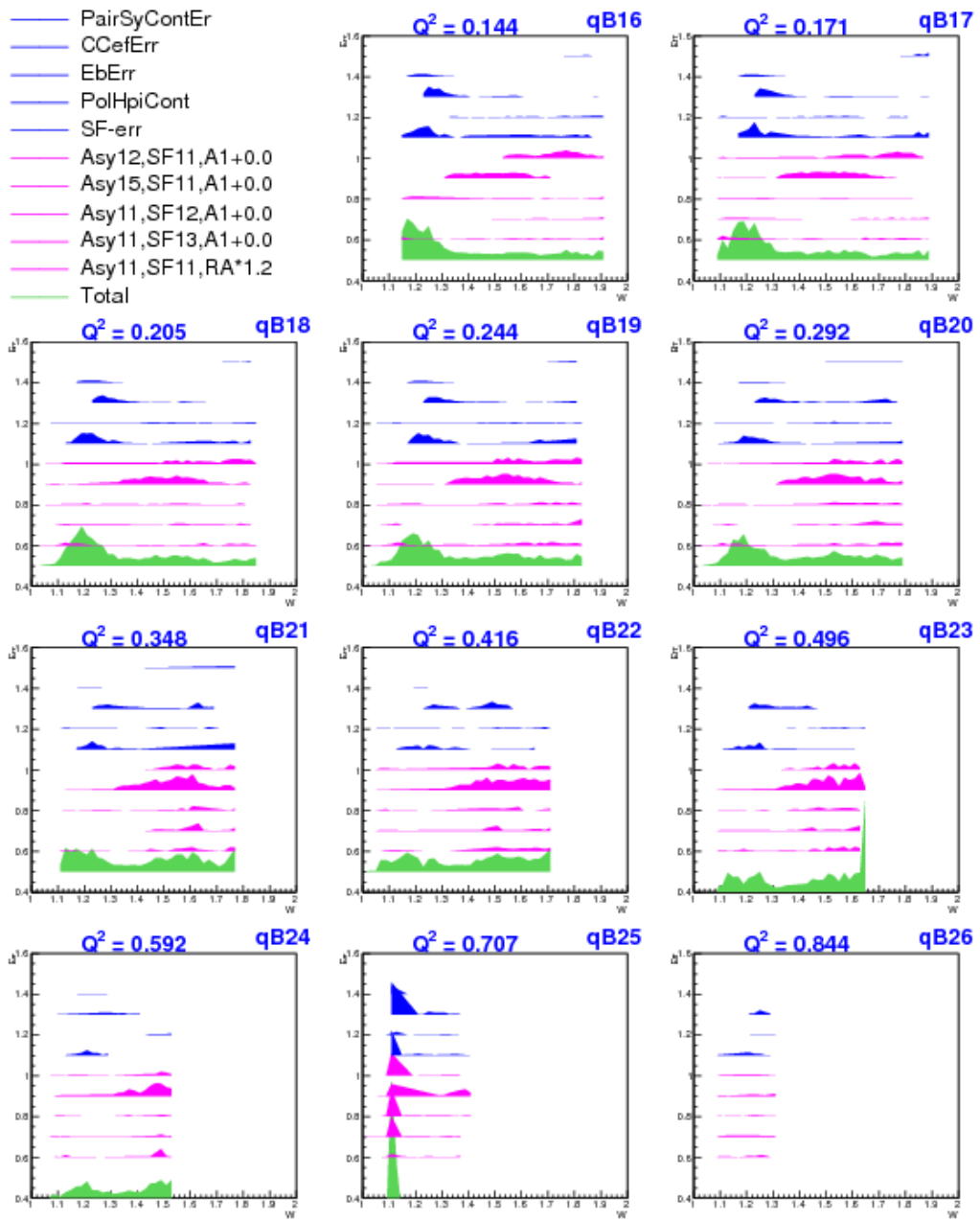


Figure 5.5: Systematic uncertainty components in remaining Q^2 bins (continuation of Fig. 5.4).

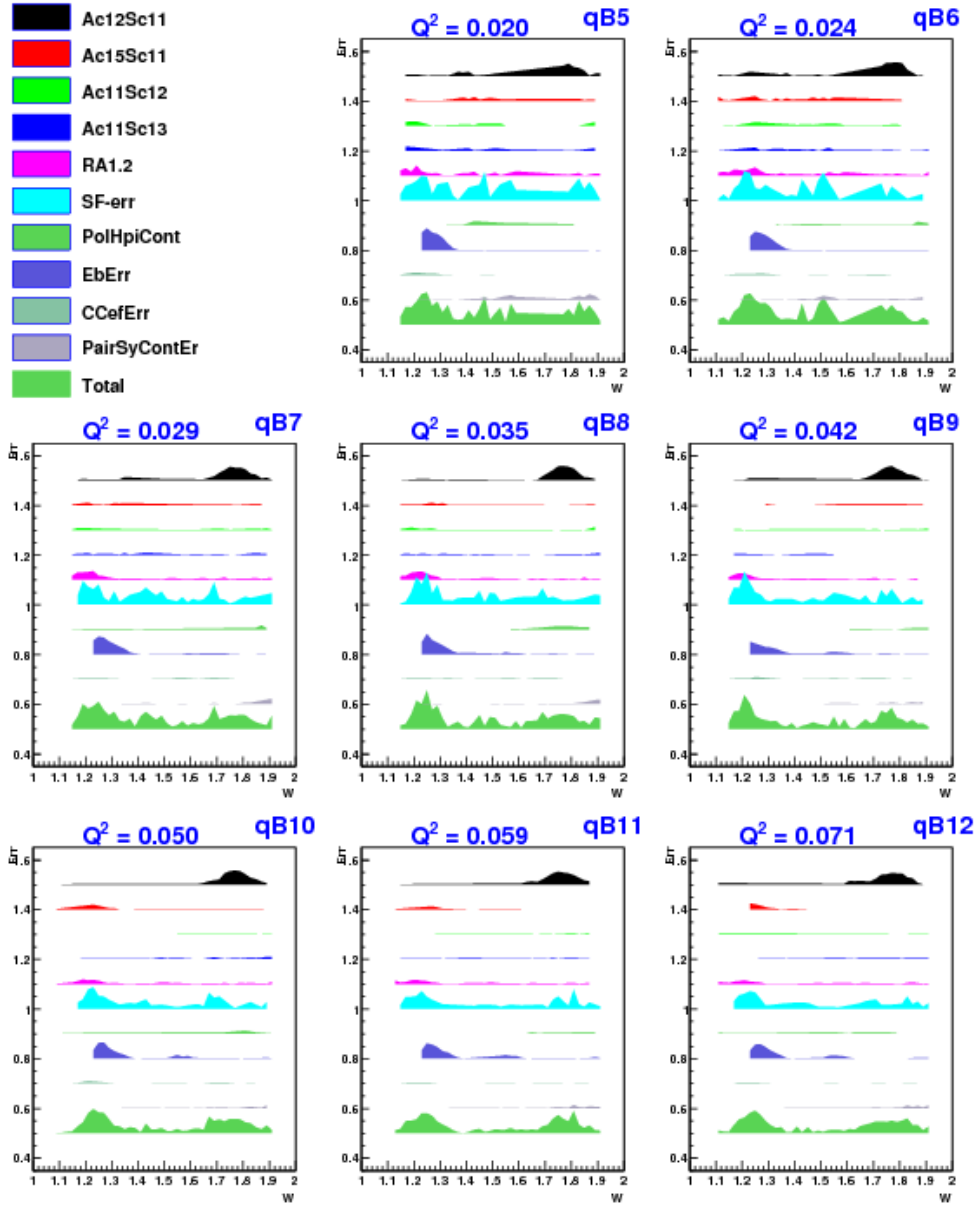


Figure 5.6: Breakdown of systematic uncertainties in g_1 (after combining data from the two energy data sets) in the first few Q^2 bins. See Fig. 5.1 for the description of the different systematic uncertainty components.

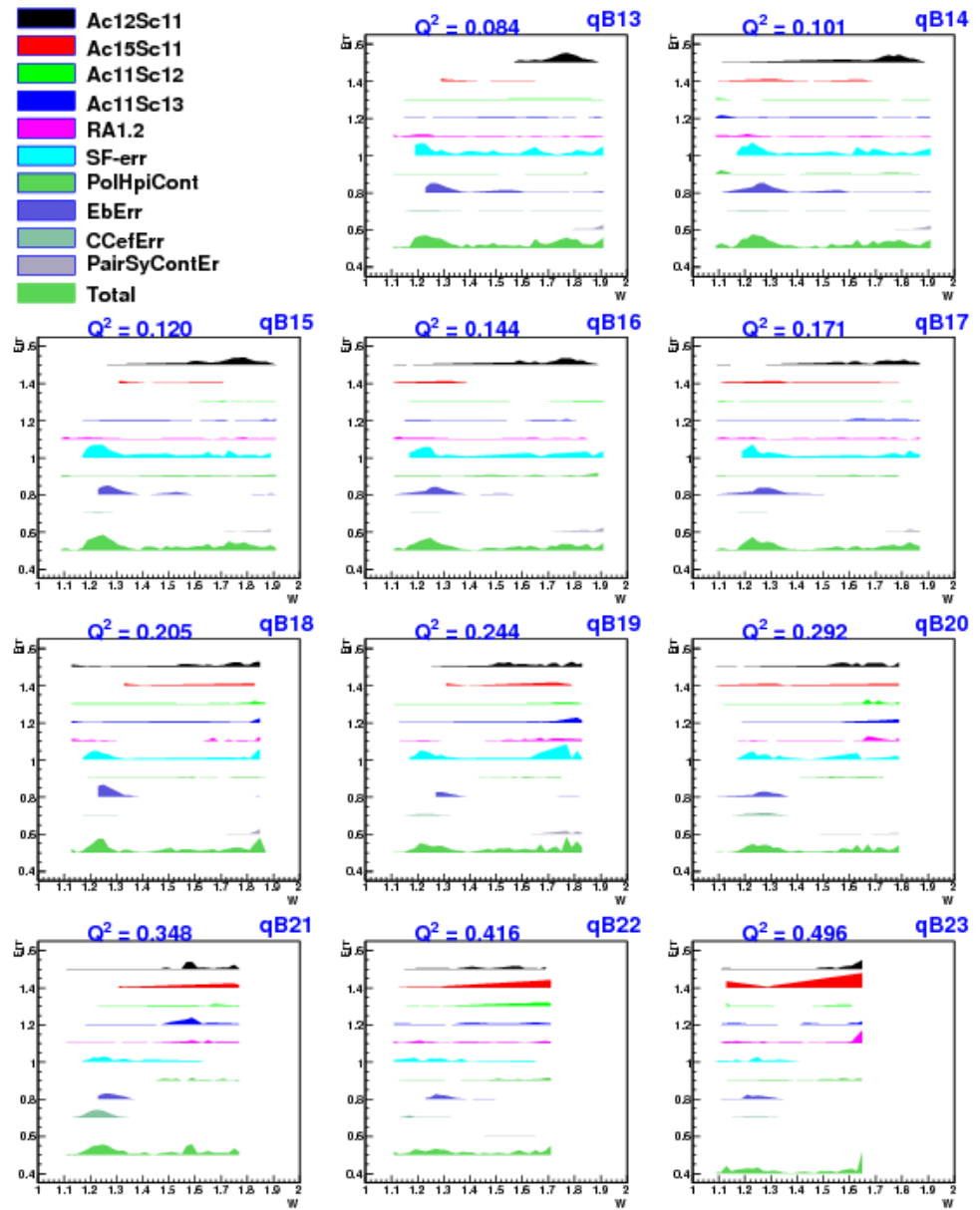


Figure 5.7: Plots as in Fig. 5.6 but in the remaining higher Q^2 bins.

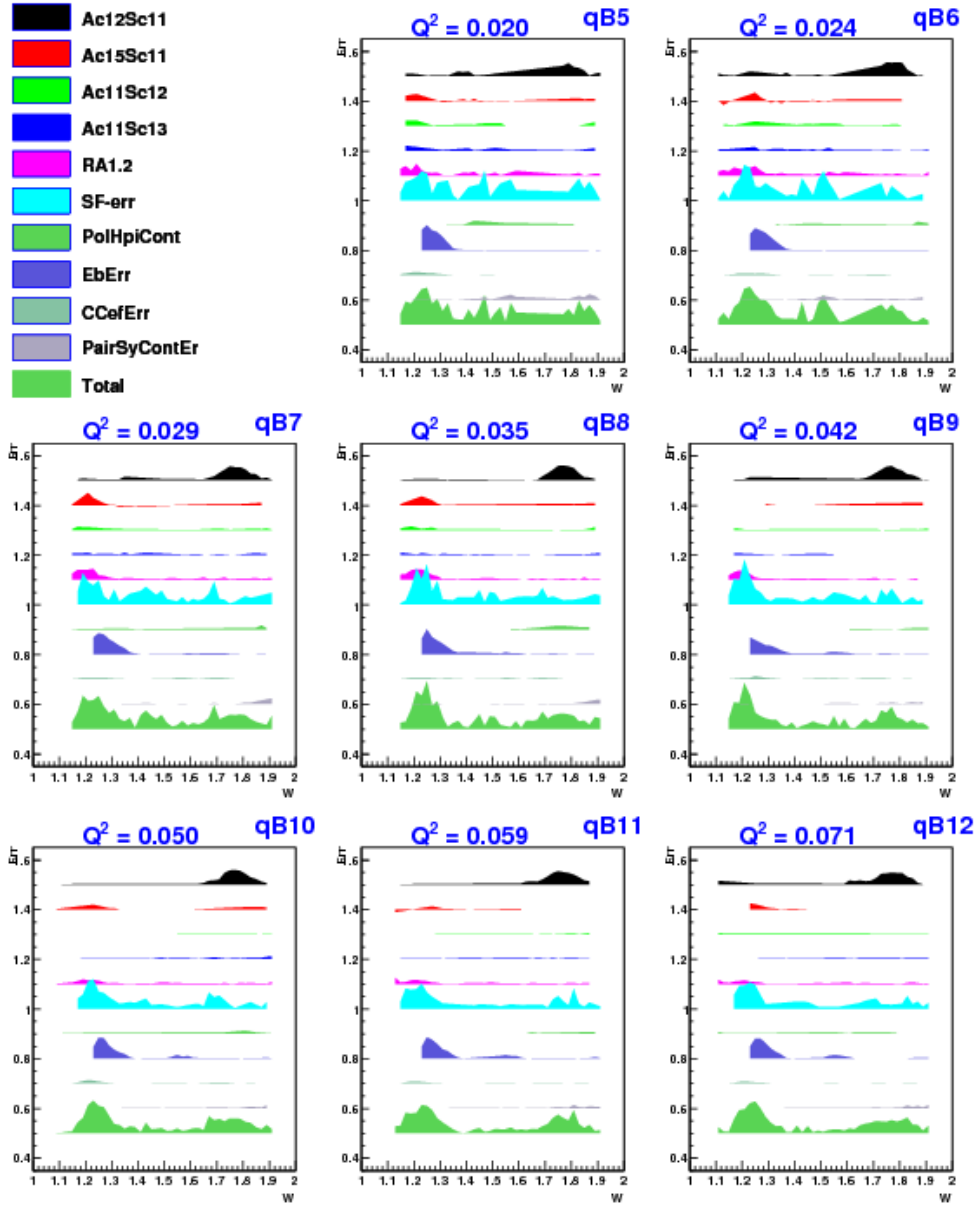


Figure 5.8: Breakdown of systematic uncertainties in $A_1 F_1$ (after combining data from the two energy data sets) in the first few Q^2 bins. See Fig. 5.1 for the description of the different systematic uncertainty components.

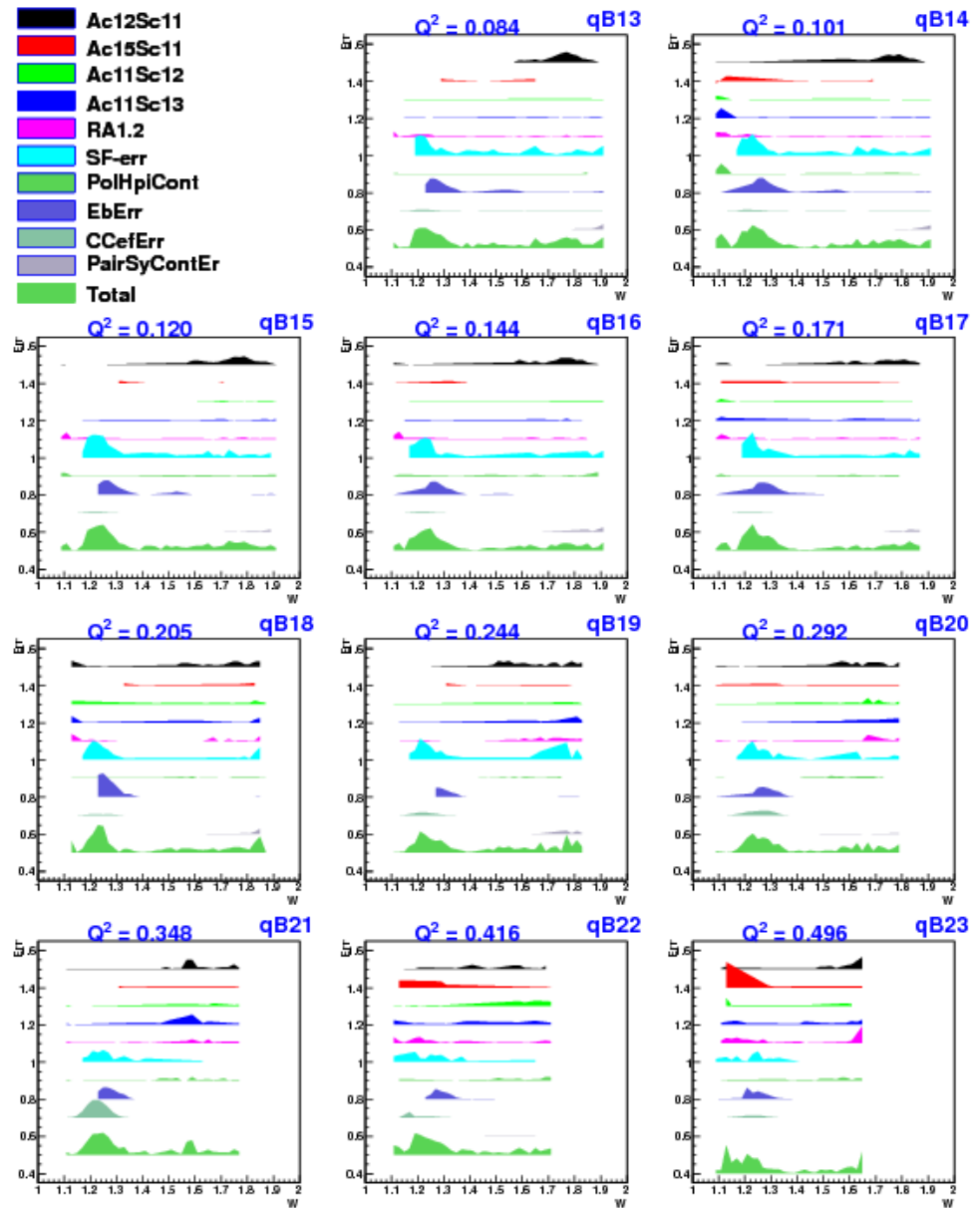


Figure 5.9: Plots as in Fig. 5.8 but in the remaining higher Q^2 bins.

1809 **Chapter 6**

1810 **Results**

1811 Two quantities - g_1 and $A_1 F_1$ and their uncertainties were extracted from the
1812 EG4 deuteron target data using the methods outlined in the previous chapter.
1813 This was done in each of 21 Q^2 bins (between about 0.02 and 0.7 GeV 2 in
1814 Q^2) and several W bins of size 20 MeV each. In the overlapping kinematic
1815 bins where both beam energy data sets contributed, the results were further
1816 combined individually to arrive at a single set of energy independent data
1817 points. Finally, within each Q^2 bin, the newly extracted g_1 and $A_1 F_1$ values
1818 were used to evaluate three different integrals - Γ_1^d , \bar{I}_{TT} , and γ_0^d . All of these
1819 results are presented in the sections below.

1820 **6.1 Extracted g_1 and $A_1 F_1$**

1821 Figures 6.1 and 6.2 show the extracted values of g_1 and their errors from
1822 two different beam energies (1.337 GeV and 1.989 GeV). It can be seen that
1823 the two energies give results that are in good agreement in the overlapping
1824 kinematic regions.

1825 These results from low Q^2 measurements clearly show the resonant struc-
1826 ture in the region $W \leq 2.0$. Especially, the Δ -resonance stands out through
1827 its strongly negative signal. In addition, in the second resonance region
1828 around $W=1.5$ GeV where $N^*(1520)$ and $N^*(1535)$ (also denoted by D_{11}
1829 and S_{13} respectively) overlap, we see a drastic transition of g_1 (or cross sec-
1830 tion) from strongly negative values (not well described by the model because
1831 it is unconstrained there due to the lack of experimental data) at low Q^2
1832 to clearly positive values at high Q^2 indicating that the dominance of the

1833 spin-flip helicity amplitude $A_{\frac{3}{2}}^T$ on cross section drastically diminishes with
 1834 Q^2 and the non-flip amplitude $A_{\frac{1}{2}}^T$ becomes stronger¹. We have pushed the
 1835 lower limit on Q^2 in the resonance region with reduced systematic and sta-
 1836 tistical errors that will contribute greatly to the world data set. Our data
 1837 will help MAID and other phenomenological models to better constrain their
 1838 parameters enabling them to make better predictions in the future.

¹The four virtual photoabsorption cross sections σ_T , σ_L , σ_{LT} , and σ_{TT} , are related to the four structure functions F_1 , F_2 , g_1 and g_2 of the target and as a result, g_1 can be expressed as $g_1 = \frac{MK}{8\pi^2\alpha(1+\gamma^2)}(\sigma_{\frac{1}{2}}^T - \sigma_{\frac{3}{2}}^T + 2\gamma\sigma_{LT})$

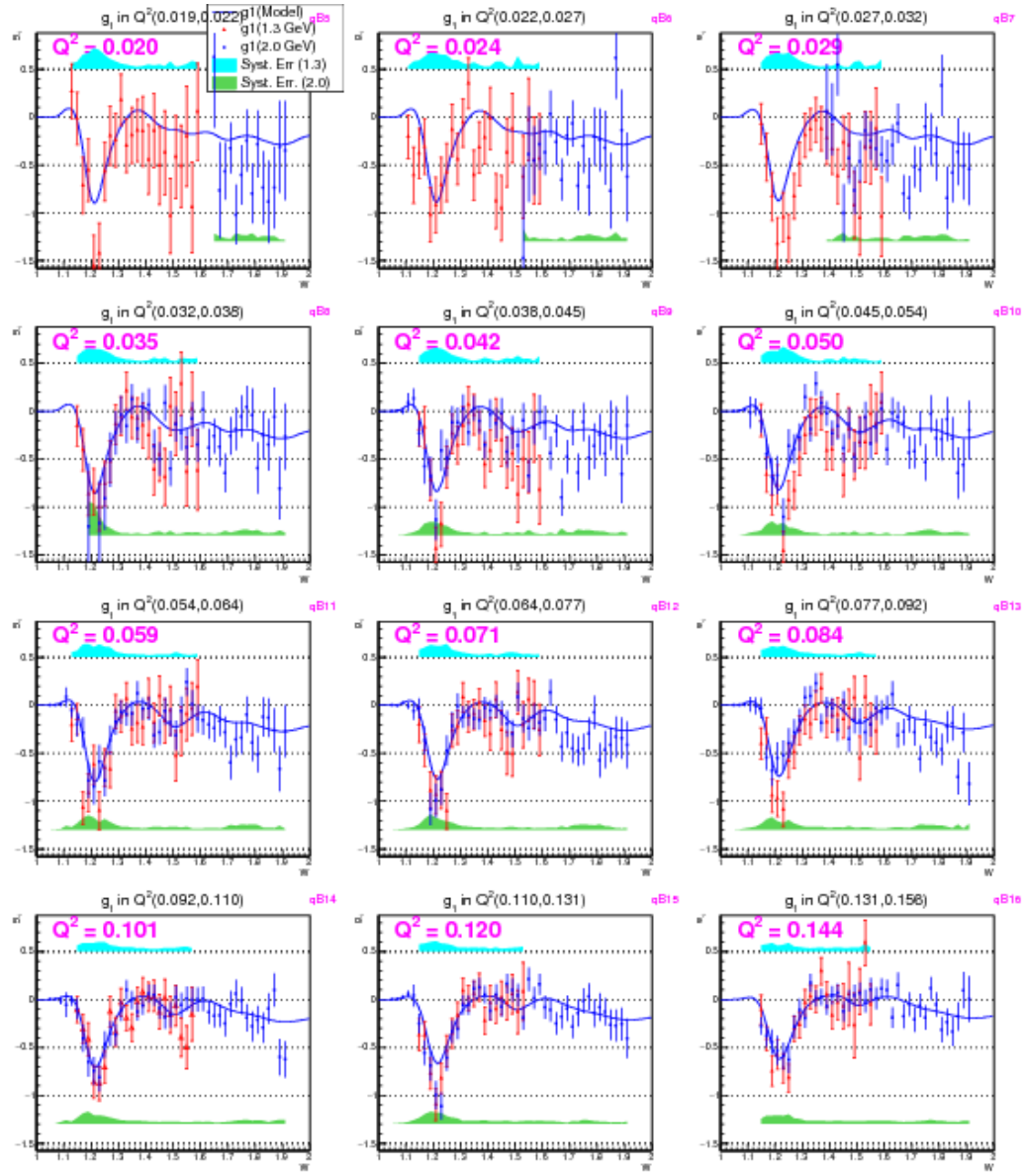


Figure 6.1: Extracted g_1 for deuteron (in the first 12 Q^2 bins) from the two different beam energy data sets. The statistical errors are indicated by error bars, while the systematic uncertainties are given by the bands (cyan, top: 1.3 GeV and green, bottom: 2 GeV).

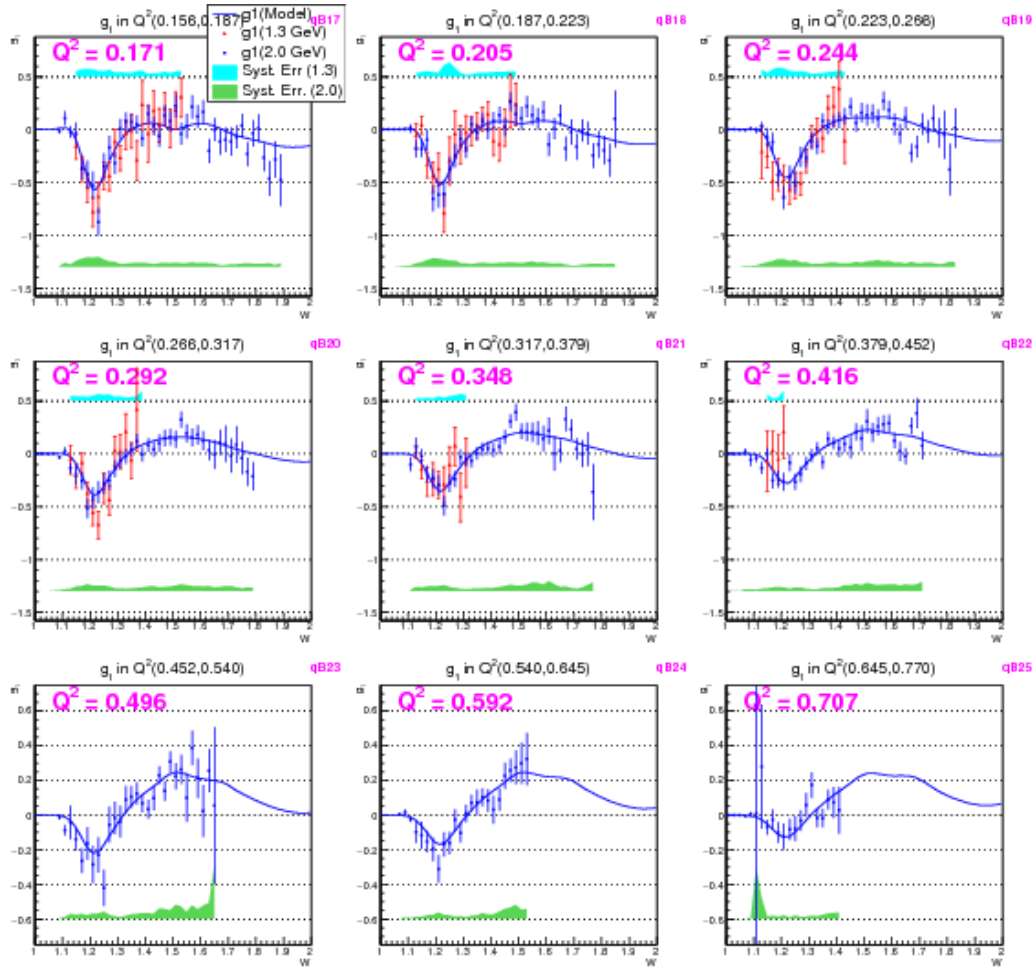


Figure 6.2: Extracted g_1 for deuteron (in the last 9 Q^2 bins (see Fig. 6.1 for the first 12 bins)) from the two different beam energy data sets.

Likewise, Figs. 6.3 and 6.4 shows the extracted values of $A_1 F_1$ and their errors from two different beam energies (1.3 GeV and 2.0 GeV). These values also show similar behavior as g_1 .

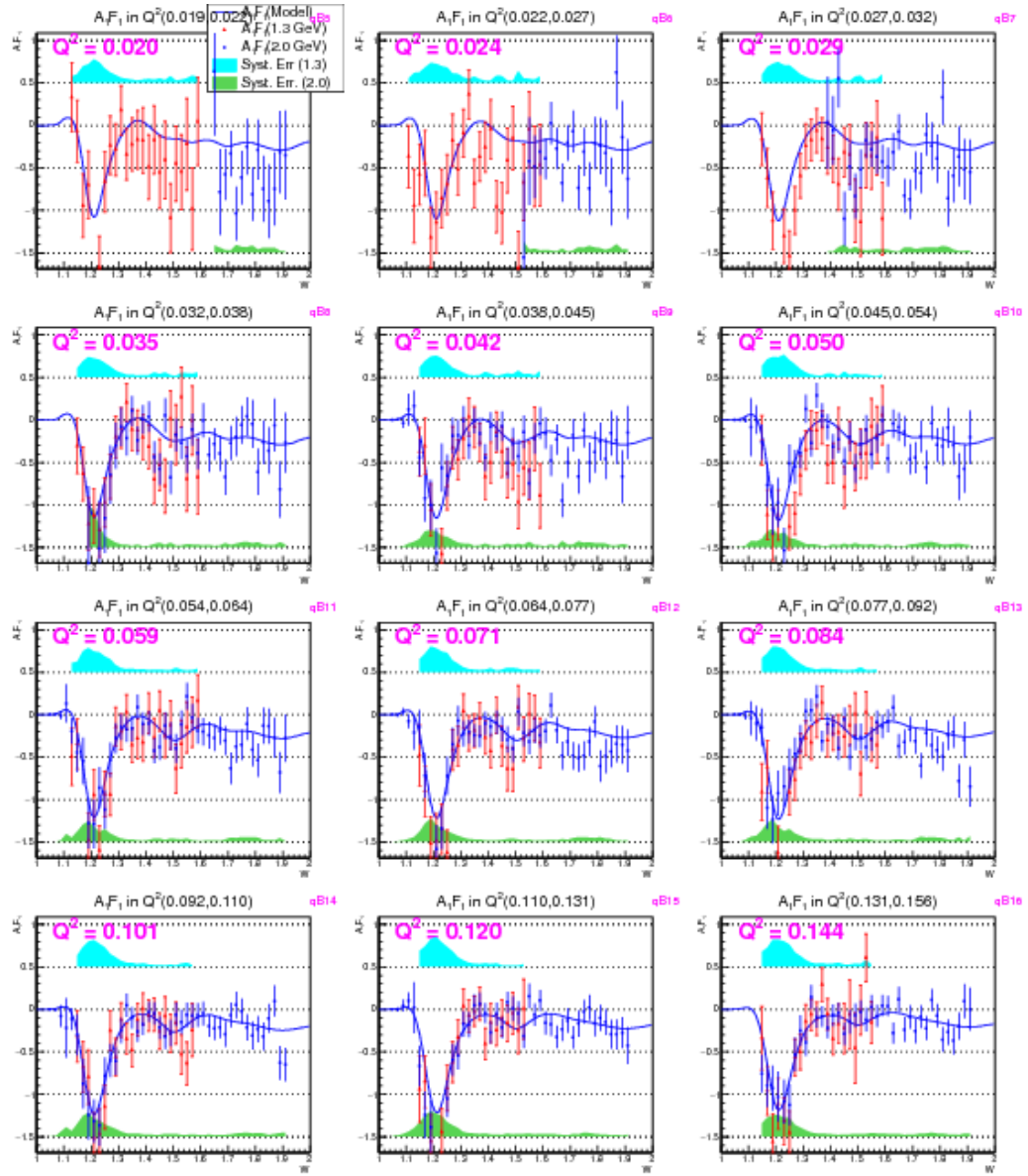


Figure 6.3: Extracted $A_1 F_1$ for deuteron (in the first 12 Q^2 bins) from the two different beam energy data sets. The statistical errors are indicated by error bars, while the systematic uncertainties are given by the bands (cyan, top: 1.3 GeV and green, bottom: 2 GeV).

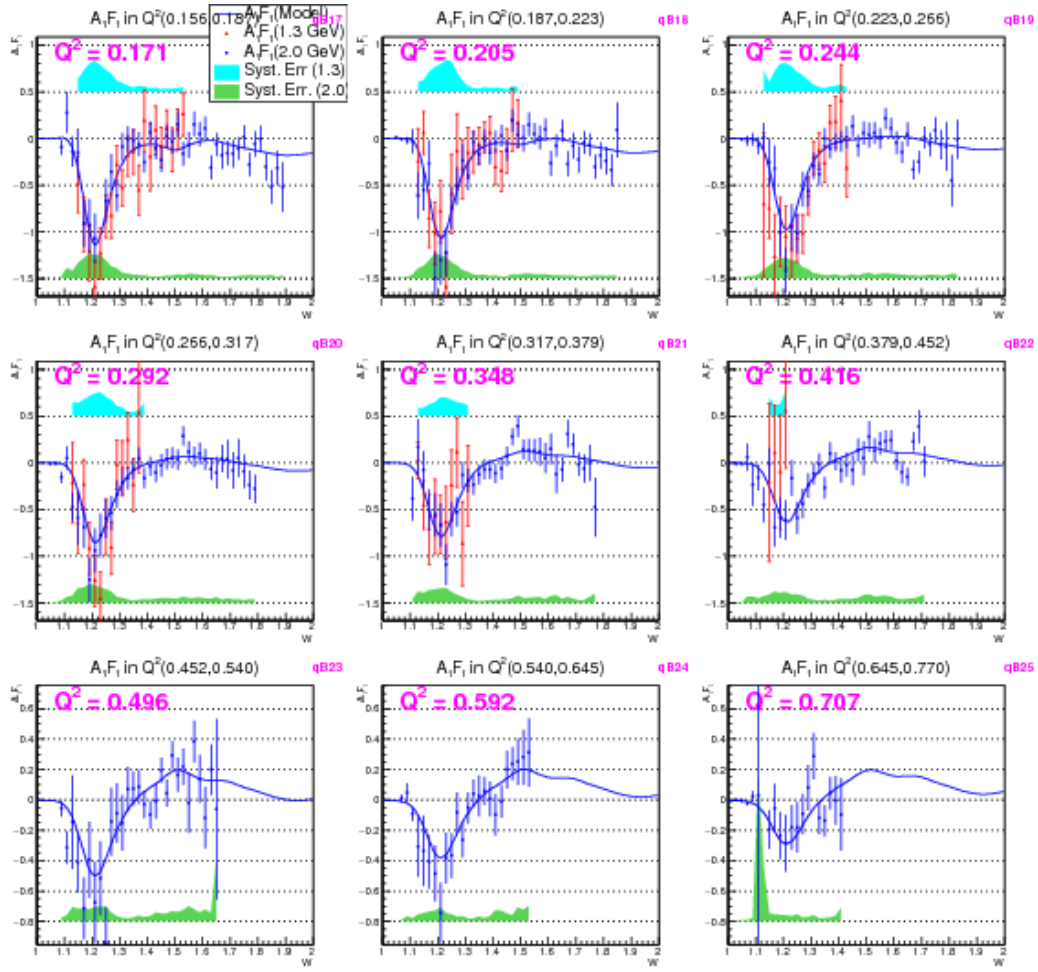


Figure 6.4: Extracted $A_1 F_1$ for deuteron (in the last 9 Q^2 bins (see Fig. 6.3 for the first 12 bins)) from the two different beam energy data sets..

1842 Figs. 6.5, 6.6, 6.7 and 6.8 show the values of g_1 and $A_1 F_1$ and their
 1843 errors after combining the corresponding results from the two different beam
 1844 energies as described in the previous chapter.

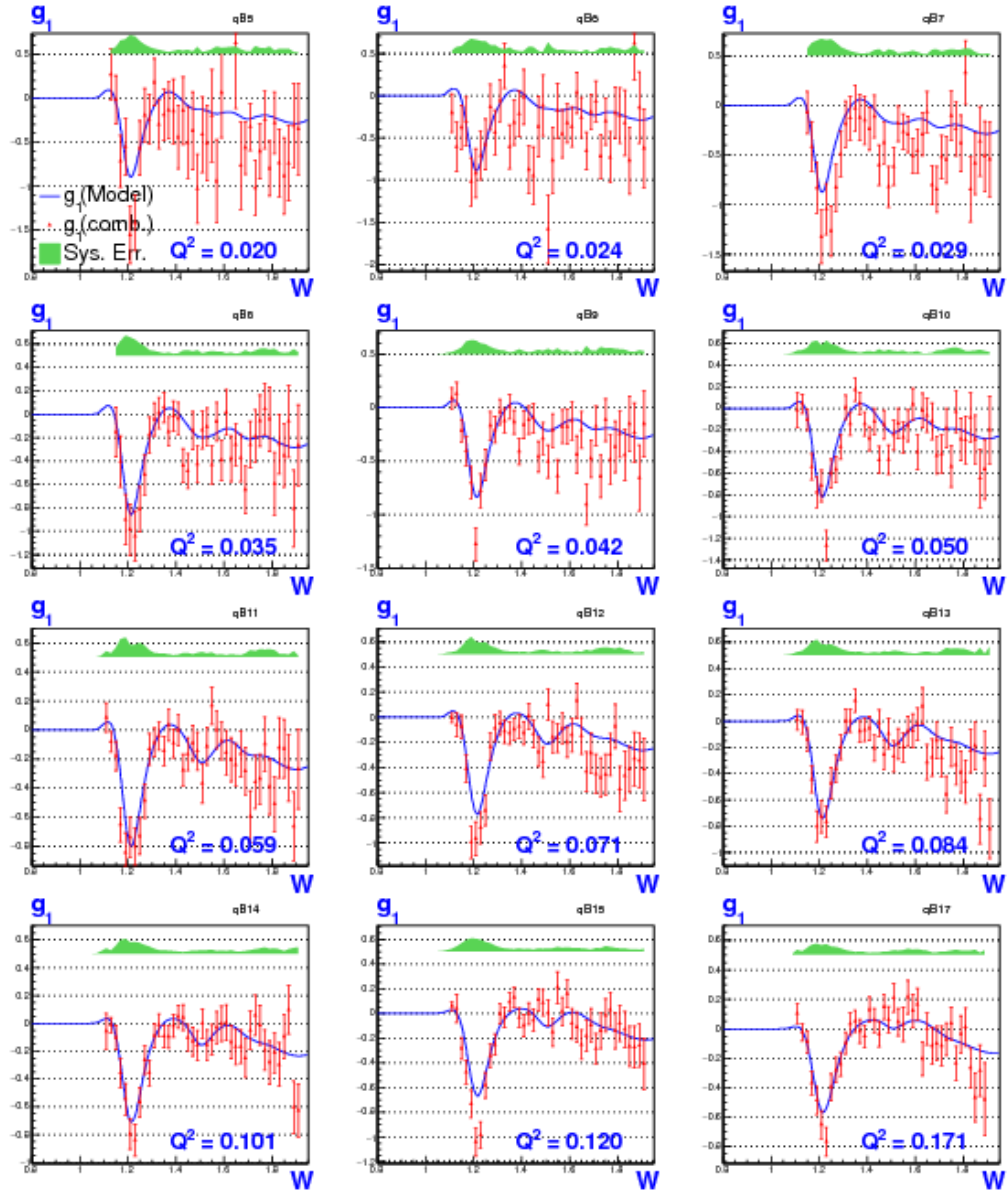


Figure 6.5: Extracted g_1 for deuteron after combining the results from the two beam energies (in the first 12 Q^2 bins). The red data points with error bars in each of the panels are the combined extracted results, the blue continuous line is the used model of g_1 and the green band represents the corresponding total systematic errors.

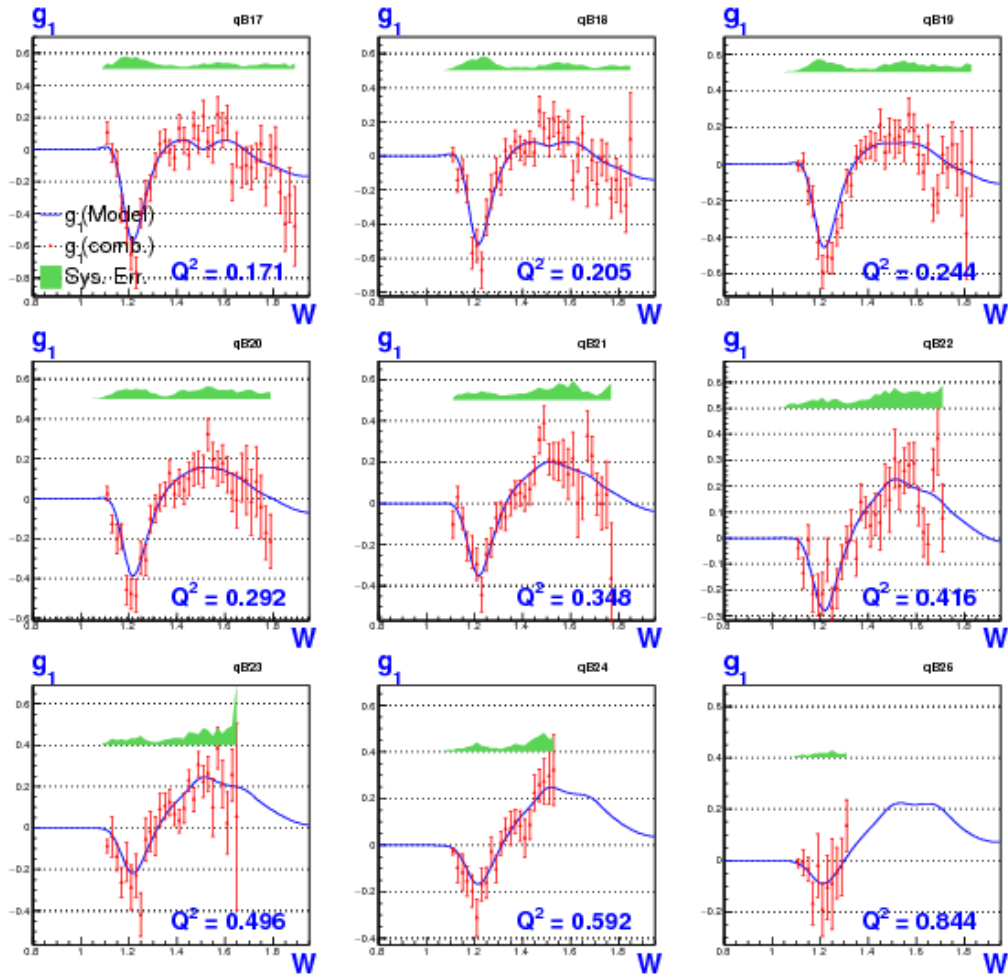


Figure 6.6: Similar plots as in Fig. 6.5 showing the combined results on g_1 in the next 9 Q^2 bins.

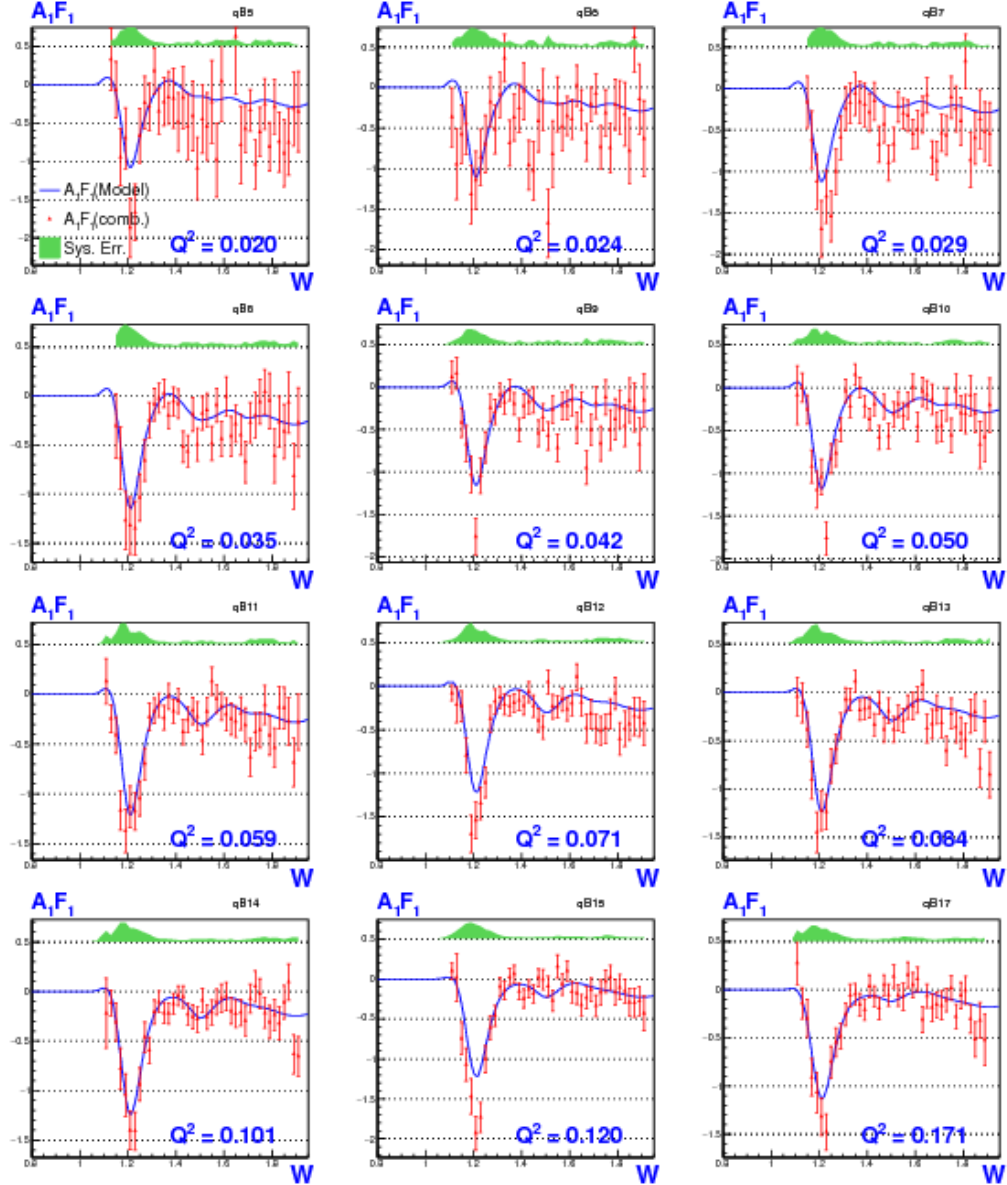


Figure 6.7: $A_1 F_1$ after combining the results from the two beam energies (in the first 12 Q^2 bins). The red data points with error bars in each of the panels are the combined extracted results, the blue continuous line is the used model of g_1 and the green band represents the corresponding total systematic errors.

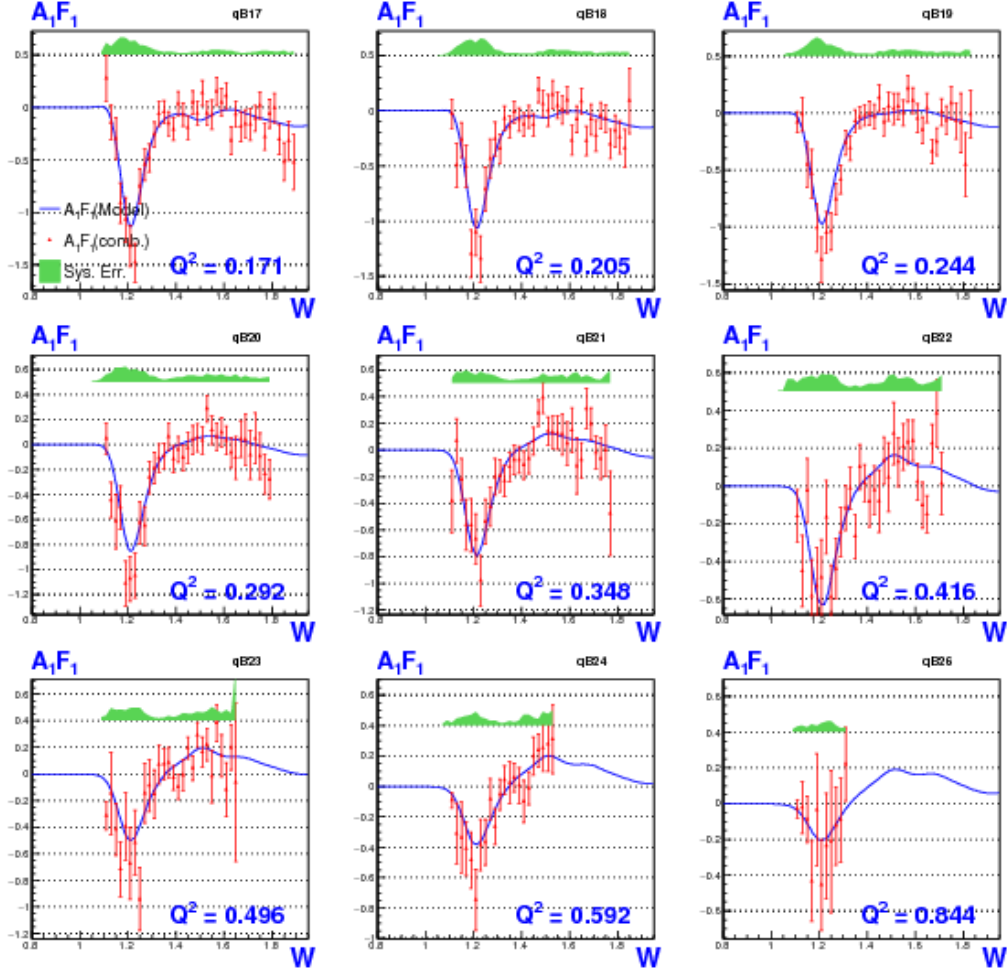


Figure 6.8: Similar plots as in Fig. 6.7 showing the combined results on g_1 in the next 9 Q^2 bins.

1845 **6.2 Moments of Deuteron Spin Structure func-**
 1846 **tions**

1847 Using the measured values of g_1 and A_1F_1 , three integrals were evaluated for
 1848 each of the Q^2 bins in which these data were measured. These integrals have
 1849 been calculated in two ways - using only the new EG4 measurements, and
 1850 adding model contributions to the data for regions not covered by our mea-

1851 surements. The integrals with the model contributions were calculated from
 1852 $x = 0.001$ to the onset of the resonance region (i.e. to the pion production
 1853 threshold of $W \approx 1.08$ GeV), dividing the sum into three parts for each Q^2
 1854 bin. For example, Γ_1 was evaluated by adding up the product $g_1 \Delta x$ over the
 1855 following three kinematic regions:

$$\Gamma_1(Q^2) = \int_{x=0.001}^{x(W_{data})} g_1(x, Q^2) dx \quad \text{model} \quad (6.1)$$

$$+ \int_{x(W_{data})}^{W=1.15} g_1(x, Q^2) dx \quad \text{data (or model for gaps)} \quad (6.2)$$

$$+ \int_{W=1.15}^{W=1.08} g_1(x, Q^2) dx \quad \text{model} \quad (6.3)$$

1856 where W_{data} indicates the upper edge of the last W bin in which the EG4
 1857 data is available in a given Q^2 bin (the W variable was divided into 70 bins
 1858 of size 20 MeV in the range $W=(0.7,2.1)$ GeV). The first part of the integral
 1859 as given by Eq. 6.1 is evaluated by using the model values of g_1 and using
 1860 Δx corresponding to a W bin of size 10.0 MeV. The ΔW is converted to Δx
 1861 by using $x = Q^2/(Q^2 + W^2 - M^2)$ to evaluate x at the two edges of each W
 1862 bin and taking the difference as follows:

$$\Delta x = x_{High} - x_{Low} = \frac{Q^2}{Q^2 + W_{High}^2 - M^2} - \frac{Q^2}{Q^2 + W_{Low}^2 - M^2} \quad (6.4)$$

1863 The second part given by Eq. 6.2 is evaluated similarly but using the EG4
 1864 results for g_1 if there is no measurement gap in between. If there is any gap,
 1865 the same method as in the first part is used to get a model contribution for the
 1866 gap and added to the data contribution. Lastly, the the third contribution
 1867 given by Eq. 6.2 again were evaluated from from model values (quasi-elastic
 1868 part turned off from the model in all of these cases) but with finer W bins
 1869 (1 MeV) because the integrals are very sensitive to the region near the Δ
 1870 resonance due to the fact that the structure functions show rapid changes
 1871 in this region. The reason to calculate the third integral using model values
 1872 rather than data values is to avoid having contributions in the integrals from
 1873 the quasi-elastic contamination.

1874 The statistical errors are evaluated by adding the statistical error con-
 1875 tribution in each W or x bin in quadrature. For example, if the integral is
 1876 evaluated in a Q^2 bin by calculating the sum $\left(\sum_{W \text{ bins}} g_1 \cdot \Delta x \right)$, then the cor-

1877 responding statistical error is evaluated by calculating $\sqrt{\sum_{W \text{ bins}} (\sigma g_1)^2 \cdot \Delta x}$.

1878 Because the model contribution is assumed to have no statistical uncertainties,
1879 the statistical errors in the integrals come solely from the propagation
1880 of the statistical error of the measured g_1 or $A_1 F_1$.

1881 The other two integrals and their errors are evaluated in the same manner,
1882 with g_1 replaced by their corresponding integrands and again calculating the
1883 three parts of the integrals separately.

1884 These integrals are then compared with the latest available predictions
1885 from different theories (mainly χ PT) and phenomenological calculations along
1886 with EG1b or DIS data whenever applicable.

1887 6.2.1 First moment of g_1 (Γ_1)

1888 The first integral of interest is the first moment of g_1 i.e., Γ_1 (see Eq. 1.10)
1889 , which was calculated for all Q^2 bins for which the new data are available.
1890 Figs. 6.9 and 6.10 show the two calculations (with and without model in-
1891 put) along with EG1b data and several χ PT and model predictions. One
1892 important observation here is that our measurements provide the only data
1893 points in the very low Q^2 region (i.e for $Q^2 < 0.05$ GeV 2) where χ PT is
1894 thought to be able to make rigorous calculations. Therefore, our data will
1895 provide important benchmarks for the future calculations in this kinematics.
1896 Particularly, the latest χ PT prediction by Bernard *et al.* [50] seems to agree
1897 remarkably well with data in the very low Q^2 region.

1898 While all other higher Q^2 predictions, except that of Ji *et al.*, seem to
1899 be within the uncertainties of our measurements, it can be seen that the
1900 phenomenological predictions of Soffer *et al.* compare slightly better with
1901 data than others (excluding, of course, the Bernard *et al.* prediction).

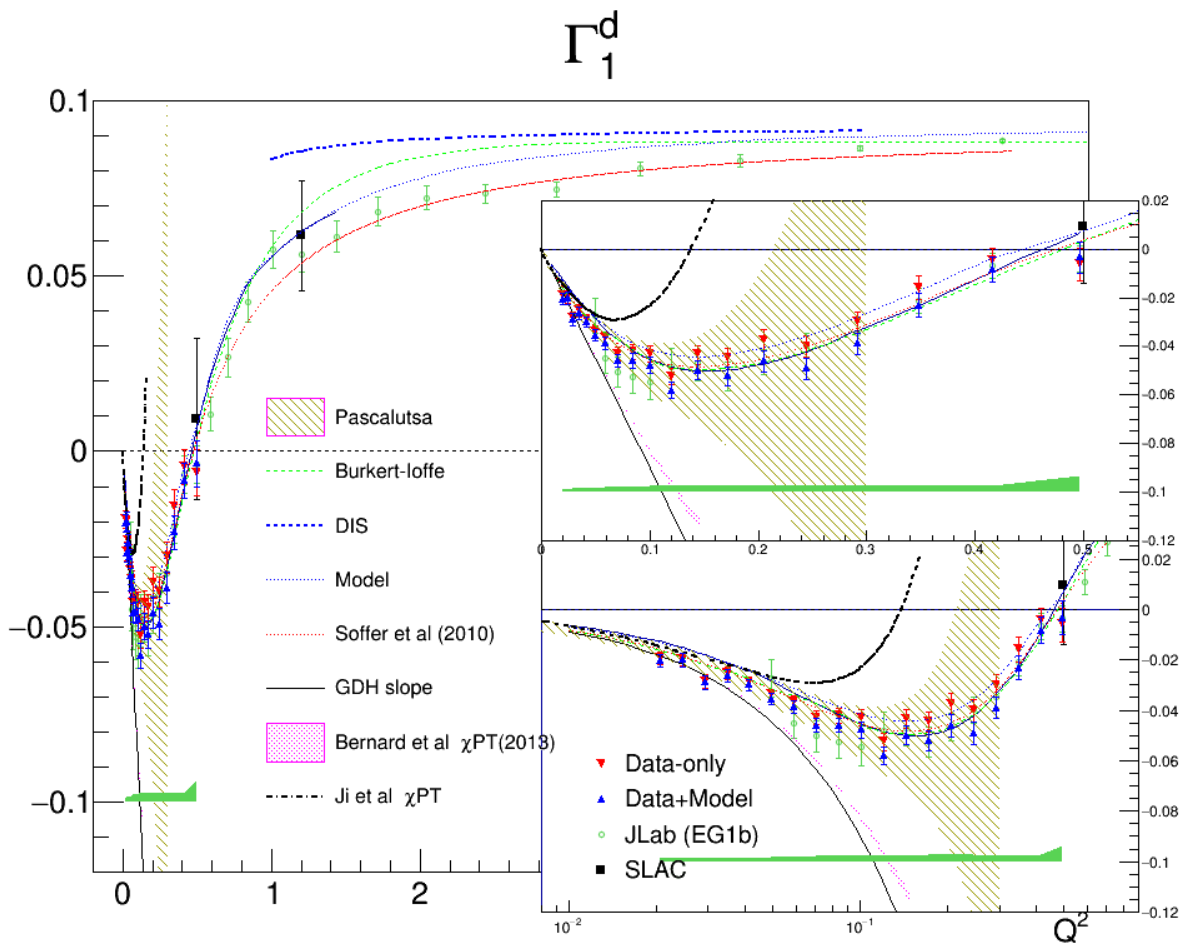


Figure 6.9: Extracted Γ_1 for deuteron compared with some of the past measurements and various theoretical predictions with a linear scale used for Q^2 .

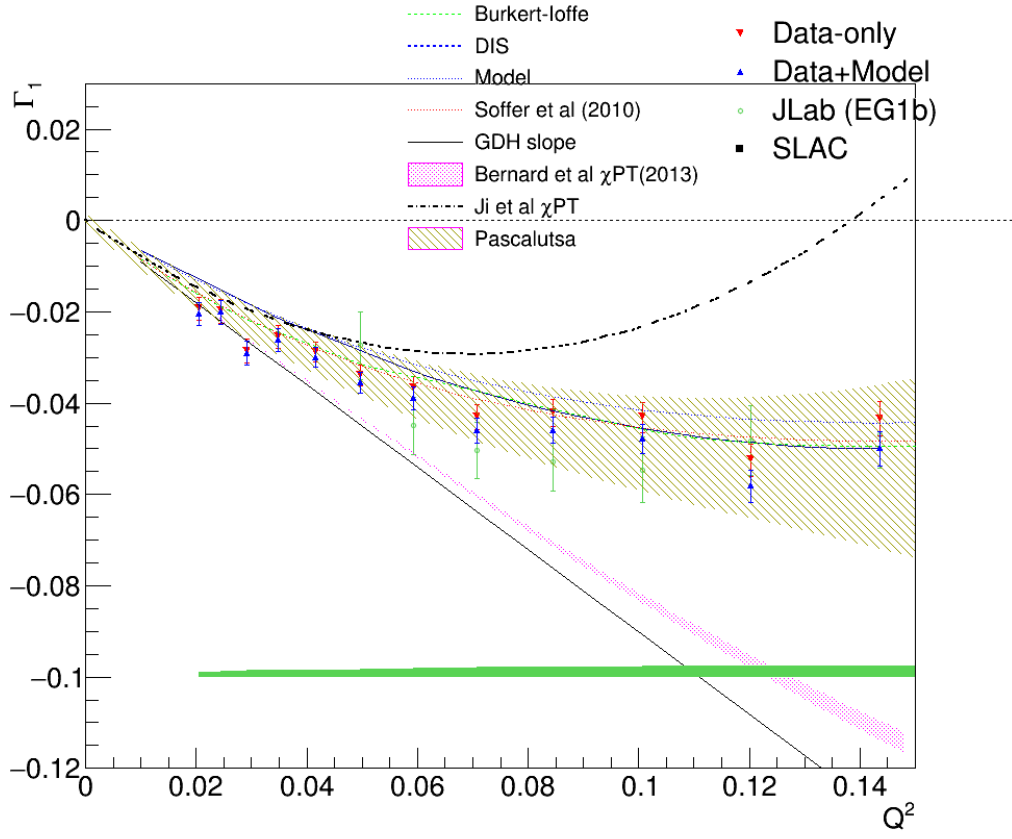


Figure 6.10: Extracted Γ_1 for deuteron compared with some of the past measurements and various theoretical predictions zooming in on the very low Q^2 region.

1902 6.2.2 The extended GDH integral \bar{I}_{TT}

1903 Using the measured values of $A_1 F_1$, the generalized GDH integral $\bar{I}_{TT} =$
 1904 $2M^2/Q^2 \int A_1 F_1(x, Q^2) dx$ was also calculated and compared (see Figs. 6.11
 1905 and 6.12) with the latest χ PT calculation from Bernard *et al.* [50]. We
 1906 can see that at the very low Q^2 , the χ PT prediction and the measurement
 1907 get very close. The χ PT methods determine the higher powers of Q^2 in the
 1908 Taylor expansion of the integral around the photon point $Q^2 = 0$, beyond the
 1909 prediction of the GDH sum rule which determines the lowest order term. Our
 1910 data seem indeed to converge towards the GDH sum rule at our lowest Q^2 .
 1911 However, only one or two higher order terms can be calculated confidently,
 1912 since higher orders require additional (unknown) constants. Therefore, χ PT

1913 predictions do reasonably well at ultra-low Q^2 but cannot be expected to
 1914 work at the higher Q^2 , where the data show a turn-around and a transition
 1915 towards positive values.

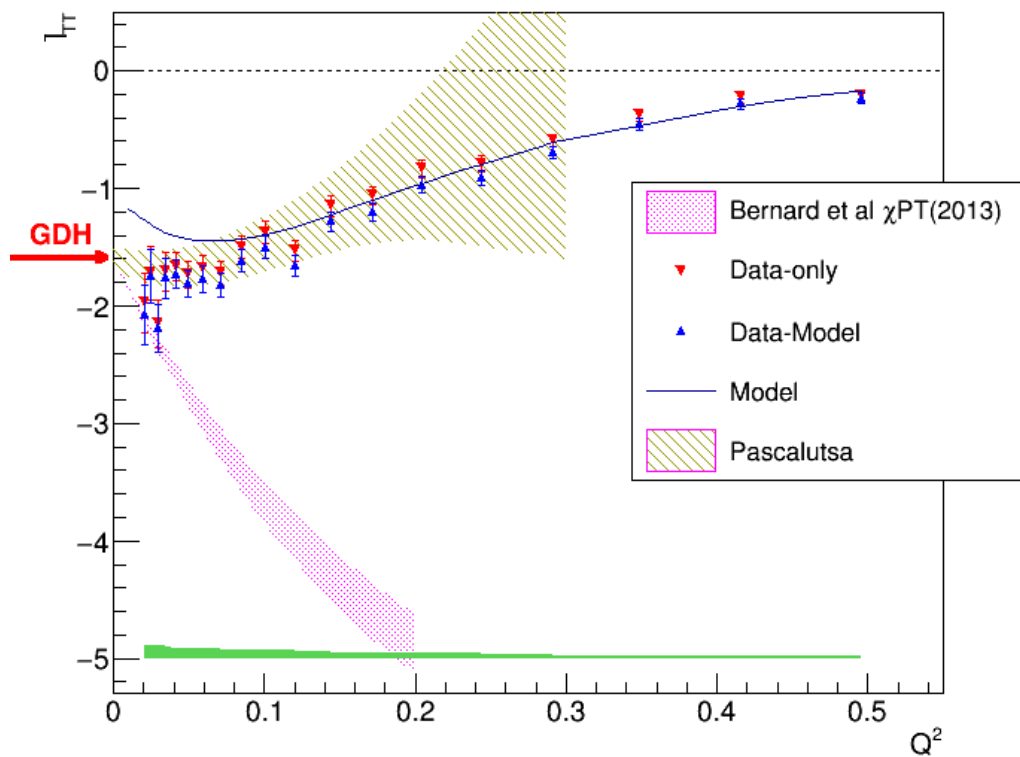


Figure 6.11: Extracted \bar{I}_{tt} for deuteron compared with the used model and a χ PT prediction with a linear scale used for Q^2 .

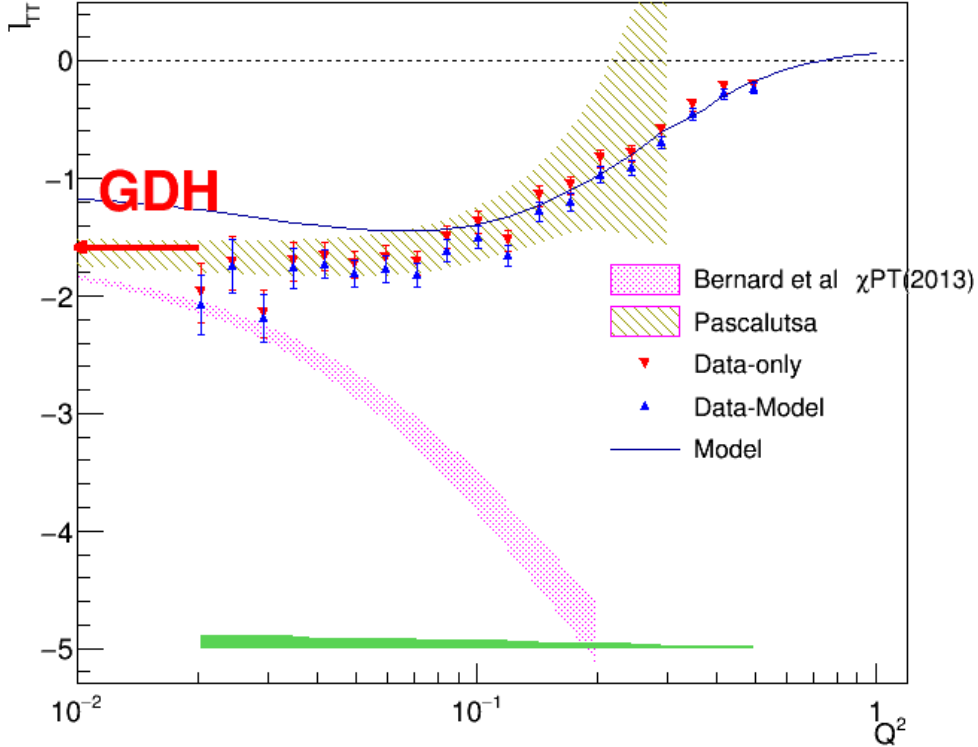


Figure 6.12: Extracted I_{tt} for deuteron compared with the model used in the simulation and two χ PT predictions with a logarithmic scale used for Q^2 .

1916 6.2.3 The Generalized Forward Spin Polarizability γ_0

1917 Finally, the generalized forward polarizability (as given by Eq. 1.16) for
 1918 the deuteron was also calculated using the measured values of $A_1 F_1$ and
 1919 then compared with various predictions as shown in Figs. 6.13 and 6.14.
 1920 The comparison shows that both χ PT calculations by Bernard *et al.* and
 1921 Kao *et al.* converge with data at the lowest Q^2 bins. However, the χ PT
 1922 calculations by Pascalutsa *et al.* seem to deviate greatly from both the
 1923 current measurement as well as the other χ PT calculations (particularly at
 1924 the very low Q^2 region, indicating that some ingredients might be missing
 1925 from the calculation model). Likewise, the MAID prediction also seems to be
 1926 somewhat off the current results.

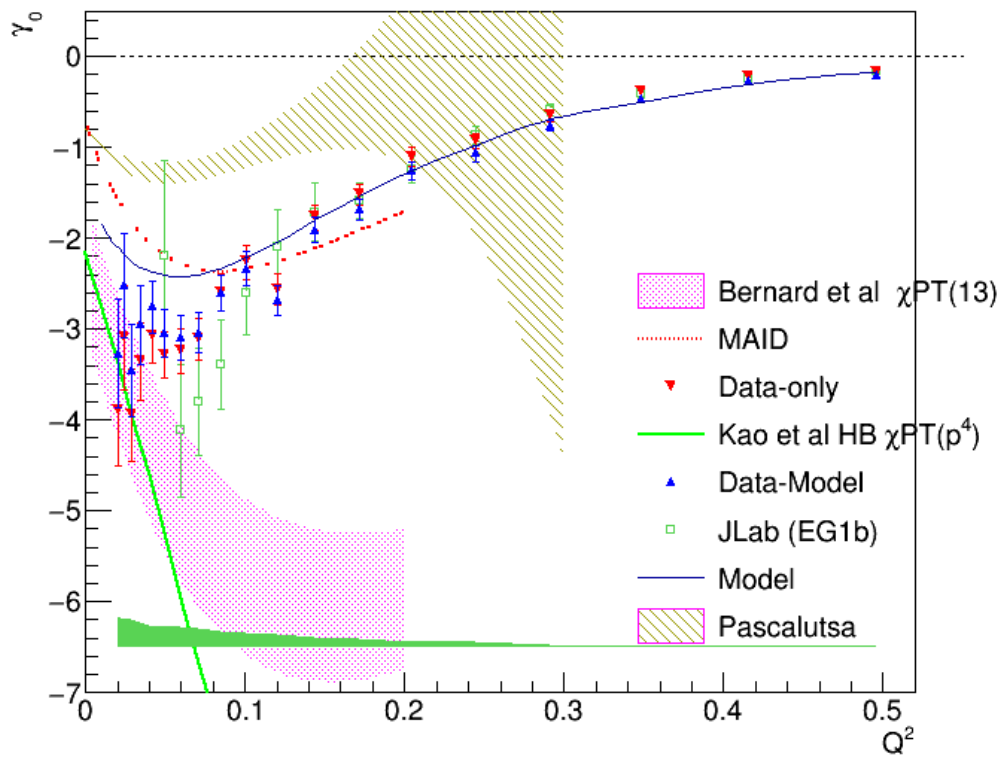


Figure 6.13: Extracted γ_0 for deuteron compared with some of the past measurements and various theoretical predictions with a linear scale used for Q^2 .

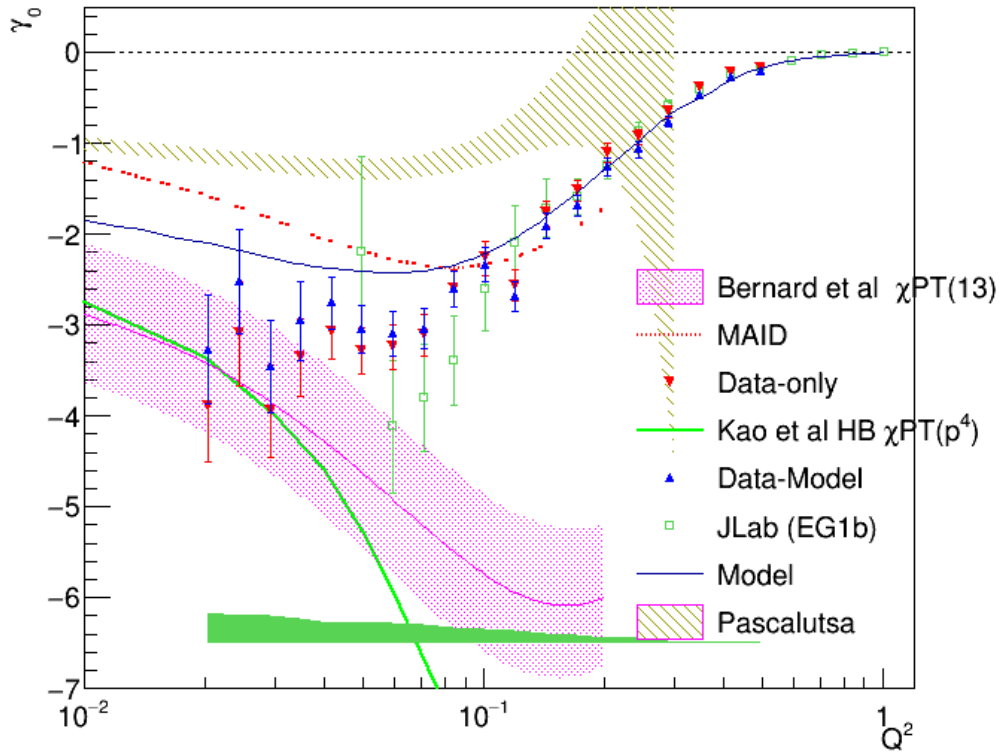


Figure 6.14: Extracted γ_0 for deuteron compared with some of the past measurements and various theoretical predictions with a logarithmic scale used for Q^2 .

1927

Chapter 7

1928

Conclusions

1929

1930 The very low momentum transfer (Q^2) data from the EG4 experiment
1931 have been analyzed for the helicity dependent inclusive cross section (difference)
1932 for the scattering of longitudinally polarized electrons off longitudinally
1933 polarized deuterons (from DNP polarized ND₃ target, using two beam en-
1934 ergies 1.3 and 2.0 GeV). The analyzed data has the kinematic coverage of
1935 ($0.02 \text{ GeV}^2 < Q^2 < 0.7 \text{ GeV}^2$) and ($1.08 \text{ GeV} < W < 2.0 \text{ GeV}$). Al-
1936 though past measurements from EG1b go as low as 0.05 GeV^2 in Q^2 , the
1937 new measurements have higher precision (due to higher statistics and bet-
1938 ter detection efficiency) in the overlapping region (particularly evident below
1939 $Q^2 = 0.2 \text{ GeV}^2$) in addition to new high precision data in the previously
1940 unmeasured region below $Q^2 = 0.5 \text{ GeV}^2$.

1941 The new deuteron data were used to extract the deuteron's spin struc-
1942 ture function g_1 by comparing the experimental data with simulated data
1943 produced by using a realistic cross section model for the deuteron under sim-
1944 ilar kinematic conditions. The newly extracted data pushes the lower limit
1945 on Q^2 in the resonance region with reduced systematic and statistical un-
1946 certainties that will contribute greatly to the world data set. It is observed
1947 that the data from two beam energies give results that are in good agreement
1948 wherever they overlap. The low Q^2 results clearly show resonance structure
1949 in the region $W \leq 2.0$ which smooths out as Q^2 becomes larger. In particular,
1950 the Δ -resonance shows a strongly and consistently negative signal at all Q^2 ,
1951 but the second resonance region (around $W=1.5 \text{ GeV}$) shows a rather rapid
1952 transition of g_1 (or polarized cross section) from strongly negative values at
1953 low Q^2 to clearly positive values at high Q^2 . This observation in the second

1954 resonance region is not well described by the model because the model is not
1955 constrained in the region due to the lack of experimental data up to now and
1956 indicates that the spin-flip helicity amplitude $A_{\frac{3}{2}}^T$ dominates the cross section
1957 at low Q^2 while the non-flip amplitude $A_{\frac{1}{2}}^T$ becomes stronger at higher Q^2 .

1958 The product $A_1 F_1$ of the virtual photon asymmetry A_1 and the unpo-
1959 larized structure function F_1 was also extracted from the same data and
1960 method. The extracted results on g_1 and $A_1 F_1$ were then used to evaluate
1961 three important moments - the first moment Γ_1^d of g_1 , the generalized GDH
1962 integral \bar{I}_{TT}^d and the generalized forward spin polarizability γ_0^d - in each of
1963 the Q^2 bins in which the new g_1 and $A_1 F_1$ have been extracted. The new low
1964 Q^2 measurements of the moments evaluated both with and without model
1965 inputs for the unmeasured kinematic regions were then compared with vari-
1966 ous χ PT calculations, phenomenological predictions and past measurements,
1967 particularly the EG1b or DIS data whenever applicable.

1968 The EG4 results provide the only data points in the very low Q^2 region
1969 ($Q^2 < 0.05 \text{ GeV}^2$) where χ PT is thought to be able to make rigorous calcu-
1970 lations. The high precision data will provide important benchmarks for the
1971 future calculations in this kinematics. In the case of the first moment Γ_1^d ,
1972 the EG4 results show remarkable agreement with the latest χ PT prediction
1973 by Bernard *et al.* [50] in the very low Q^2 region. The phenomenological
1974 predictions which have much larger Q^2 coverage also seem to agree within
1975 the uncertainties of our measurements, with the predictions of Soffer *et al.*
1976 showing slightly better comparison than others. Likewise, the very low Q^2
1977 results of the generalized GDH integral \bar{I}_{TT} are indeed observed to converge
1978 towards the GDH sum rule and thus getting very close to the χ PT predic-
1979 tions by Bernard *et al.* [50]. Finally, the generalized forward polarizability
1980 (γ_0^d) for the deuteron calculated from the EG4 data and the χ PT calculations
1981 by Bernard *et al.* and Kao *et al.* seem to converge at the lowest Q^2 bins.
1982 However, the χ PT based predictions from Pascalutsa *et al.* and the MAID
1983 prediction seems to be well off the current results for all three moments.

1984 The deuteron data in combination with the EG4 proton data taken under
1985 similar conditions (currently being analyzed by another collaborator) will be
1986 useful in extracting neutron quantities in the near future, which is valuable
1987 because of the unavailability of free neutron targets. Moreover, due to the
1988 complexities of the nuclear medium effects, neutron data from deuteron will
1989 be very important to enhance confidence in similar neutron results extracted
1990 from other nuclear targets - particularly ${}^3\text{He}$.

1991 The work presented in this analysis has improved our understanding of the
1992 field of the nucleon spin structure and contributed to more solid foundation
1993 for future advancements. The new data on spin structure functions and their
1994 moments will help various χ PT calculations and phenomenological models
1995 such as MAID to better constrain their parameters enabling them to make
1996 better predictions in the future. With the availability of the high precision
1997 data in the previously (largely) unmeasured region that has the potential to
1998 help constrain the theories and models, it is hoped that a unified description
1999 of spin structure functions over all kinematic regions will be possible in the
2000 future.

₂₀₀₁ Bibliography

- 2002 [1] K.V. Dharmawardane et al. Measurement of the x- and -dependence of
2003 the asymmetry on the nucleon. *Physics Letters B*, 641(1):11 – 17, 2006.
- 2004 [2] J. Ashman and other. A measurement of the spin asymmetry and de-
2005 termination of the structure function g1 in deep inelastic muon-proton
2006 scattering. *Physics Letters B*, 206(2):364 – 370, 1988.
- 2007 [3] D.J. Gross and F. Wilczek. Ultraviolet behavior of non-abelian gauge
2008 theories. *Phys. Rev. Lett.*, 30(26):1343–1346, 1973.
- 2009 [4] Kenneth G. Wilson. Confinement of quarks. *Phys. Rev. D*, 10:2445–
2010 2459, Oct 1974.
- 2011 [5] J. P. Chen and others. The GDH Sum Rule and the Spin Structure of
2012 ^3He and the Neutron using Nearly-Real Photons. JLab Hall A Proposal,
2013 1997. PR97-110.
- 2014 [6] S. B. Gerasimov. *Yad. Fiz.*; 2:598, 1966.
- 2015 [7] S. D. Drell and A. C. Hearn. Exact sum rule for nucleon magnetic
2016 moments. *Phys. Rev. Lett.*, 16:908–911, May 1966.
- 2017 [8] S.E. Kuhn, J.-P. Chen, and E. Leader. Spin Structure of the Nucleon -
2018 Status and Recent Results. *Prog.Part.Nucl.Phys.*, 63:1–50, 2009.
- 2019 [9] H. Dutz et al. First measurement of the gerasimov-drell-hearn sum rule
2020 for ^1H from 0.7 to 1.8 gev at elsa. *Phys. Rev. Lett.*, 91:192001, Nov 2003.
- 2021 [10] H. Dutz et al. Measurement of helicity-dependent photoabsorption
2022 cross sections on the neutron from 815 to 1825 mev. *Phys. Rev. Lett.*,
2023 94:162001, Apr 2005.

- 2024 [11] Dieter Drechsel and Lothar Tiator. The Gerasimov-Drell-Hearn sum rule
 2025 and the spin structure of the nucleon. *Ann.Rev.Nucl.Part.Sci.*, 54:69–
 2026 114, 2004.
- 2027 [12] S. Hoblit et al. Measurements of $hd(\gamma, \pi)$ and implications for the conver-
 2028 gence of the gerasimov-drell-hern integral. *Phys. Rev. Lett.*, 102:172002,
 2029 Apr 2009.
- 2030 [13] M. Anselmino, B.L. Ioffe, and E. Leader. On Possible Resolutions of the
 2031 Spin Crisis in the Parton Model. *Sov.J.Nucl.Phys.*, 49:136, 1989.
- 2032 [14] A. Deur et al. Measurement of the Gerasimov-Drell-Hearn Integral at
 2033 low Q^2 on the Neutron and Deuteron. CLAS Proposal, December 2006.
 2034 PR06-017.
- 2035 [15] Matthias Burkhardt. The $g(2)$ Structure Function. *AIP Conf. Proc.*,
 2036 1155:26–34, 2009.
- 2037 [16] M. Anghinolfi and others. The GDH Sum Rule with Nearly-Real Photo-
 2038 tons and the Proton g_1 Structure Function at Low Momentum Transfer.
 2039 CLAS Proposal, 2003. PR03-006.
- 2040 [17] D. Drechsel, B. Pasquini, and M. Vanderhaeghen. Dispersion relations
 2041 in real and virtual Compton scattering. *Phys. Rept.*, 378:99–205, 2003.
- 2042 [18] N. Guler et al. Precise determination of the deuteron spin structure at
 2043 low to moderate Q^2 with clas and extraction of the neutron contribution.
 2044 *Phys. Rev. C*, 92:055201, Nov 2015.
- 2045 [19] The eg4 wiki. [https://clasweb.jlab.org/rungroups/eg4/wiki/
 2046 index.php/Main_Page](https://clasweb.jlab.org/rungroups/eg4/wiki/index.php/Main_Page). [Online; accessed 22-Sep-2013].
- 2047 [20] X. Zheng. CLAS EG4 Analysis Note - 'Double- and Target Spin Asym-
 2048 metries in Pion Electro-production from Polarized NH₃ Targets'. 2015.
- 2049 [21] X. Zheng et al. Measurement of target and double-spin asymmetries for
 2050 the $\vec{e}\vec{p} \rightarrow \vec{e}\vec{\pi}^+(n)$ reaction in the nucleon resonance region at low Q^2 .
 2051 *Phys. Rev. C*, 94:045206, Oct 2016.
- 2052 [22] N. Guler. *Spin Structure of the Deuteron*. PhD thesis, Old Dominion
 2053 University, December 2009.

- 2054 [23] M. Osipenko, A. Vlassov and M. Taiuti. A vxibus based trigger for the
 2055 clas detector at cebaf. Technical Report CLAS NOTE 2004-020, JLAB,
 2056 2004.
- 2057 [24] K.S. Egiyan. Determination of electron energy cut due to the clas ec
 2058 threshold. Technical Report CLAS-NOTE-1999-007, JLAB, 1999.
- 2059 [25] The eg4 collaboration. <http://clasweb.jlab.org/shift/eg4/>. [On-
 2060 line; accessed 22-Sep-2013].
- 2061 [26] S. E. Kuhn. Private communications, 2013.
- 2062 [27] P. Bosted. Private communications, 2010.
- 2063 [28] Beam energies during the eg4 run. http://www.jlab.org/deurpam/e03006/eg4_energy.pdf. [Online; accessed 05-Jan-2017].
- 2064
- 2065 [29] P. Bosted. CLAS EG1-DVCS Technical Note 004 - 'Tracking from Drift
 2066 Chambers to Target through Solenoid'. 2010.
- 2067 [30] P. Bosted and A. Kim. CLAS EG1-DVCS Technical Note 002 - 'Beam
 2068 (x,y) and Target Center z from Raster ADCs'. 2014.
- 2069 [31] A. Klimentko and S. Kuhn . Momentum Corrections for E6. Technical
 2070 Report CLAS-Note 2003-005, JLAB, 2003.
- 2071 [32] William R Leo. *Techniques for nuclear and particle physics experiments: a how-to approach*. Springer, 1994.
- 2072
- 2073 [33] R. G. Fersch. PhD thesis, January.
- 2074 [34] P. Bosted. Pair-symmetric and pion backgrounds for eg1b. Technical
 2075 Report CLAS-NOTE-2004-005, JLAB, 2004.
- 2076 [35] S. P. Phillips. http://clasweb.jlab.org/rungroups/eg4/wiki/index.php/October_14%2C_2011. [Online; accessed 22-Sep-2013].
- 2077
- 2078 [36] Peter Bosted. Nh3 correction for nd3 target: Eg1-dvcs technical note
 2079 17. Technical report, November 2011.
- 2080 [37] Suman Koirala. EG1-DVCS Part-C Target Contamination. Technical
 2081 report, May 2012.

- 2082 [38] S.E. Kuhn and K. Adhikari. Data Analysis for EG4 - extraction of g_1
 2083 from data. 2013.
- 2084 [39] K. Abe et al. Measurements of the proton and deuteron spin structure
 2085 functions g_1 and g_2 . *Phys. Rev. D*, 58:112003, Oct 1998.
- 2086 [40] T.V. Kuchto and N.M. Shumeiko. Radiative effects in deep inelastic
 2087 scattering of polarized leptons by polarized nucleons. *Nuclear Physics*
 2088 *B*, 219(2):412–436, 1983.
- 2089 [41] L. W. Mo and Y. S. Tsai. Radiative corrections to elastic and inelastic
 2090 ep and up scattering. *Rev. Mod. Phys.*, 41:205–235, Jan 1969.
- 2091 [42] P.E. Bosted and M.E. Christy. Empirical fit to inelastic electron-
 2092 deuteron and electron-neutron resonance region transverse cross-
 2093 sections. *Phys.Rev.*, C77:065206, 2008.
- 2094 [43] R. G. Fersch et al. Precise Determination of Proton Spin Structure
 2095 Functions at Low to Moderate Q^2 with CLAS. To be published, October
 2096 2012.
- 2097 [44] N. Guler et al. Precise Determination of Deuteron and Neutron Spin
 2098 Structure Functions at Low to Moderate Q^2 with CLAS. To be pub-
 2099 lished, October 2013.
- 2100 [45] Yonatan Kahn, W. Melnitchouk, and Sergey A. Kulagin. New method
 2101 for extracting neutron structure functions from nuclear data. *Phys. Rev.*,
 2102 C79:035205, 2009.
- 2103 [46] M. Holtrop. GSIM: CLAS GEANT Simulation. http://nuclear.unh.edu/~maurik/gsim_info.shtml. [Online; accessed 22-Sep-2013].
- 2104 [47] Brooks, W. *CLAS - A large acceptance spectrometer for intermediate*
 2105 *energy electromagnetic nuclear physics*. Jun 1999.
- 2106 [48] B. Dey. *Differential cross section and polarization extractions for $\gamma p \rightarrow K^+ \Sigma^0$ and $\gamma p \rightarrow \phi p$ using CLAS at Jefferson Lab, towards a partial wave*
 2107 *analysis in search of missing baryon resonances*. PhD thesis, Carnegie
 2108 Mellon University, July 2011.
- 2109 [49] J. Zhang. *Exclusive π^- Electro-production from the Neutron in the Res-*
 2110 *onance Region*. PhD thesis, Old Dominion University, May 2010.

- 2113 [50] Veronique Bernard, Evgeny Epelbaum, Hermann Krebs, and Ulf-G.
2114 Meissner. New insights into the spin structure of the nucleon. *Phys.*
2115 *Rev.*, D87:054032, 2013.

₂₁₁₆ **Appendix A**

₂₁₁₇ **FFREAD cards used by GSIM**

Table A.1: Some of the ffreac cards & their values which are used as GSIM input parameters.

Cards	Values
MAGTYPE	2
MAGSCALE	-0.5829 0.0 (for 1.337 GeV)
MAGSCALE	-0.3886 0.0 (for 1.993 GeV)
GEOM	'ALL'
NOMC	'EC' 'SC' 'CC' 'DC'
NOGEOM	'MINI' 'ST' 'TG2' 'TG' 'SOL'
NOGEOM	'PTG' 'FOIL'
NOMATE	'PTG' 'FOIL'
PTGIFIELD	1
TMGIFIELD	1
TMGIFIELDM	1
TMGFIELDM	51.0
TMGSCALE	0.979
PTGMAXRAD	300.0
MGPOS	0.0 0.0 -100.93
BAFF	3. 9. 165.3 9. 180.5 9. 195.8
RUNG	50556
AUTO	1
KINE	1